Optics of atomically thin films and van der Waals heterostructures made from two-dimensional semiconductors

Osvaldo Del Pozo Zamudio

Department of Physics and Astronomy

University of Sheffield

This thesis is submitted for the degree of

Doctor of Philosophy

September 2015

A mi familia

Acknowledgements

I would like to acknowledge, first of all, my supervisor Prof. Alexander Tartakovskii for his advice and support during my PhD.

Thanks to Dr. Jorge Puebla and Dr. Evgeny Chekhovich for their support and guidance during my first year.

An enormous thank you to Dr. Freddie Withers and Prof. Konstantin Novoselov from the University of Manchester for a very fruitful collaboration that resulted in important publications and two chapters of this thesis.

Thanks to Prof. Manfred Bayer and Dr. Ilya Akimov from TU Dortmund for giving me the opportunity of visiting theirs labs to measure PL dynamics. Thanks to Dr. Max Sich for his help and patience during measurements in D52.

I would like to thank my colleagues and friends in the LDSD group, specially Stefan Schwarz, Dr. Daniel Sercombe, Robert Schofield, Dr. Tillmann Godde, Sasha Skrypka.

A big thank you to Chris Vickers and his team for their technical support and professionalism with cryogenics.

Many thanks to CONACYT and SEP for giving me the financial support for my studies.

Thanks to all my friends and housemates in Sheffield.

Thanks to my best friends in Mexico.

And finally, an enormous thank you to my mother, father, brother and sister.

Abstract

This thesis discusses optical investigations of two-dimensional metal-chalcogenide semiconductor materials and their heterostructures. Topics include a study of continuous wave (cw) and time-resolved photoluminescence (PL) of GaTe and GaSe thin films. Based on experimental evidence, we propose a model explaining the strong PL intensity decrease for thin films as a result of non-radiative carrier escape via surface states. We investigate the stability of thin films of InSe and GaSe using a combination of PL and Raman spectroscopies. By comparing signal intensities in films exposed to ambient conditions for up to 100 hours, we find notable degradation in GaSe and high stability of InSe. We continue our study with the investigation of optical properties of light emitting diodes (LED) made of van der Waals (vdW) heterostructures comprising graphene as transparent contacts, hexagonal boron nitride as tunnel barriers and transition metal dichalcogenides (TMDC), MoS_2 and WS_2, as the semiconductor active regions. Single and multiple 'quantum well' structures were fabricated with an aim to enhance the external quantum efficiency (EQE) under electrical injection. We also present PL characterisation of LEDs based on vdW heterostructures comprising WSe_2 and $MoSe_2$ as active layers. Temperature dependent experiments show unusual enhancement of the EQE with temperature in WSe_2 in contrast to $MoSe_2$, where both electroluminescence and PL are reduced with temperature. A theoretical approach to explain this behaviour is proposed, which is based on the strong spin-orbit interaction present in both materials.

List of publications

1. F. Withers, **O. Del Pozo-Zamudio**, S. Schwarz, S. Dufferwiel, P. M. Walker, T. Godde, A. P. Rooney, A. Gholinia, C. R. Woods, P. Blake, S. J. Haigh, K. Watanabe, T. Taniguchi, I. L. Aleiner, A. K. Geim, V. I. Fal'ko, A. I. Tartakovskii, K. S. Novoselov. *WSe_2 light-emitting tunneling transistors with enhanced brightness at room temperature.* Nano Letters **15** (12), 8223-8228 (2015). doi: 10.1021/acs.nanolett.5b03740.

2. **O. Del Pozo-Zamudio**, S. Schwarz, M. Sich, I. A. Akimov, R. C. Schofield, E. A. Chekhovich, B. J. Robinson, N. D. Kay, O. Kolosov, D. N. Borisenko, N. N. Kolesnikov, and A. I. Tartakovskii. *Photoluminescence of two-dimensional GaTe and GaSe films.* 2D Materials **2** (3), 035010 (2015) doi: 10.1088/2053-1583/2/3/035010.

3. F. Withers, **O. Del Pozo-Zamudio**, A. Mishchenko, A. P. Rooney, A. Gholinia, K. Watanabe, T. Taniguchi, S. J. Haigh, A. K. Geim, A. I. Tartakovskii, K. S. Novoselov. *Light-emitting diodes by band-structure engineering in the van der Waals heterostructures.* Nature Materials **14**, 301-306 (2015) doi: 10.1038/nmat4205.

In preparation:

1. **O. Del Pozo-Zamudio**, S. Schwarz, J. Klein, R. C. Schofield, E. A. Chekhovich, O. Ceylan, E. Margapoti, A. I. Dmitriev, G. V. Lashkarev, D. N. Borisenko, N. N. Kolesnikov, J. J. Finley, and A. I. Tartakovskii *Photoluminescence and Raman*

investigation of stability of InSe and GaSe thin films. Submitted to Applied Physics Letters (preprint: arxiv.org/abs/1506.05619).

2. **O. Del Pozo-Zamudio**, S. Schwarz, F. Withers, T. Godde, R. C. Schofield, A. P. Rooney, A. Gholinia, K. Watanabe, T. Taniguchi, S. J. Haigh, A. K. Geim, A. I. Tartakovskii, K. S. Novoselov. *Atomically Thin WSe_2 Light-emitting Diodes Embedded in Monolithic Microcavities.* To be submitted in Nano Letters.

Other publications:

1. S. Dufferwiel, S. Schwarz, F. Withers, A. A. P. Trichet, F. Li, M. Sich, **O. Del Pozo-Zamudio**, C. Clark, A. Nalitov, D. D. Solnyshkov, G. Malpuech, K. S. Novoselov, J. M. Smith, M. S. Skolnick, D. N. Krizhanovskii, A. I. Tartakovskii. *Exciton-polaritons in van der Waals heterostructures embedded in tunable microcavities.* Nature Communications **6**, 8579 (2015). doi: 10.1038/ncomms9579

2. D. Sercombe, S. Schwarz, **O. Del Pozo-Zamudio**, F. Liu, B. J. Robinson, E. A. Chekhovich, I. I. Tartakovskii, O. Kolosov, A. I. Tartakovskii. *Optical investigation of the natural electron doping in thin MoS_2 films deposited on dielectric substrates.* Scientific Reports **3**, 3489 (2013). doi: 10.1038/srep03489

3. I. J. Luxmoore, R. Toro, **O. Del Pozo-Zamudio**, N. A. Wasley, E. A. Chekhovich, A. M. Sanchez, R. Beanland, A. M. Fox, M. S. Skolnick, H. Y. Liu and A. I. Tartakovskii. *III-V quantum light source and cavity-QED on Silicon.* Scientific Reports **3**, 1239 (2013). doi: 10.1038/srep01239

Contents

Contents

Contents

Chapter 1

Background and motivation

1.1 Introduction

Modern condensed matter physics have received an addition of a new branch of study in recent years: physics of two-dimensional (2D) materials [1]. This topic gained prominence with the first isolation of a single-layer of graphite, known as graphene, in 2004 [2]. Since then, the library of 2D materials has been rapidly expanding including hexagonal boron nitride (hBN), transition metal dichalcogenides (TMDCs), III-VI compounds and layered oxides [3, 4]. After an extensive research of graphene that followed the advent of this material [5], scientists started paying more attention to other 2D crystals. This has been reflected in the discovery of various novel characteristics such as mechanical [6, 7], electronic and optical [8], thermal [9], superconductive [10, 11], etc. properties. that lead to potential applications in, e.g, flexible devices [12], lasers [13] and biological studies [14]. Heterostructures based on stacks of 2D materials (known as van der Waals heterostructures) showed additional interesting characteristics due to the possibility to combine and manipulate various properties of the constituent materials [15, 16]. However, because of the novelty of the field, there is still a long way for 2D materials to reach the point where applications become a

reality. For this reason, further investigation of many aspects of material properties and new device prototypes need to be conducted. This thesis focuses on the optical properties of two different groups of two-dimensional materials: III-VI compounds and semiconducting transition metal dichalcogenides. Thin films as well as light emitting diodes based on van der Waals heterostructures made of TMDCs sandwiched with hBN and graphene were characterised. The study was performed using a combination of different optical spectroscopy techniques, including continuous and time-resolved photoluminescence, electroluminescence and Raman spectroscopy which will be described in chapter 2 together with the fabrication methods used to produce samples and devices.

1.2 The family of layered materials

A new family of layered materials, metal-chalcogenides, has recently emerged which includes semi-metals, semiconductors and superconductors. Furthermore, the idea of combining these materials in van der Waals heterostructures has been developed recently. Heterostructures have a long and fruitful history in semiconductor physics. They were used to produce electron and optical confinement, engineering of the electronic energy bands and resonant tunnelling , which led to important technologies such as lasers, solar cells and transistors. These heterostructures, with many examples among III-V semiconductor materials, are grown directly on top of each other by very clean techniques such as molecular beam epitaxy. However such growth techniques are usually limited to the lattice-matched materials. The samples produced by transferring two-dimensional films onto each other to form van der Waals heterostructures allow the combination of a wide range of materials and control of doping and thickness with atomic precision. The goal is that functional devices will be fabricated and that they are able to compete with existing technologies based on heterostructures

in a broad range of applications.

Different experimental techniques are needed in order to perform characterisation of two-dimensional materials and van der Waals heterostructures including electronic transport, optical spectroscopy, microscopy, etc.

The 2D materials studied in this work are III-VI semicondutors such as GaSe, GaTe and InSe in chapters 3 and 4; TMDCs such as MoS_2, $MoSe_2$, WS_2 and WSe_2 in chapters 5 and 6; and, to a lesser extent, graphene and hBN in these latter two chapters. In the following subsections a brief discussion of the properties of these materials will be presented.

1.2.1 Graphene

Graphene is an allotrope of carbon such as the well known and widely studied nanotubes and fullerenes. It consists of carbon atoms in a hexagonal lattice of only one atom thickness separated by 1.42 Å[17]. In the figure 1.1 different carbon allotropes are shown, graphene is the *honeycomb* structure in the right-bottom side of the image.

It has been intensively studied since its first isolation in 2004 by Andre Geim and Konstantin Novoselov[2].

Graphene performance in electronic devices is expected to be of extremely high quality due to its properties. In fig. 1.2 ambipolar electric field effect is observed. This allows charge carrier to be tuned continuously between electrons and holes in high concentrations ($10^{13}cm^{-2}$) and their mobilities μ can exceed 15 000 $cm^2V^{-1}s^{-1}$ [5] as it is shown in the inset of the figure where, with changing V_g, electrons and holes concentration are tuned. This mobility has been observed to be weakly dependent on temperature that makes graphene even more impressive [19].

The ability of graphene to act as a thin and transparent contact for carrier injection is used in this work. Studies of metal-graphene junctions have proved a low resistance
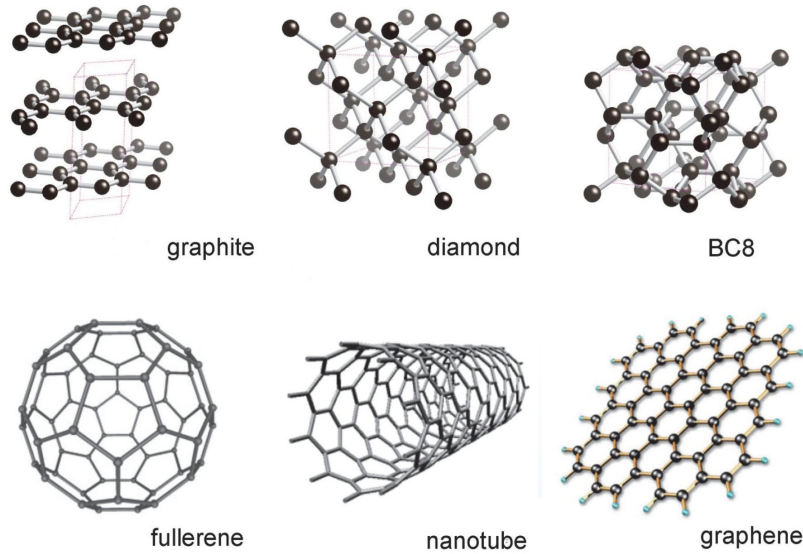
Fig. 1.1 Carbon allotropes[18]. Graphene (bottom right) has a 'honeycomb' structure with carbon atoms separated by 1.42 Å.

in the order of tens of Ω μm [20–22]. This makes graphene suitable for electronic device fabrication like transistors, photo-detectors or LEDs.

Synthesis of graphene

Since the beginning of extensive research of graphene in 2004 using the now famous mechanical exfoliation method (scotch tape)[2], there have been developed different ways to produce few-to-single layer graphene. Nowadays, the mechanical exfoliation technique is still offering the best quality samples for investigation[24]. The main concern is the fact that it is not viable for mass production processes. In table 1.1 a summary of four fabrication methods show in number of layers, sample size and mobility is presented. These methods are: mechanical exfoliation[23, 25], thermal decomposition of silicon carbide[26], chemical vapour deposition (CVD) on Ni[27] and CVD on Cu[28, 29]. Note that large films in the centimetre scale are already produced with high mobility, however the larger the size, the more structural defects are present in the layer.
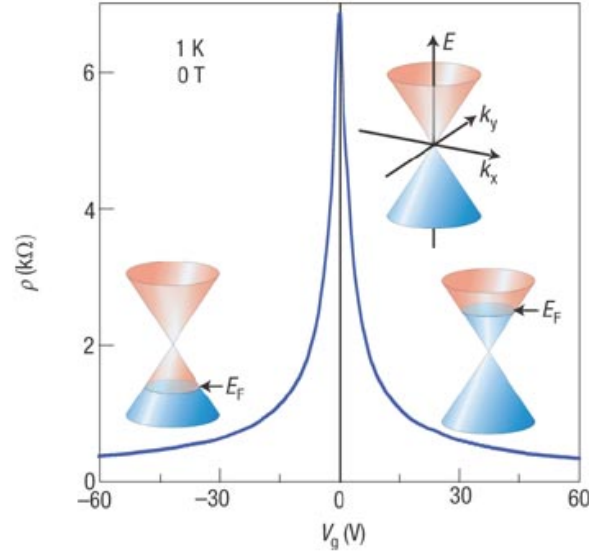
Fig. 1.2 Graphene resistivity ρ plotted as a function of gate voltage V_b[5]. The rapid decrease in resistivity when adding charge carriers indicates their high mobility, in this case 5 000 cm^2 V^{-1} s^{-1} at 1 K and 0 T. This value depends weakly with temperature. The insets show its conical low-energy spectrum $E(k)$, showing changes in the position of the Fermi energy E_F with changing gate voltage V_g. Positive V_g induce electrons and negative V_g induce holes [2, 3, 23].

As it will be discussed in the chapters 2,5 and 6, the graphene layers used in this work were exfoliated from bulk graphite using the scotch tape method and transferred onto different layers to form heterostructures. It is used as transparent electrodes in LEDs for carrier injection thanks to the properties of ambipolar field effect and high conduction discussed previously.

1.2.2 Boron Nitride

Boron nitride (BN) is a chemical compound that consist on equal number of boron and nitrogen atoms. It exists in different crystalline forms with the hexagonal (hBN) being the most studied one. Like TMDCs, it is widely used as a lubricant in industrial applications [30]. Similar to previously discussed materials, weak interlayer bonding is present in hBN so exfoliation methods can be implemented. Due to its wide band

Method	Layers	Size	Mobility ($cm^2V^{-1}s^{-1}$)
Exfoliation	1 to 10+	1 mm	15000
Thermal SiC	1 to 4	50 μm	2000
Ni-CVD	1 to 4	1 cm	3700
Cu-CVD	1	65 cm	16000

Table 1.1 Comparison of graphene synthesis methods. Number of layers, sample size and mobility are shown [24]

.

gap of $\sim$6 eV [31], dielectric properties of this material are very attractive.

In fig. 1.3 a schematic of a single layer of hBN is shown. B and N atoms (purple and yellow spheres, respectively) are arranged in a 'honeycomb' structure. Its lattice constant of 2.5 Å is 1.8 % larger than in graphene [32, 33].
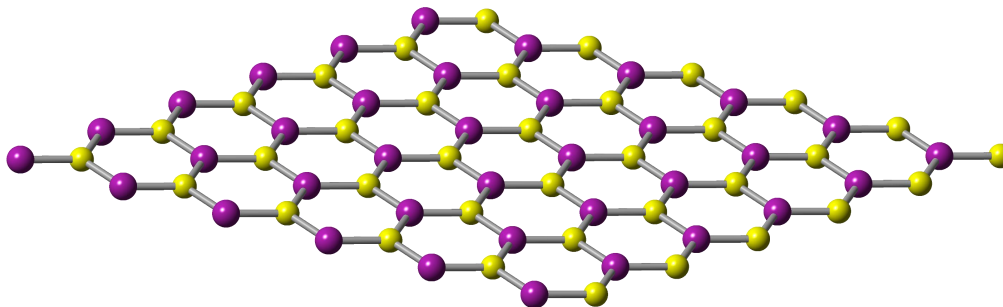
Fig. 1.3 Hexagonal boron nitride single layer. Boron (purple) and Nitrogen (yellow) atoms are arranged in a *honeycomb* structure separated by 2.5 Å.

An important property of hBN is its transparency in a wide range of wavelengths [34] so it has been recently reported to be an ideal layered material for encapsulation and capping of other 2D materials to protect them from oxidation or other atmospheric effects that could produce damage [35] when they are unstable in ambient conditions. In a similar way, it has been proved to be an excellent substrate for graphene electronics [36] reducing carrier inhomogeneity and intrinsic doping [37] in comparison with SiO_2/Si (the most common substrate).

Synthesis of hBN layers

Comparable to other 2D materials, hBN synthesis has been widely investigated resulting in methods similar to those used for graphene. Mechanical exfoliation is, again, the most common and pure method to produce high quality samples with typical sizes of 10-50 μm[38]. Moreover CVD [39] and epitaxial [40] grown hBN has been shown paving the way to the production of samples on the industrial scales.

In this work, hBN is mechanically exfoliated from bulk and used for encapsulation of devices and as a barrier for the quantum well structures (from single to few layers). This will be discussed in detail in chapters 5 and 6.

1.2.3 III-VI semiconductors

III-VI semiconductors are compounds of the form AB where A is an element from the group III of the periodic table and B from the group VI. These compounds are layered crystals with strong covalent in-plane inter-atomic bonding and weaker van der Waals inter-plane bonding[41]. Bulk crystals are stacks of a hexagonal tetralayers in-plane structure of the form B-A-A-B (A=Ga, In; B=S, Se, Te). For the wider studied GaSe, several types of stacking exist leading to different polytypes[42–44]. For GaTe having a monoclinic crystal lattice [45, 46] the polytypic behavior has not been observed [46, 47]. In fig. 1.4 the crystal structure of III-VI compound is presented (III atoms shown in purple, VI in blue): in 1.4A it is seen from the top and the hexagonal lattice is observed. In 1.4B it is viewed from the side where group-III atoms are sandwiched by group-VI atoms, and in 1.4C it is seen from an angle. Table 1.2 presents the structural parameters and band gap energies of the three III-VI semiconductors used in this work.

In the past decades, III-VI compounds attracted attention because of their non-linear optical properties. Some of the most important is their capability as second
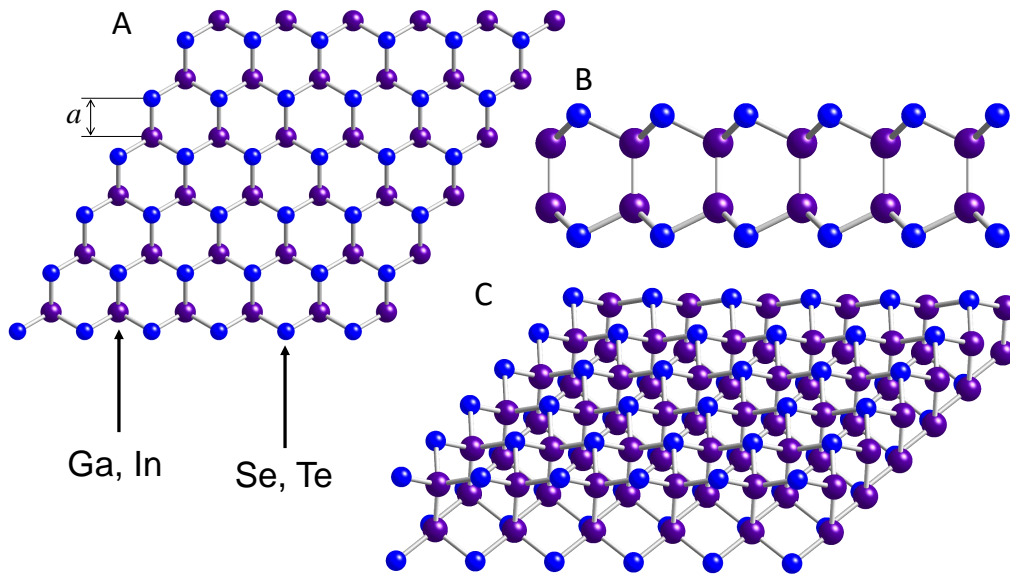
Fig. 1.4 $III - VI$ crystal structure of a single layer viewed from (A) top, (B) side and (C) an angle to observe the layered geometry. Purple balls represent atoms of a group-III material, i.e. Ga, In. Blue balls are atoms of a group-VI material, i.e. Se, Te. See table 1.2 for structural parameters a and c.

Compound	a (Å)	c (Å)	E_g (eV)
GaSe	3.755	15.95	2.1
GaTe	4.06	16.90	1.7
InSe	4.00	16.70	1.3

Table 1.2 Structural parameters and band gap energies of III-VI semiconductors[41].

harmonic generation (SHG) materials [48, 49] and also far infra-red properties in the THz range [50].

Properties of sub-micron thick films have been reported only recently. GaSe, GaS and GaTe thin films were investigated for photodetector and sensor applications [51–53], flexible electronics[54] and phototransistors [55]. InSe suggests interesting potential for solar cells [56, 57], room temperature electroluminescence [58] and shows tuning of band gap with film thickness [59, 60]. These studies open up new possibilities for 2D III-VI films in nano- and opto-electronics.

Furthermore, in contrast to molybdenum and tungsten chalcogenides emitting light efficiently only in films with a single unit cell thickness, as it will be discussed later in this chapter, III-VI materials are bright light emitters in a range of thicknesses[59, 60]. This may relax the stringent fabrication requirements and add flexibility for the novel heterostructured devices such as light emitting diodes.

Synthesis of III-VI layers

In the previous section, it was mentioned that III-VI semiconductor materials have not been studied extensively in their layered form. As a consequence, only few reports of different methods of synthesis can be found: mechanical exfoliation, used for graphene in the studies that started the study of 2D materials [2] was employed in the case of InSe[59, 60], GaSe[53] and GaTe [55] and epitaxy was used for GaSe[54].

3D crystals of Gallium-based III-VI materials are usually grown by high-pressure vertical zone melting in graphite crucibles under Ar pressure[61–64]. The gallium mono-chalcogenides used in this work were synthesized from high-purity materials: Ga and Te - 99.9999 %, Se - 99.9995 %. InSe single crystals were grown by the Bridgman-Stockbarger method from a preliminarily synthesized ingot [65].

The thin film samples studied in this work were produced using mechanical exfoliation from bulk materials onto SiO_2/Si substrates. This method will be explained in detail in the next chapter.

1.2.4 Transition metal dichalcogenides

Transition metal dichalcogenides (TMDCs) are a family of compounds of the form MX_2, where M a transition metal (Mo, W, etc.) and X a chalcogen atom (S, Se or Te). These compounds were largely studied in their bulk form five decades ago in material science and engineering that led to important industrial applications as

solid lubricants and surface protectors[66–68]. New properties of these materials were discovered when they were produced in monolayer form [3]. The crystal structures of these compounds are very similar to each other and consists of a M atom sandwiched by two X atoms. In fig. 1.5 a schematic of a single layer of a MX_2 single-layer is shown from three different angles. X atoms are presented in yellow and M in blue. In 1.5A it is seen from top, where the hexagonal structure is evident. In 1.5B the single layer is viewed from the side, showing the atomic structure of M atoms sandwiched by two X atoms and in 1.5C the single layer is viewed from a 3D perspective. Bulk crystals are formed by vertical stacking of these single layers separated by the half of the vertical lattice constant c. Table 1.3 shows the structural parameters of the four TMDCs used in this work.
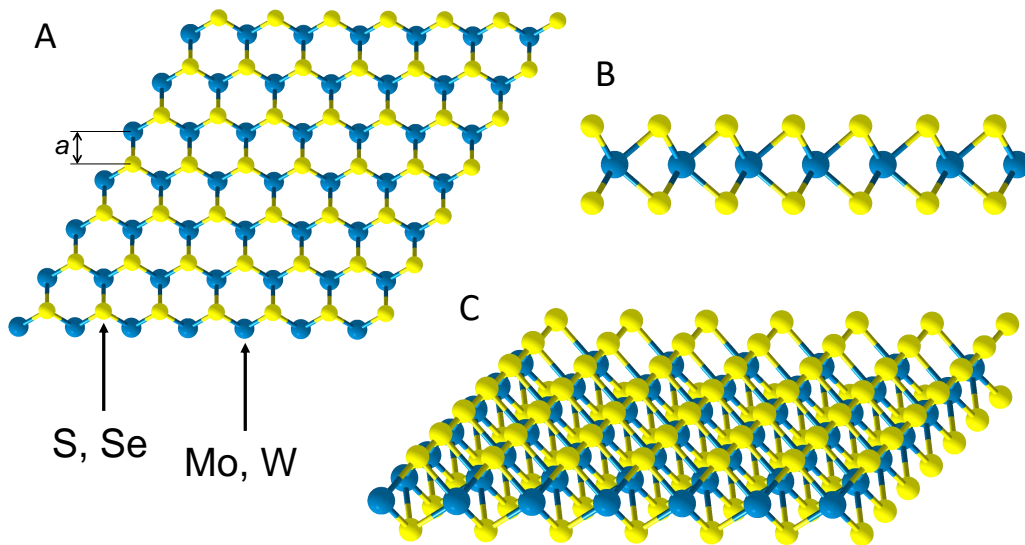
Fig. 1.5 Single layer of a MX_2 single layer viewed from three different angles: (a) Top (b) side and (c) 3D perspective. M atoms are shown in blue and X in yellow. See table 1.3 for parameters of structural parameters of various TMDCs.

Some of the most studied TMDCs in the 2D research such as MoS_2, $MoSe_2$, WS_2 and WSe_2 received much attention in the last few years due to important transformation in their electronic band structure in few monolayer thick films. These are

Compound	a (Å)	c (Å)	E_g (eV)	Δ_{SO} (meV)	Δ_{cb} (meV)	E_b (meV)	E_c(meV)
MoS_2	3.18	12.296	1.67	146	3	570	18
$MoSe_2$	3.32	12.939	1.44	183	22	550	30
WS_2	3.19	12.349	1.81	425	32	700	20-40
WSe_2	3.32	12.976	1.55	461	37	600	30

Table 1.3 Structural parameters, band gap energies E_g, spin-orbit splitting of the valence band Δ_{SO} and the conduction band Δ_{cb}, exciton E_b and trion E_c binding energies of TMDCs used in this work [72–76].

semiconductor materials with an indirect band gap in the bulk form. When they are thinned down to single layer, a transition to a direct band gap occurs[69, 70]. Excitonic effects govern their optical properties[71]. The different band gap energies E_g for the four TMDCs mentioned above are shown in table 1.3.

The electronic structure of TMDCs has been calculated by several theory groups to show the above mentioned transition from indirect to direct band gap semiconductor [70, 72, 77]. In fig. 1.6 a calculated band structure of MoS_2 using density functional theory is presented for (a) bulk, (b) quadrilayer, (c) bilayer and (d) monolayer reported in [70]. In this case the indirect bandgap occurs in the Γ point for bulk and the transition to direct bandgap occurs in the K point. Similar behaviour of the band is present in others TMDCs such as $MoSe_2$, WS_2 and, more ambiguously, in WSe_2 as was shown in one of the studies [73]. For the latter case, a special investigation of the band structure is discussed in Chapter 6.

Both optical and electronic remarkable properties have been observed in monolayers. Field effect transistors (FETs) made of MoS_2 due to high mobility [78], flexible electronic devices [79] exploit strain tuning effects[72] and solar cells [80] are some examples of the research reported recently.
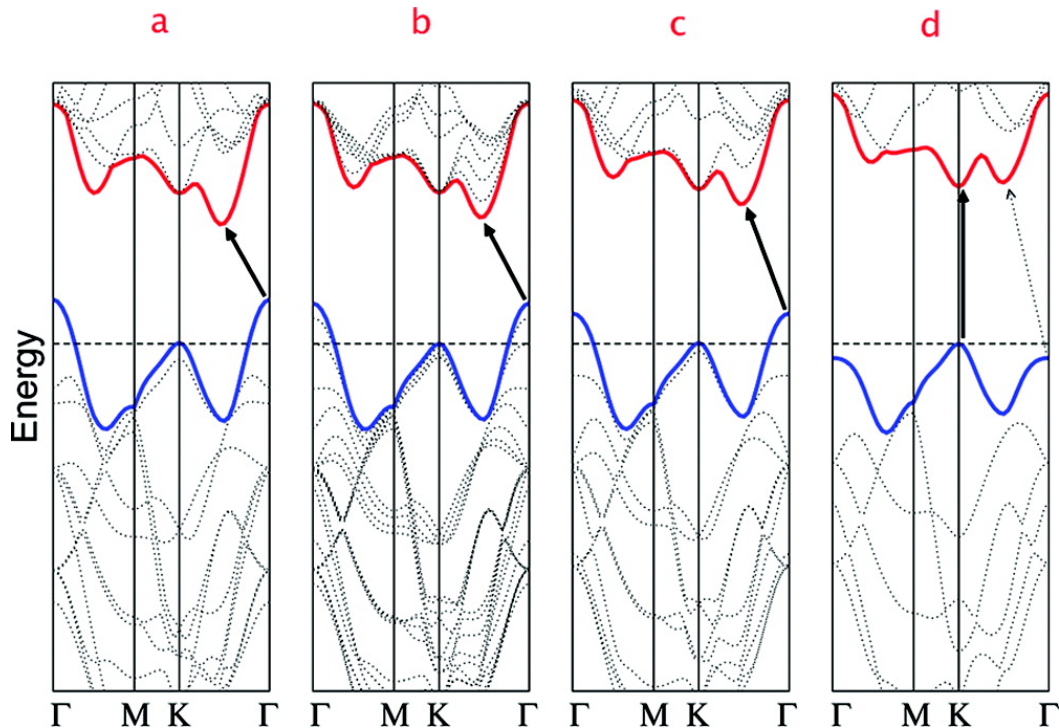
Fig. 1.6 Electronic band structure of (a) bulk (b) quadrilayer (c) bilayer and (d) single layer MoS_2. The transtition from indirect to direct band gap is observed [70].

Excitonic properties of TMDCs

In semiconductor physics, an essential quasiparticle called exciton that consists of an electron-hole pair is formed when an electron is excited from the valence band to the conduction band [81]. These quasiparticles can be seen as hidrogen-like atoms due to the Coulomb force that binds the electron and hole. The simplest exciton, formed just by one electron and one hole, has no charge (neutral) and is usually denoted X^0 as it is illustrated in fig. 1.7(a). When more than one electrons or holes form the quasiparticle, they are called charged excitons or trions and denoted X^-, X^+, depending on the charge state.

In TMDC monolayers, excitons are strongly influenced by the strong spin-orbit coupling producing splitting (Δ_{SO}) in the valence band [82]. This results in the formation of two excitonic transitions, usually referred to as A and B, associated to direct

optical transitions between band edges [8] at the K points, this can be observed in fig. 1.7(b) where the transitions are still depicted in the single-particle band structure representation with no excitonic effects shown. The giant magnitude of Δ_{SO} in ultrathin TMDC layers is predicted to be from ~140 to 460 meV (see table 1.3)[82] and experimentally observable both from PL and absorption spectra like in the case of MoSe$_2$ in fig. 1.7(c). In general, excitation with light generates free neutral excitons on the TMDCs and, in the case of doped layers, trions can be created as well when $e-h$ pairs bind to additional charge. The exciton binding energies E_b have been predicted by first-principles calculations [83, 84] to be extraordinarily large on the order of hundreds of meV (see table 1.3). Different experimental results have demonstrated these magnitudes including reflection spectra [85], two-photon absorption [86] and scanning tunnelling microscopy [87]. The strong binding energy emerges from the 2D geometry and the large effective masses of electrons and holes [84]. In comparison with III-V semiconductors, the binding energy is two orders of magnitude larger in 2D TMDCs. For example, in GaAs it is ~5 meV with an effective electron mass m_e=0.063m_0. For MoS$_2$ the binding energy is 146 meV with m_e=0.37m_0. It is clear that the value of the electron effective masses play a very important roll here as they differ significantly in both materials. It is worth to compare the exciton Bohr radius a_B (distance between electron and hole) of both types of materials as well. In TMDCs a_B ~1 nm [84], one order of magnitude smaller than in GaAs. Since the a_B is only ~3 times the unit cell dimensions a, the excitons in 2D TMDCs belong to a case in between a typical Wannier-Mott exciton and a Frenkel exciton[88], where a_B is larger than the lattice constant a.

Properties of trions can also be understood from optical spectra. For example, from the energy splitting in PL spectra as shown in 1.7(c), the difference between X^- or X^+ and the neutral exciton X^0 is called trion binding energy E_c and corresponds

to the energy that binds the additional charge to the exciton. PL experiments show clearly separated X^0 and X^- peaks in TMDCs and range from ∼20 to 40 meV [75] (see table 1.3). In the inset of 1.7(c) both X^0 and X^- from monolayer $MoSe_2$ are clearly observable with a separation of 30 meV [89].

Recent theoretical studies have shown that spin-orbit splitting is also relatively large in the conduction band for some TMDC monolayers and the spin ordering affects the excitonic dark and bright states [76]. These effects have not been studied experimentally in detail due to the fact that for MoS_2, the most investigated TMDC, the splitting is of the order of a few meV. In table 1.3 the calculated spin-orbit splitting of the conduction band Δ_{cb} for the materials used in this work are presented. In chapter 6 a temperature dependent study of the electroluminesence of $MoSe_2$ and WSe_2 will be presented and the effects are mainly explained as a result of their large Δ_{cb}.

Another important property of excitons is their spin. It depends on both electron (↑ or ↓) and hole (⇑ or ⇓) spins and play a key role when a recombination that leads to emission of a photon occurs. For conservation of angular momentum, an exciton should have total spin $S=0$, this is the case when electron and hole have opposite spins (↑⇓ or ↓⇑), and will be a bright state. For $S=0$ (same spin, ↑⇑ or ↓⇓), their direct recombination is forbidden as momentum conservation cannot be satisfied and the exciton is therefore dark. Optical interband transitions always conserve the spin. Therefore, only the bright exciton can radiatively recombine and result in a photon emission, as the name itself implies. Bright excitons are directly observable from the PL spectra[75].

The excitonic properties of the TMDCs are very important in the study presented in chapters 5 and 6 where LEDs made of these materials are studied and PL and EL spectra are described in terms of excitonic effects.
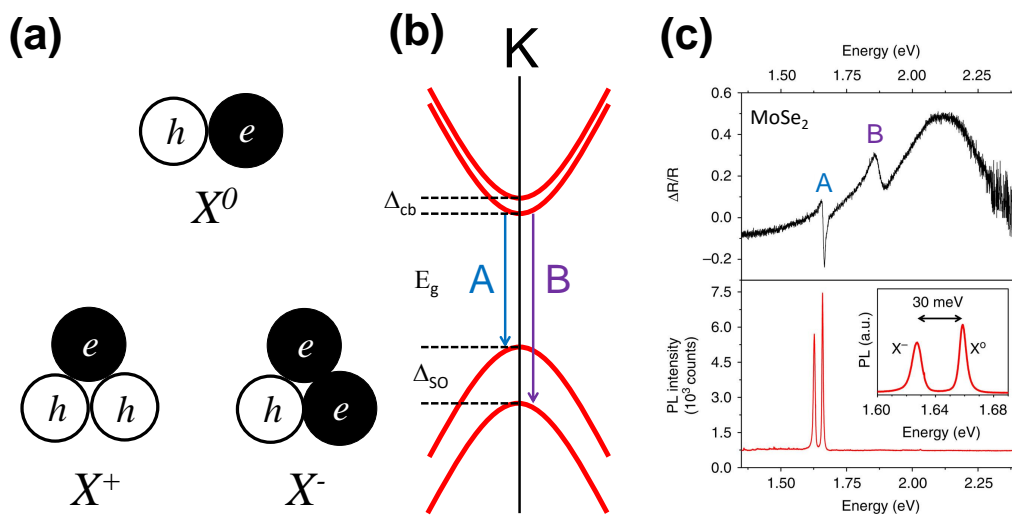
Fig. 1.7 Excitons in TMDCs monolayers. (a) Diagrams of excitons X^0 and trions X^+, X^-. (b) Diagram of the band structure around the K point of TMDC monolayers. The excitonic transitions A and B due to Δ_{SO} are observed in blue and purple, respectively. (c) Differential reflectance spectra (top) of monolayer MoSe$_2$ at 20 K shows A and B excitons. X^0 and X^- are observed in the PL spectra (bottom). Inset: zoom to the PL peaks shows a X^- charging energy of 30 meV[89].

Synthesis of TMDCs layers

Mechanical cleaving or exfolation used for production of graphene [2] has been extended to TMDCs. It is possible to obtain clean high quality samples, but the production rate is generally low and is not suitable for technological applications. As a consequence, further fabrication methods emerged that in principle could be used for a large scale production of TMDCs. This can be obtained, for example, by using chemical vapour deposition (CVD), a common technique used for decades to produce thin films of a large variety of composites including silicon, nitrides, carbon nanotubes and high-k dielectrics [90–92]. In recent years, reports of different CVD grown TMDCs like MoS_2[93–95], WS_2 [95, 96], WSe_2[97, 98] and $MoSe_2$[99, 100] have been published. The properties that all these works share is that crystals grow in a form of triangles due to hexagonal structure (see fig. 1.5). The layers can be grown on or transferred onto a variety of substrates such as sapphire, quartz, gold or SiO_2 in film size of hundreds of micrometres to a millimetre scale [93–100].

Another elaborated technique is liquid exfolation, which uses ion intercalation between atomic layers in a liquid environment to split them from each other [101–103]. This process results in a liquid solution that can be span or sprayed onto a substrate producing a large area covered by single layers of the material.

In the next chapter a detailed description of the mechanical exfoliation method will be presented since it was the technique used in this work to produce TMDCs samples.

1.2.5   van der Waals heterostructures

One of the properties that all the materials described previously in this chapter share is the weak interlayer bonding in their bulk form. Due to this, it is natural to think of the stacking of layers of different materials. A typical analogy, proposed by Geim [15], is to imagine the atomic layers as LEGO blocks. When various blocks are stacked on

top of each other, they get strongly attached and form a more complex structure. The strong covalent bonding of the two-dimensional materials act in a similar way. The possibility of making multilayer structures forming new artificial materials has been extensively studied recently [71, 104].
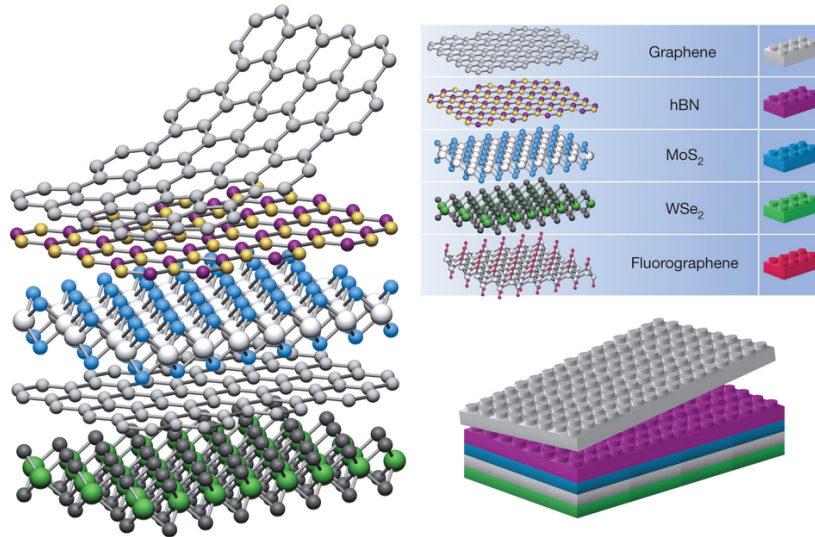
Fig. 1.8 Analogous representation of van der Waals heterostructures with LEGO blocks. The stacking of different classes of layered materials like graphene, MoS_2, hBN, etc. to build more complex structures is possible[15].

Among the reports on vdW heterostructures are the fabrication of field effect tunnelling transistors based on hBN and graphene [104], demonstration of tunnelling diodes with negative differential resistance[105] and photovoltaic devices based on MoS_2-graphene [106] and WS_2-graphene [107]. In terms of optical studies, long-lived interlayer excitons in $MoSe_2$-WSe_2 heterostructures[108] and LEDs [109] have been demonstrated.

Fabrication of van der Waals heterostructures

In section 2.1.2 the most common method for van der Waals heterostructure will be presented, namely so-called 'peel/lift transfer'. This technique has been the base of

almost all the studies mentioned above and consists of the mechanical exfoliation of the desired layers followed by the transfer and stacking on top of each other [110, 111]. In this work LEDs based on vdW heterostructures made of graphene, hBN and TMDCs are built with this method and they will be presented in chapters 5 and 6. These devices were fabricated in laboratories of The University of Manchester by Dr. F. Withers.

References

[1] Elizabeth Gibney. 2d or not 2d, 2015.

[2] Kostya S Novoselov, Andre K Geim, SV Morozov, D Jiang, Y_ Zhang, SV Dubonos, , IV Grigorieva, and AA Firsov. Electric field effect in atomically thin carbon films. *science*, 306(5696):666–669, 2004.

[3] K. S. Novoselov, D. Jiang, F. Schedin, T. J. Booth, V. V. Khotkevich, S. V. Morozov, and A. K. Geim. Two-dimensional atomic crystals. *Proceedings of the National Academy of Sciences of the United States of America*, 102(30):10451–10453, 2005. doi: 10.1073/pnas.0502848102.

[4] Ruben Mas-Balleste, Cristina Gomez-Navarro, Julio Gomez-Herrero, and Felix Zamora. 2d materials: to graphene and beyond. *Nanoscale*, 3(1):20–30, 2011.

[5] Andre K Geim and Konstantin S Novoselov. The rise of graphene. *Nature materials*, 6(3):183–191, 2007.

[6] Qun Wei and Xihong Peng. Superior mechanical flexibility of phosphorene and few-layer black phosphorus. *Applied Physics Letters*, 104(25):251915, 2014.

[7] Changgu Lee, Xiaoding Wei, Jeffrey W Kysar, and James Hone. Measurement

of the elastic properties and intrinsic strength of monolayer graphene. *science*, 321(5887):385–388, 2008.

[8] Qing Hua Wang, Kourosh Kalantar-Zadeh, Andras Kis, Jonathan N Coleman, and Michael S Strano. Electronics and optoelectronics of two-dimensional transition metal dichalcogenides. *Nature nanotechnology*, 7(11):699–712, 2012.

[9] Alexander A Balandin. Thermal properties of graphene and nanostructured carbon materials. *Nature materials*, 10(8):569–581, 2011.

[10] Defa Liu, Wenhao Zhang, Daixiang Mou, Junfeng He, Yun-Bo Ou, Qing-Yan Wang, Zhi Li, Lili Wang, Lin Zhao, Shaolong He, et al. Electronic origin of high-temperature superconductivity in single-layer fese superconductor. *Nature communications*, 3:931, 2012.

[11] Xiaoxiang Xi, Liang Zhao, Zefang Wang, Helmuth Berger, László Forró, Jie Shan, and Kin Fai Mak. Strongly enhanced charge-density-wave order in monolayer nbse2. *Nature nanotechnology*, 2015.

[12] Sang Jin Kim, Kyoungjun Choi, Bora Lee, Yuna Kim, and Byung Hee Hong. Materials for flexible, stretchable electronics: Graphene and 2d materials. *Annual Review of Materials Research*, 45(1):63–84, 2015. doi: 10.1146/annurev-matsci-070214-020901.

[13] Sanfeng Wu, Sonia Buckley, John R Schaibley, Liefeng Feng, Jiaqiang Yan, David G Mandrus, Fariba Hatami, Wang Yao, Jelena Vučković, Arka Majumdar, et al. Monolayer semiconductor nanocavity lasers with ultralow thresholds. *Nature*, 520(7545):69–72, 2015.

[14] Kostas Kostarelos and Kostya S Novoselov. Exploring the interface of graphene and biology. *Science*, 344(6181):261–263, 2014.

References

[15] AK Geim and IV Grigorieva. Van der waals heterostructures. *Nature*, 499(7459): 419–425, 2013.

[16] Hui Fang, Corsin Battaglia, Carlo Carraro, Slavomir Nemsak, Burak Ozdol, Jeong Seuk Kang, Hans A Bechtel, Sujay B Desai, Florian Kronast, Ahmet A Unal, et al. Strong interlayer coupling in van der waals heterostructures built from single-layer chalcogenides. *Proceedings of the National Academy of Sciences*, 111(17):6198–6202, 2014.

[17] Monica Pozzo, Dario Alfe, Paolo Lacovig, Philip Hofmann, Silvano Lizzit, and Alessandro Baraldi. Thermal expansion of supported and freestanding graphene: lattice constant versus interatomic distance. *Physical review letters*, 106(13): 135501, 2011.

[18] Artem R Oganov, Russell J Hemley, Robert M Hazen, and Adrian P Jones. Structure, bonding, and mineralogy of carbon at extreme conditions. *Rev Mineral Geochem*, 75(1):47–77, 2013.

[19] S. V. Morozov, K. S. Novoselov, M. I. Katsnelson, F. Schedin, D. C. Elias, J. A. Jaszczak, and A. K. Geim. Giant intrinsic carrier mobilities in graphene and its bilayer. *Phys. Rev. Lett.*, 100:016602, Jan 2008. doi: 10.1103/PhysRevLett.100. 016602. URL `http://link.aps.org/doi/10.1103/PhysRevLett.100.016602`.

[20] Fengnian Xia, Vasili Perebeinos, Yu-ming Lin, Yanqing Wu, and Phaedon Avouris. The origins and limits of metal-graphene junction resistance. *Nature nanotechnology*, 6(3):179–184, 2011.

[21] K Nagashio, T Nishimura, K Kita, and A Toriumi. Contact resistivity and current flow path at metal/graphene contact. *Applied Physics Letters*, 97(14): 143514, 2010.

[22] Cheng Gong, Stephen McDonnell, Xiaoye Qin, Angelica Azcatl, Hong Dong, Yves J Chabal, Kyeongjae Cho, and Robert M Wallace. Realistic metal–graphene contact structures. *ACS nano*, 8(1):642–649, 2013.

[23] KSA Novoselov, Andre K Geim, SVb Morozov, Da Jiang, MIc Katsnelson, IVa Grigorieva, SVb Dubonos, and AAb Firsov. Two-dimensional gas of massless dirac fermions in graphene. *nature*, 438(7065):197–200, 2005.

[24] Daniel R Cooper, Benjamin D'Anjou, Nageswara Ghattamaneni, Benjamin Harack, Michael Hilke, Alexandre Horth, Norberto Majlis, Mathieu Massicotte, Leron Vandsburger, Eric Whiteway, et al. Experimental review of graphene. *ISRN Condensed Matter Physics*, 2012, 2012.

[25] Andre Konstantin Geim. Graphene: status and prospects. *science*, 324(5934): 1530–1534, 2009.

[26] Konstantin V Emtsev, Aaron Bostwick, Karsten Horn, Johannes Jobst, Gary L Kellogg, Lothar Ley, Jessica L McChesney, Taisuke Ohta, Sergey A Reshanov, Jonas Röhrl, et al. Towards wafer-size graphene layers by atmospheric pressure graphitization of silicon carbide. *Nature materials*, 8(3):203–207, 2009.

[27] Keun Soo Kim, Yue Zhao, Houk Jang, Sang Yoon Lee, Jong Min Kim, Kwang S Kim, Jong-Hyun Ahn, Philip Kim, Jae-Young Choi, and Byung Hee Hong. Large-scale pattern growth of graphene films for stretchable transparent electrodes. *Nature*, 457(7230):706–710, 2009.

[28] Sukang Bae, Hyeongkeun Kim, Youngbin Lee, Xiangfan Xu, Jae-Sung Park, Yi Zheng, Jayakumar Balakrishnan, Tian Lei, Hye Ri Kim, Young Il Song, et al. Roll-to-roll production of 30-inch graphene films for transparent electrodes. *Nature nanotechnology*, 5(8):574–578, 2010.

References

[29] Xuesong Li, Carl W Magnuson, Archana Venugopal, Jinho An, Ji Won Suk, Boyang Han, Mark Borysiak, Weiwei Cai, Aruna Velamakanni, Yanwu Zhu, et al. Graphene films with large domain size by a two-step chemical vapor deposition process. *Nano letters*, 10(11):4328–4334, 2010.

[30] Jochen Greim and Karl A. Schwetz. *Boron Carbide, Boron Nitride, and Metal Borides*. Wiley-VCH Verlag GmbH and Co. KGaA, 2000. ISBN 9783527306732. doi: 10.1002/14356007.a04_295.pub2. URL `http://dx.doi.org/10.1002/14356007.a04_295.pub2`.

[31] Kenji Watanabe, Takashi Taniguchi, and Hisao Kanda. Direct-bandgap properties and evidence for ultraviolet lasing of hexagonal boron nitride single crystal. *Nature materials*, 3(6):404–409, 2004.

[32] Jiamin Xue, Javier Sanchez-Yamagishi, Danny Bulmash, Philippe Jacquod, Aparna Deshpande, K Watanabe, T Taniguchi, Pablo Jarillo-Herrero, and Brian J LeRoy. Scanning tunnelling microscopy and spectroscopy of ultra-flat graphene on hexagonal boron nitride. *Nature materials*, 10(4):282–285, 2011.

[33] RW Lynch and HG Drickamer. Effect of high pressure on the lattice parameters of diamond, graphite, and hexagonal boron nitride. *The Journal of Chemical Physics*, 44(1):181–184, 1966.

[34] Li Song, Lijie Ci, Hao Lu, Pavel B Sorokin, Chuanhong Jin, Jie Ni, Alexander G Kvashnin, Dmitry G Kvashnin, Jun Lou, Boris I Yakobson, et al. Large scale growth and characterization of atomic hexagonal boron nitride layers. *Nano letters*, 10(8):3209–3215, 2010.

[35] Y Cao, A Mishchenko, GL Yu, K Khestanova, A Rooney, E Prestat, AV Kretinin, P Blake, MB Shalom, G Balakrishnan, et al. Quality heterostructures from two

dimensional crystals unstable in air by their assembly in inert atmosphere. *arXiv preprint arXiv:1502.03755*, 2015.

[36] CR Dean, AF Young, I Meric, C Lee, L Wang, S Sorgenfrei, K Watanabe, T Taniguchi, P Kim, KL Shepard, and J Hone. Boron nitride substrates for high-quality graphene electronics. *Nature nanotechnology*, 5(10):722–726, 2010.

[37] L Ju, J Velasco Jr, E Huang, S Kahn, C Nosiglia, Hsin-Zon Tsai, W Yang, T Taniguchi, K Watanabe, Y Zhang, et al. Photoinduced doping in heterostructures of graphene and boron nitride. *Nature nanotechnology*, 9(5):348–352, 2014.

[38] Roman V Gorbachev, Ibtsam Riaz, Rahul R Nair, Rashid Jalil, Liam Britnell, Branson D Belle, Ernie W Hill, Kostya S Novoselov, Kenji Watanabe, Takashi Taniguchi, et al. Hunting for monolayer boron nitride: optical and raman signatures. *Small*, 7(4):465–468, 2011.

[39] Li Song, Lijie Ci, Hao Lu, Pavel B Sorokin, Chuanhong Jin, Jie Ni, Alexander G Kvashnin, Dmitry G Kvashnin, Jun Lou, Boris I Yakobson, et al. Large scale growth and characterization of atomic hexagonal boron nitride layers. *Nano letters*, 10(8):3209–3215, 2010.

[40] Wei Yang, Guorui Chen, Zhiwen Shi, Cheng-Cheng Liu, Lianchang Zhang, Guibai Xie, Meng Cheng, Duoming Wang, Rong Yang, Dongxia Shi, et al. Epitaxial growth of single-domain graphene on hexagonal boron nitride. *Nature materials*, 12(9):792–797, 2013.

[41] F. S. Ohuchi and M. A. Olmstead. *Semiconductors, III–VI*. John Wiley and Sons, Inc., 2001. ISBN 9780471346081. doi: 10.1002/047134608X.W3213. URL http://dx.doi.org/10.1002/047134608X.W3213.

References

[42] F. Hulliger. *Structuml Chemistry of Layer TyPe Phases.* Reidel, Dordrecht, 1976.

[43] V. Capozzi. Direct and indirect excitonic emission in gase. *Phys. Rev. B*, 23: 836–840, 1981.

[44] M. O. D. Camara, A. Mauger, and I. Devos. Electronic structure of the layer compounds gase and inse in a tight-binding approach. *Phys. Rev. B*, 65:125206, Mar 2002. doi: 10.1103/PhysRevB.65.125206. URL `http://link.aps.org/doi/10.1103/PhysRevB.65.125206`.

[45] V Grasso, G Mondio, M A Pirrone, and G Saitta. Modulation of optical constants of gate single crystals. *Journal of Physics C: Solid State Physics*, 8(1): 80, 1975.

[46] J. Z. Wan, J. L. Brebner, R. Leonelli, and J. T. Graham. Optical properties of excitons in gate. *Phys. Rev. B*, 46:1468–1471, 1992.

[47] Aishi Yamamoto, Atsushi Syouji, Takenari Goto, Erkin Kulatov, Kaoru Ohno, Yoshiyuki Kawazoe, Kazuhito Uchida, and Noboru Miura. Excitons and band structure of highly anisotropic gate single crystals. *Phys. Rev. B*, 64:035210, Jun 2001. doi: 10.1103/PhysRevB.64.035210. URL `http://link.aps.org/doi/10.1103/PhysRevB.64.035210`.

[48] G Akhundov. Second-harmonic generation in iii-vi compounds. *Sov. Phys. Semiconductors*, 7(6):826–827, 1973.

[49] I.M. Catalano, A. Cingolani, A. Minafra, and C. Paorici. Second harmonic generation in layered compounds. *Optics Communications*, 24(1):105 – 108, 1978. ISSN 0030-4018. doi: http://dx.doi.org/10.1016/0030-4018(78)90276-6. URL `http://www.sciencedirect.com/science/article/pii/0030401878902766`.

[50] N.B. Singh, D.R. Suhre, V. Balakrishna, M. Marable, R. Meyer, N. Fernelius, F.K. Hopkins, and D. Zelmon. Far-infrared conversion materials: Gallium selenide for far-infrared conversion applications. *Progress in Crystal Growth and Characterization of Materials*, 37(1):47 – 102, 1998. ISSN 0960-8974. doi: http://dx.doi.org/10.1016/S0960-8974(98)00013-8. URL `http://www.sciencedirect.com/science/article/pii/S0960897498000138`.

[51] Sidong Lei, Liehui Ge, Zheng Liu, Sina Najmaei, Gang Shi, Ge You, Jun Lou, Robert Vajtai, and Pulickel M. Ajayan. Synthesis and photoresponse of large gase atomic layers. *Nano Letters*, 13(6):2777–2781, 2013. doi: 10.1021/nl4010089.

[52] Dattatray J. Late, Bin Liu, Jiajun Luo, Aiming Yan, H. S. S. Ramakrishna Matte, Matthew Grayson, C. N. R. Rao, and Vinayak P. Dravid. Gas and gase ultrathin layer transistors. *Advanced Materials*, 24(26):3549–3554, 2012. ISSN 1521-4095. doi: 10.1002/adma.201201361. URL `http://dx.doi.org/10.1002/adma.201201361`.

[53] PingAn Hu, Zhenzhong Wen, Lifeng Wang, Pingheng Tan, and Kai Xiao. Synthesis of few-layer gase nanosheets for high performance photodetectors. *ACS Nano*, 6(7):5988–5994, 2012. doi: 10.1021/nn300889c.

[54] Yubing Zhou, Yufeng Nie, Yujing Liu, Kai Yan, Jinhua Hong, Chuanhong Jin, Yu Zhou, Jianbo Yin, Zhongfan Liu, and Hailin Peng. Epitaxy and photoresponse of two-dimensional gase crystals on flexible transparent mica sheets. *ACS Nano*, 8(2):1485–1490, 2014. doi: 10.1021/nn405529r.

[55] Zhenxing Wang, Kai Xu, Yuanchang Li, Xueying Zhan, Muhammad Safdar, Qisheng Wang, Fengmei Wang, and Jun He. Role of ga vacancy on

References

a multilayer gate phototransistor. *ACS Nano*, 8(5):4859–4865, 2014. doi: 10.1021/nn500782n.

[56] Mohammad Afzaal and Paul O'Brien. Recent developments in ii-vi and iii-vi semiconductors and their applications in solar cells. *J. Mater. Chem.*, 16: 1597–1602, 2006. doi: 10.1039/B512182E. URL `http://dx.doi.org/10.1039/B512182E`.

[57] Garry W Mudd, Simon A Svatek, Lee Hague, Oleg Makarovsky, Zakhar R Kudrynskyi, Christopher J Mellor, Peter H Beton, Laurence Eaves, Kostya S Novoselov, Zakhar D Kovalyuk, et al. High broad-band photoresponsivity of mechanically formed inse–graphene van der waals heterostructures. *Advanced Materials*, 2015.

[58] Nilanthy Balakrishnan, Zakhar R Kudrynskyi, Michael W Fay, Garry W Mudd, Simon A Svatek, Oleg Makarovsky, Zakhar D Kovalyuk, Laurence Eaves, Peter H Beton, and Amalia Patanè. Room temperature electroluminescence from mechanically formed van der waals iii–vi homojunctions and heterojunctions. *Advanced Optical Materials*, 2(11):1064–1069, 2014.

[59] Garry W. Mudd, Simon A. Svatek, Tianhang Ren, Amalia Patanè, Oleg Makarovsky, Laurence Eaves, Peter H. Beton, Zakhar D. Kovalyuk, George V. Lashkarev, Zakhar R. Kudrynskyi, and Alexandr I. Dmitriev. Tuning the bandgap of exfoliated inse nanosheets by quantum confinement. *Advanced Materials*, 25(40):5714–5718, 2013. ISSN 1521-4095. doi: 10.1002/adma.201302616. URL `http://dx.doi.org/10.1002/adma.201302616`.

[60] G. W. Mudd, A. Patanè, Z. R. Kudrynskyi, M. W. Fay, O. Makarovsky, L. Eaves, Z. D. Kovalyuk, V. Zólyomi, and V. Falko. Quantum confined acceptors and donors in inse nanosheets. *Applied Physics Letters*, 105(22):221909,

2014. doi: http://dx.doi.org/10.1063/1.4903738. URL `http://scitation.aip.`
`org/content/aip/journal/apl/105/22/10.1063/1.4903738`.

[61] N.N. Kolesnikov, E.B. Borisenko, D.N. Borisenko, and V.K. Gartman. Influence
of growth conditions on microstructure and properties of gase crystals. *Journal
of Crystal Growth*, 300(2):294 – 298, 2007.

[62] N.N. Kolesnikov, E.B. Borisenko, D.N. Borisenko, and S.I. Bozhko. Fractal
structures of dendrites in gase crystals. *Journal of Crystal Growth*, 310(14):3287
– 3289, 2008.

[63] E.B. Borisenko, N.N. Kolesnikov, D.N. Borisenko, and S.I. Bozhko. Microhard-
ness and structural defects of gase layered semiconductor. *Journal of Crystal
Growth*, 316(1):20 – 24, 2011.

[64] N.N. Kolesnikov, E.B. Borisenko, D.N. Borisenko, and A.V. Timonina. Structure
and microstructure of gate crystals grown by high-pressure vertical zone melting.
Journal of Crystal Growth, 365(0):59 – 63, 2013.

[65] A.I. Dmitriev, V.V. Vishnjak, G.V. Lashkarev, V.L. Karbovskyi, Z.D. Ko-
valjuk, and A.P. Bahtinov. Investigation of the morphology of the van der
waals surface of the inse single crystal. *Physics of the Solid State*, 53(3):
622–633, 2011. ISSN 1063-7834. doi: 10.1134/S1063783411030085. URL
`http://dx.doi.org/10.1134/S1063783411030085`.

[66] S.R Cohen, L Rapoport, E.A Ponomarev, H Cohen, T Tsirlina, R Tenne, and
C Lévy-Clément. The tribological behavior of type ii textured mx_2 (m=mo,
w; x=s, se) films. *Thin Solid Films*, 324(1–2):190 – 197, 1998. ISSN 0040-
6090. doi: http://dx.doi.org/10.1016/S0040-6090(97)01218-2. URL `http://`
`www.sciencedirect.com/science/article/pii/S0040609097012182`.

References

[67] T.W. Scharf and S.V. Prasad. Solid lubricants: a review. *Journal of Materials Science*, 48(2):511–531, 2013. ISSN 0022-2461. doi: 10.1007/s10853-012-7038-2. URL http://dx.doi.org/10.1007/s10853-012-7038-2.

[68] AA Voevodin, C Muratore, and SM Aouadi. Hard coatings with high temperature adaptive lubrication and contact thermal management: review. *Surface and Coatings Technology*, 257:247–265, 2014.

[69] Kin Fai Mak, Changgu Lee, James Hone, Jie Shan, and Tony F. Heinz. Atomically thin mos$_2$: A new direct-gap semiconductor. *Phys. Rev. Lett.*, 105:136805, Sep 2010.

[70] Andrea Splendiani, Liang Sun, Yuanbo Zhang, Tianshu Li, Jonghwan Kim, Chi-Yung Chim, Giulia Galli, and Feng Wang. Emerging photoluminescence in monolayer mos2. *Nano Letters*, 10(4):1271–1275, 2010. doi: 10.1021/nl903868w. PMID: 20229981.

[71] Michele Buscema, Joshua O. Island, Dirk J. Groenendijk, Sofya I. Blanter, Gary A. Steele, Herre S. J. van der Zant, and Andres Castellanos-Gomez. Photocurrent generation with two-dimensional van der waals semiconductors. *Chem. Soc. Rev.*, 44:3691–3718, 2015. doi: 10.1039/C5CS00106D. URL http://dx.doi.org/10.1039/C5CS00106D.

[72] Won Seok Yun, SW Han, Soon Cheol Hong, In Gee Kim, and JD Lee. Thickness and strain effects on electronic structures of transition metal dichalcogenides: 2h-m x 2 semiconductors (m= mo, w; x= s, se, te). *Physical Review B*, 85(3): 033305, 2012.

[73] Ashwin Ramasubramaniam. Large excitonic effects in monolayers of molybdenum and tungsten dichalcogenides. *Phys. Rev. B*, 86:115409, Sep 2012.

doi: 10.1103/PhysRevB.86.115409. URL `http://link.aps.org/doi/10.1103/PhysRevB.86.115409`.

[74] Oleg V. Yazyev and Andras Kis. Mos2 and semiconductors in the flatland. *Materials Today*, 18(1):20 – 30, 2015. ISSN 1369-7021. doi: http://dx.doi.org/10.1016/j.mattod.2014.07.005. URL `http://www.sciencedirect.com/science/article/pii/S1369702114002557`.

[75] Hongyi Yu, Xiaodong Cui, Xiaodong Xu, and Wang Yao. Valley excitons in two-dimensional semiconductors. *National Science Review*, 2(1):57–70, 2015. doi: 10.1093/nsr/nwu078. URL `http://nsr.oxfordjournals.org/content/2/1/57.abstract`.

[76] Andor Kormányos, Guido Burkard, Martin Gmitra, Jaroslav Fabian, Viktor Zólyomi, Neil D Drummond, and Vladimir Fal'ko. k · p theory for two-dimensional transition metal dichalcogenide semiconductors. *2D Materials*, 2(2):022001, 2015.

[77] A Kumar and PK Ahluwalia. Electronic structure of transition metal dichalcogenides monolayers 1h-mx2 (m= mo, w; x= s, se, te) from ab-initio theory: new direct band gap semiconductors. *The European Physical Journal B*, 85(6):1–7, 2012.

[78] Branimir Radisavljevic, Aleksandra Radenovic, Jacopo Brivio, V Giacometti, and A Kis. Single-layer mos_2 transistors. *Nature nanotechnology*, 6(3):147–150, 2011.

[79] FHL Koppens, T Mueller, Ph Avouris, AC Ferrari, MS Vitiello, and M Polini. Photodetectors based on graphene, other two-dimensional materials and hybrid systems. *Nature nanotechnology*, 9(10):780–793, 2014.

References

[80] Marco M Furchi, Andreas Pospischil, Florian Libisch, Joachim Burgdorfer, and Thomas Mueller. Photovoltaic effect in an electrically tunable van der waals heterojunction. *Nano letters*, 14(8):4785–4791, 2014.

[81] Mark Fox. *Optical Properties of Solids.* Oxford University Press, 2006.

[82] Hualing Zeng, Junfeng Dai, Wang Yao, Di Xiao, and Xiaodong Cui. Valley polarization in mos2 monolayers by optical pumping. *Nature nanotechnology*, 7 (8):490–493, 2012.

[83] Ji Feng, Xiaofeng Qian, Cheng-Wei Huang, and Ju Li. Strain-engineered artificial atom as a broad-spectrum solar energy funnel. *Nature Photonics*, 6(12): 866–872, 2012.

[84] Diana Y Qiu, H Felipe, and Steven G Louie. Optical spectrum of mos 2: many-body effects and diversity of exciton states. *Physical review letters*, 111(21): 216805, 2013.

[85] Alexey Chernikov, Timothy C Berkelbach, Heather M Hill, Albert Rigosi, Yilei Li, Ozgur Burak Aslan, David R Reichman, Mark S Hybertsen, and Tony F Heinz. Exciton binding energy and nonhydrogenic rydberg series in monolayer ws 2. *Physical review letters*, 113(7):076802, 2014.

[86] Keliang He, Nardeep Kumar, Liang Zhao, Zefang Wang, Kin Fai Mak, Hui Zhao, and Jie Shan. Tightly bound excitons in monolayer wse 2. *Physical review letters*, 113(2):026803, 2014.

[87] Chendong Zhang, Amber Johnson, Chang-Lung Hsu, Lain-Jong Li, and Chih-Kang Shih. Direct imaging of band profile in single layer mos2 on graphite: quasiparticle energy gap, metallic edge states, and edge band bending. *Nano letters*, 14(5):2443–2447, 2014.

[88] Xiaoyang Zhu, Nicholas R. Monahan, Zizhou Gong, Haiming Zhu, Kristopher W. Williams, and Cory A. Nelson. Charge transfer excitons at van der waals interfaces. *Journal of the American Chemical Society*, 137(26):8313–8320, 2015. doi: 10.1021/jacs.5b03141. URL `http://dx.doi.org/10.1021/jacs.5b03141`. PMID: 26001297.

[89] Jason S Ross, Sanfeng Wu, Hongyi Yu, Nirmal J Ghimire, Aaron M Jones, Grant Aivazian, Jiaqiang Yan, David G Mandrus, Di Xiao, Wang Yao, et al. Electrical control of neutral and charged excitons in a monolayer semiconductor. *Nature communications*, 4:1474, 2013.

[90] Jong-Hee Park and TS Sudarshan. *Chemical vapor deposition*, volume 2. ASM international, 2001.

[91] Bernard S Meyerson. Low-temperature silicon epitaxy by ultrahigh vacuum/chemical vapor deposition. *Applied Physics Letters*, 48(12):797–799, 1986.

[92] Jing Kong, Alan M Cassell, and Hongjie Dai. Chemical vapor deposition of methane for single-walled carbon nanotubes. *Chemical Physics Letters*, 292(4): 567–574, 1998.

[93] Yi-Hsien Lee, Xin-Quan Zhang, Wenjing Zhang, Mu-Tung Chang, Cheng-Te Lin, Kai-Di Chang, Ya-Chu Yu, Jacob Tse-Wei Wang, Chia-Seng Chang, Lain-Jong Li, et al. Synthesis of large-area mos2 atomic layers with chemical vapor deposition. *Advanced Materials*, 24(17):2320–2325, 2012.

[94] Sanfeng Wu, Chunming Huang, Grant Aivazian, Jason S Ross, David H Cobden, and Xiaodong Xu. Vapor–solid growth of high optical quality mos2 monolayers with near-unity valley polarization. *Acs Nano*, 7(3):2768–2772, 2013.

References

[95] Yi-Hsien Lee, Lili Yu, Han Wang, Wenjing Fang, Xi Ling, Yumeng Shi, Cheng-Te Lin, Jing-Kai Huang, Mu-Tung Chang, Chia-Seng Chang, et al. Synthesis and transfer of single-layer transition metal disulfides on diverse surfaces. *Nano letters*, 13(4):1852–1857, 2013.

[96] Chunxiao Cong, Jingzhi Shang, Xing Wu, Bingchen Cao, Namphung Peimyoo, Caiyu Qiu, Litao Sun, and Ting Yu. Synthesis and optical properties of large-area single-crystalline 2d semiconductor ws2 monolayer from chemical vapor deposition. *Advanced Optical Materials*, 2(2):131–136, 2014.

[97] Kai Xu, Zhenxing Wang, Xiaolei Du, Muhammad Safdar, Chao Jiang, and Jun He. Atomic-layer triangular wse2 sheets: synthesis and layer-dependent photoluminescence property. *Nanotechnology*, 24(46):465705, 2013.

[98] Jing-Kai Huang, Jiang Pu, Chang-Lung Hsu, Ming-Hui Chiu, Zhen-Yu Juang, Yung-Huang Chang, Wen-Hao Chang, Yoshihiro Iwasa, Taishi Takenobu, and Lain-Jong Li. Large-area synthesis of highly crystalline wse2 monolayers and device applications. *ACS nano*, 8(1):923–930, 2013.

[99] Jonathan C Shaw, Hailong Zhou, Yu Chen, Nathan O Weiss, Yuan Liu, Yu Huang, and Xiangfeng Duan. Chemical vapor deposition growth of monolayer mose2 nanosheets. *Nano Research*, 7(4):511–517, 2014.

[100] Xingli Wang, Yongji Gong, Gang Shi, Wai Leong Chow, Kunttal Keyshar, Gonglan Ye, Robert Vajtai, Jun Lou, Zheng Liu, Emilie Ringe, et al. Chemical vapor deposition growth of crystalline monolayer mose2. *ACS nano*, 8(5): 5125–5131, 2014.

[101] Jonathan N. Coleman, Mustafa Lotya, Arlene O'Neill, Shane D. Bergin, Paul J. King, Umar Khan, Karen Young, Alexandre Gaucher, Sukanta De, Ronan J.

Smith, Igor V. Shvets, Sunil K. Arora, George Stanton, Hye-Young Kim, Kangho Lee, Gyu Tae Kim, Georg S. Duesberg, Toby Hallam, John J. Boland, Jing Jing Wang, John F. Donegan, Jaime C. Grunlan, Gregory Moriarty, Aleksey Shmeliov, Rebecca J. Nicholls, James M. Perkins, Eleanor M. Grieveson, Koenraad Theuwissen, David W. McComb, Peter D. Nellist, and Valeria Nicolosi. Two-dimensional nanosheets produced by liquid exfoliation of layered materials. *Science*, 331(6017):568–571, 2011. doi: 10.1126/science.1194975. URL `http://www.sciencemag.org/content/331/6017/568.abstract`.

[102] Valeria Nicolosi, Manish Chhowalla, Mercouri G. Kanatzidis, Michael S. Strano, and Jonathan N. Coleman. Liquid exfoliation of layered materials. *Science*, 340 (6139), 2013. doi: 10.1126/science.1226419. URL `http://www.sciencemag.org/content/340/6139/1226419.abstract`.

[103] Goki Eda, Hisato Yamaguchi, Damien Voiry, Takeshi Fujita, Mingwei Chen, and Manish Chhowalla. Photoluminescence from chemically exfoliated mos2. *Nano Letters*, 11(12):5111–5116, 2011. doi: 10.1021/nl201874w. PMID: 22035145.

[104] L. Britnell, R. V. Gorbachev, R. Jalil, B. D. Belle, F. Schedin, A. Mishchenko, T. Georgiou, M. I. Katsnelson, L. Eaves, S. V. Morozov, N. M. R. Peres, J. Leist, A. K. Geim, K. S. Novoselov, and L. A. Ponomarenko. Field-effect tunneling transistor based on vertical graphene heterostructures. *Science*, 335(6071):947–950, 2012. doi: 10.1126/science.1218461. URL `http://www.sciencemag.org/content/335/6071/947.abstract`.

[105] L Britnell, RV Gorbachev, AK Geim, LA Ponomarenko, A Mishchenko, MT Greenaway, TM Fromhold, KS Novoselov, and L Eaves. Resonant tunnelling and negative differential conductance in graphene transistors. *Nature communications*, 4:1794, 2013.

References

[106] Woo Jong Yu, Yuan Liu, Hailong Zhou, Anxiang Yin, Zheng Li, Yu Huang, and Xiangfeng Duan. Highly efficient gate-tunable photocurrent generation in vertical heterostructures of layered materials. *Nature nanotechnology*, 8(12): 952–958, 2013.

[107] L. Britnell, R. M. Ribeiro, A. Eckmann, R. Jalil, B. D. Belle, A. Mishchenko, Y.-J. Kim, R. V. Gorbachev, T. Georgiou, S. V. Morozov, A. N. Grigorenko, A. K. Geim, C. Casiraghi, A. H. Castro Neto, and K. S. Novoselov. Strong light-matter interactions in heterostructures of atomically thin films. *Science*, 340(6138):1311–1314, 2013. doi: 10.1126/science.1235547. URL `http://www.sciencemag.org/content/340/6138/1311.abstract`.

[108] Pasqual Rivera, John R Schaibley, Aaron M Jones, Jason S Ross, Sanfeng Wu, Grant Aivazian, Philip Klement, Kyle Seyler, Genevieve Clark, Jiaqiang Yan Mandrus D. G. Ghimire, Nirmal J, Wang Tao, and Xiaodong Xu. Observation of long-lived interlayer excitons in monolayer mose2–wse2 heterostructures. *Nature communications*, 6, 2015.

[109] F Withers, O Del Pozo-Zamudio, A Mishchenko, AP Rooney, A Gholinia, K Watanabe, T Taniguchi, SJ Haigh, AK Geim, AI Tartakovskii, et al. Light-emitting diodes by band-structure engineering in van der waals heterostructures. *Nature materials*, 2015.

[110] L Wang, I Meric, PY Huang, Q Gao, Y Gao, H Tran, T Taniguchi, K Watanabe, LM Campos, DA Muller, et al. One-dimensional electrical contact to a two-dimensional material. *Science*, 342(6158):614–617, 2013.

[111] AV Kretinin, Y Cao, JS Tu, GL Yu, R Jalil, KS Novoselov, SJ Haigh, A Gholinia, A Mishchenko, M Lozada, et al. Electronic quality of graphene on different atomically flat substrates. *arXiv preprint arXiv:1403.5225*, 2014.

Chapter 2

Experimental Techniques

2.1 Sample fabrication methods

As discussed in the previous chapter, layered materials such as III-VI semiconductors and TMDCs show new properties when they are thinned down to single or few layers. The key techniques used in this work are mechanical exfoliation and peel/lift transfer. A detailed description of both fabrication methods will be presented in the following sections.

2.1.1 Mechanical exfoliation

The most common technique to produce high quality single layers of two-dimensional materials is referred as mechanical exfoliation (or the 'scoth-tape' method). It was demonstrated by Novoselov et al in 2004 in the seminal article of graphene exfoliated from graphite[1]. It is, surprisingly, a rather straightforward procedure that consists of the use of sticky tape to peel layers off bulk crystals[2] as it is schematically shown in Fig. 2.1. The first step is to press a strip of the tape onto a piece of the material (a), then peel it off (b) and press it on a substrate (c) that usually is Si finished with

SiO$_2$. This process can be repeated (d) and, eventually, single layers of the crystal will be formed with different dimensions from few microns up to a millimetre in the case of graphene[3] and tens to hundreds of microns for hBN and TMDCs [4].
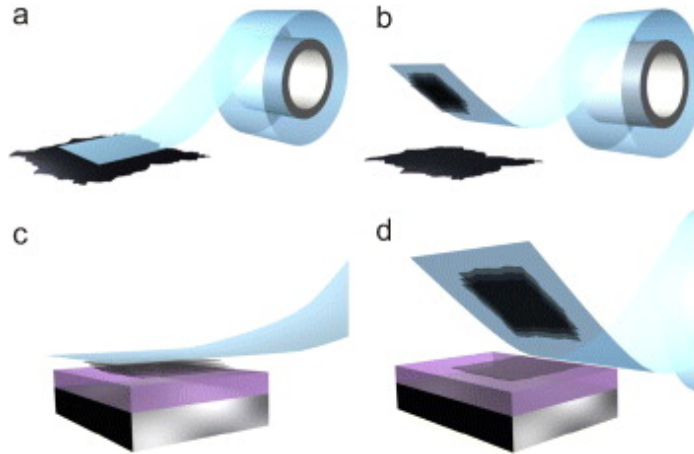

Fig. 2.1 Mechanical exfoliation [2]. (a) Sticky tape is pressed onto a crystal. (b) When the tape is peeled off, a few number of layers get attached to the tape. (c) Then it is pressed against a substrate (SiO$_2$/Si for example). (d) Repeating the process in order to get few to single layers.

Once the mechanical exfoliation procedure is carried out, the challenge is to locate the single layers on the substrate that, due to their low thickness, could be invisible even in the microscope. However, studies showed that the contrast of the films can be increased when the appropriate thickness of SiO$_2$ on Si is chosen[5–7]. It was found that an optimal thickness of 250-300 nm of SiO$_2$ on Si is needed to visualize thin films of TMDCs in the microscope, showing differing contrast colour depending on the TMDC layers thickness down to a single layer. To illustrate this, in fig. 2.2 an optical image of a MoSe$_2$ single layer surrounded by thicker flakes is presented. Note how the film colour varies from flake to flake. For more accuracy of the thickness, once the target films are localized, atomic force microscopy (AFM) is commonly used. More complex techniques to establish the film thickness have been employed. One example is Raman spectroscopy [8–10] where the separation of Raman modes depends

on the film thickness. However, this is not entirely reliable as Raman spectroscopy is sensitive to strain and charging. Another spectroscopy technique is photoluminesence when a transition from indirect to direct band gap in the material occurs, as it will be discussed later in this chapter.
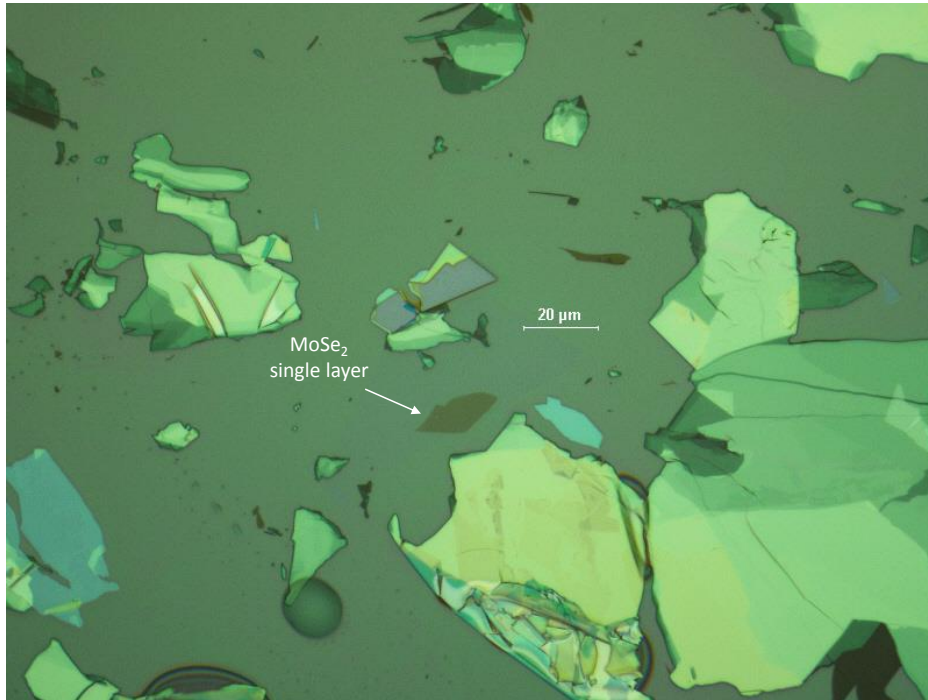

Fig. 2.2 Optical image of a mechanical exfoliated MoSe2 single layer surrounded by thicker flakes on a SiO_2/Si substrate. The film colour indicates difference in thickness.

2.1.2 Heterostructure fabrication

In chapters 5 and 6 an optical study of light-emitting diodes based on quantum wells (QW) made of van der Waals heterostructures will be presented. These heterostructures were produced via multiple 'peel' and 'lift' transfer processes described below [11, 12].

An example of a single quantum well structure is $hBN/Gr_B/2hBN/MoS_2/2hBN/Gr_T/hBN$. This requires stacking of single or few layers of the materials. Fig. 2.3A-F and Fig.

2.4 show the schematic for the processes. For the 'peel' process a flake is mechanically exfoliated (Fig. 2.3A), as described in section 2.1.1, onto a poly(methyl methacrylate) (PMMA) double layer. Then the bottom polymer is dissolved releasing the membrane which then floats on top of the liquid as is schematically shown in fig. 2.3B,C. The PMMA membrane is then inverted and aligned onto the target crystal, Fig. 2.3D. The two crystals are brought into contact (Fig. 2.3E) and heated until the PMMA adheres to the target substrate. Once the flake has adequately stuck to the target crystal the PMMA membrane is brought back, fig. 2.3F. The flake due to the strong van der Waals interaction peels from the PMMA onto the target flake.
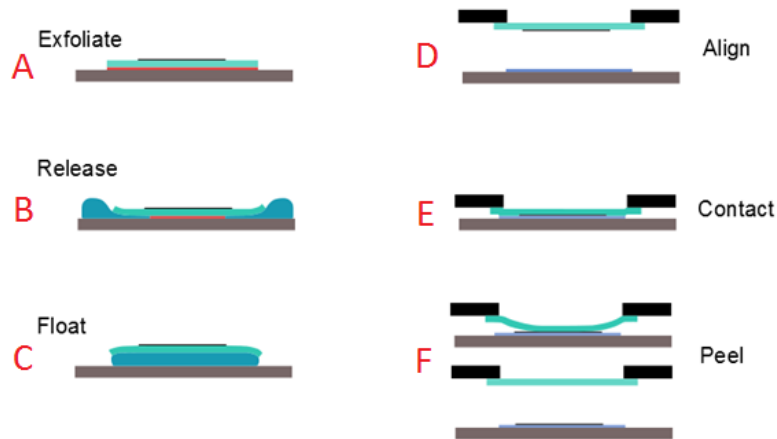

Fig. 2.3 Schematic procedure for the 'peel' process. (A) A flake is mechanical exfoliated form bulk on PMMA, (B) and released from this polymer (C) shich then floats on liquid. (D) The flake is inverted and aligned onto the target crystal, (E) and then brought into contact. (F) The flake gets stacked in the substrate when peeling the PMMA.

For the 'lift' process the membrane is produced in the same way as shown in Fig. 2.3. Instead of peeling the flake onto the target crystal, a large flake on the membrane is used to collect a smaller flake on the substrate. The flake to be lifted is exfoliated onto a second SiO_2/Si wafer.
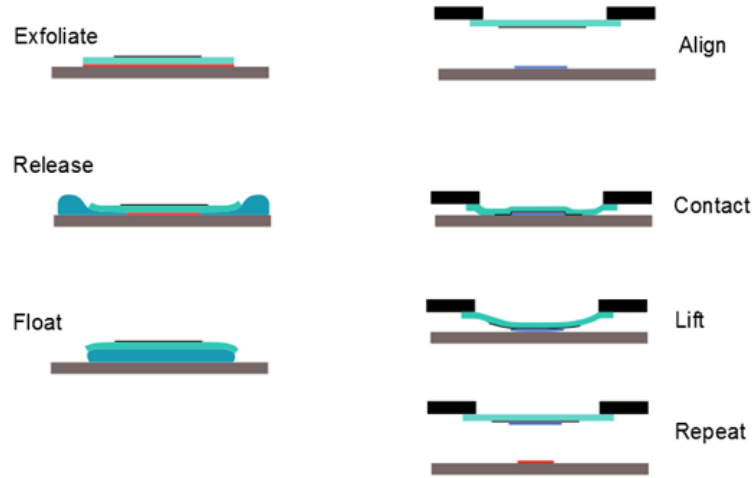
Fig. 2.4 Schematic procedure for the 'lift' process. The septs are similar to the ones decribed in 2.3. Instead of peeling the flake onto the target crystal, a large flake on the membrane is used to collect a smaller flake on the substrate. The flake to be lifted is exfoliated onto a second SiO_2/Si wafer.

In this work multiple QW heterostructures are also studied, such as the double QW hBN/Gr_B/2hBN/MoS_2/2hBN/MoS_2/2hBN/Gr_T/hBN. Fig. 2.5 shows the fabrication route for the multiple QW (MQW) structure. Firstly a graphene flake is peeled from a PMMA membrane to an hBN crystal on the Si/SiO_2 substrate, Fig. 2.5A. After this a thin hBN tunnel barrier is peeled from the PMMA membrane onto the hBN-Gr_B structure, Fig. 2.5B. A thin hBN spacer carrying a single layer TMDC crystal (lifted from a second substrate) is then peeled from the membrane, thus completing the first well, Fig. 2.5C. This process can be repeated as shown in Fig. 2.5D to produce a double QW and even further to produce multiple QW structures.

2.2   Optical techniques

In the next four experimental chapters, the main subject will be the study of optical properties of the materials previously discussed. Two essential physical phenomena in
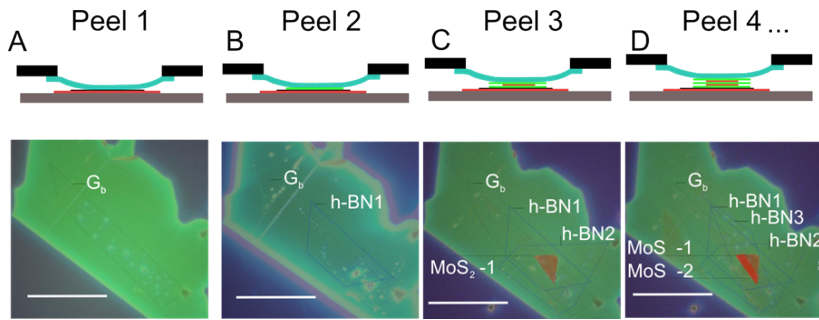
Fig. 2.5 (A-D) Schematic and differential interference contrast microscope images with semi-transparent dark field images overlaid to highlight flake edges, for the multiple QW structures. Scale bar is 50 μm.

these chapters will be photoluminescence and electroluminescence. In the next sections a description and experimental techniques employed to measure these phenomena will be discussed.

2.2.1 Luminescence in solids

Luminescence is the emission of light in materials that is not a result of heating (called incandescence). This emission can be caused by external excitations with light or an electrical current[13].

Fig. 2.6 shows an schematic of the luminescence process in a solid. We can consider two bands with a relatively large gap between them. Electrons (holes) are injected into the conduction (valence) band and relax to the lowest available level. The photon is emitted when an electron from the conduction band undergoes a transition into an empty (hole) state in the ground valence band. These empty state are generated by the injection of holes.

The spontaneous emission rate for a two level system where N is the population
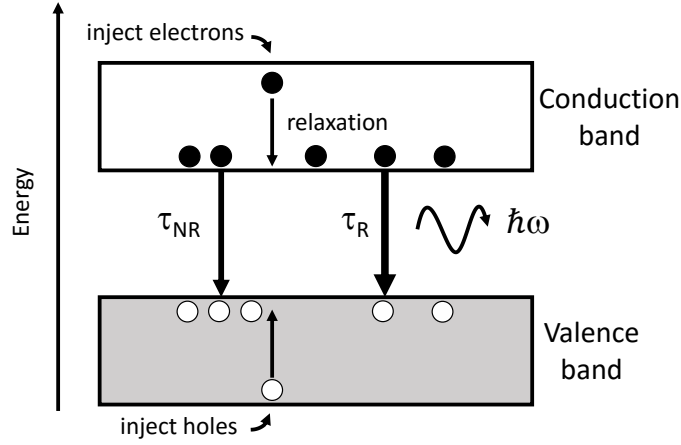
Fig. 2.6 Schematic of luminescence process in a solid. Electrons (holes) are injected into the conduction (valence) band before recombination that produces the emission of a photon.

in the upper level at time t:

$$\left(\frac{dN}{dt}\right)_{radiative} = -AN \tag{2.1}$$

This spontaneous emission is ruled by the Einstein coefficient A and the rate equation can be solved to give:

$$N(t) = N(0)exp(-At) = N(0)exp(-t/\tau_R) \tag{2.2}$$

where $\tau_R = A^{-1}$ is the radiative lifetime of the transition. A is proportional to the other Einstein coefficient B that determines the absorption probability:

$$A = \frac{8\pi h\nu^3}{c^3}B \tag{2.3}$$

Hence, if the transitions have large absorption coefficients, they will have high emission probability and short radiative lifetime. However, according to eq. 2.1, even if there is high absorption but low population N in the upper level, emission intensity

may be low, for example, due to strong non-radiative processes

The electrons relax to within $\sim k_B/T$ of the conduction band. The holes follow a similar series of relaxations. Thus light is only emitted within a narrow energy range, which is further modified by strong excitonic effects.

An important factor that needs to be taken into account is that electrons excited in the conduction band can relax into the valence band by emitting phonons or be trapped by defects. As no photons are emitted in this process, this is called non-radiative relaxation. Eq. 2.1 needs to be rewritten by adding a new non-radiative lifetime τ_{NR}:

$$\left(\frac{dN}{dt}\right)_{total} = -\frac{N}{\tau_R} - \frac{N}{\tau_{NR}} = -N\left(\frac{1}{\tau_R} + \frac{1}{\tau_{NR}}\right) \tag{2.4}$$

so the total τ will be:

$$\frac{1}{\tau} = \frac{1}{\tau_R} + \frac{1}{\tau_{NR}} \tag{2.5}$$

Let's define the term η_R as the luminescence efficiency given by the ratio of the radiative emission rate to the total de-excitation rate:

$$\eta_R = \frac{N/\tau_R}{N\left(1/\tau_R + 1/\tau_{NR}\right)} = \frac{1}{1 + \tau_R/\tau_{NR}} \tag{2.6}$$

If $\tau_R \ll \tau_{NR}$, $\eta_R \approx 1$, the maximum possible light is emitted. If $\tau_R \gg \tau_{NR}$, $\eta_R \approx 0$, light emission is very inefficient. Therefore radiative lifetime should be much shorter than non-radiative lifetime in order to achieve efficient luminescence.

For the luminescence process described above, if the excitation takes place with light, it is called photoluminescence. If it is with electrical current, electroluminescence. We will describe both in the following subsections together with the spectroscopy techniques used to measure them.

Photoluminescence (PL) is the emission of a photon created due to a recombination of an electron-hole pair that is optically created in the first step (see fig. 2.7). This occurs when the excitation photon energy is greater than the band gap (E_g) of the material, and an electron is then excited from the valence to the conduction band. Electrons and holes relax to the bottom of their bands and recombine leading to the creation of a photon with energy around the band gap E_g [13] (excitonic effects are neglected here). This case, illustrated in fig. 2.7a occurs in materials with direct band gap, where the bottom of the conduction band and the top of the valence band are observed for the same k-vector in the Brillouin zone. Fig. 2.7b shows an opposite case, where they occur for different k-vectors, this leads to an indirect band gap where a phonon assisted transition is needed for the radiative recombination process and, therefore, the efficiency is low. For this reason, as it will be discussed in the next section, commercial applications for luminescence devices are made of direct band gap semiconductors.

It was mentioned above that PL intensity depends on the absorption of photons. This process can be described as a function of thickness in a finite material as the intensity of the light $I(h)$ travelling across in the form $I(h) = I_0 e^{\alpha h}$, where I_0 is the intensity of the light before enters the material, α is the absorption coefficient and h the thickness. In chapter 3 PL intensity will be described as a function of film thickness by using this equation.

A common term to calculate the efficiency of the PL process is the Quantum Yield (QY) defined as:

$$QY \equiv \frac{\text{\# of photons emitted}}{\text{\# of photons absorbed}} \qquad (2.7)$$

43
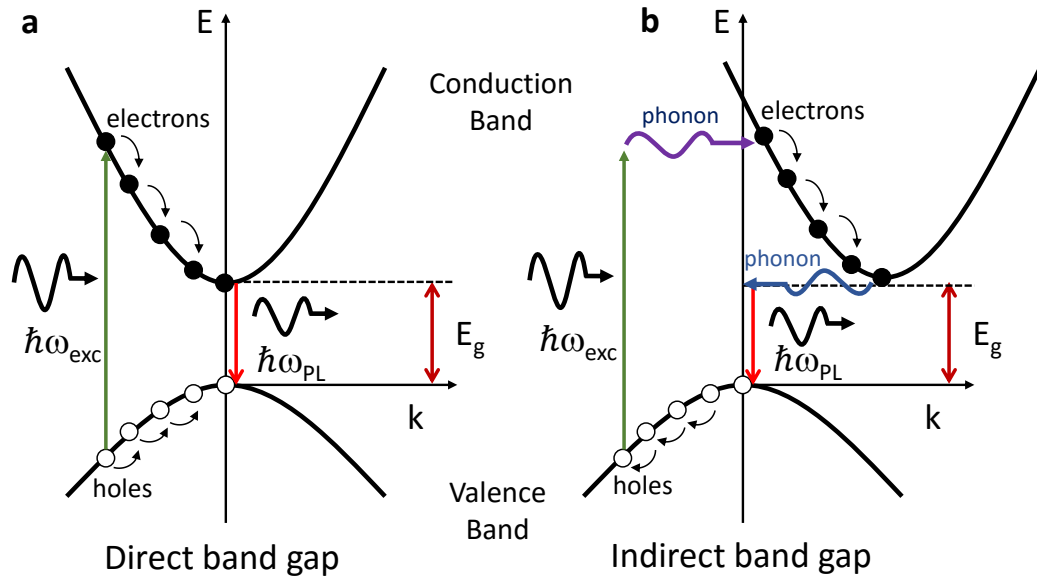
Fig. 2.7 Diagram of photoluminescence processes in semiconductor materials. (a) In a direct band gap material the top of the valence band coincide with the bottom of the conduction band. When a photon with an energy $\hbar\omega_{exc}$ excites electrons and holes, after relaxation of electrons (holes) to the bottom (top) of the band, a photon with energy $E_g = \hbar\omega_{PL}$ is emitted. (b)For indirect band gap materials, the bottom of the conduction band and top of the valence band are at different k-vectors. Here, a phonon assisted transition is needed, after relaxation a photon and phonon are emitted.

Photoluminescence measurements

In order to detect PL we use a set-up schematically shown in fig. 2.8. A diode laser used as the excitation source, typically with a wavelength of 532 nm. The laser beam (green solid line) is guided with a mirror to a 50-50 beam-splitter, 50% of the light goes to a power meter and the rest to a 50x microscope objective with a 25 mm working distance that focuses the beam onto the target sample achieving a laser spot of ∼ 1-2 μm diameter with a power range from ∼10 nW to 25 mW. The light emitted by the sample (red dashed line) is collected with the same objective (NA=0.55) and guided to a slit of a 0.5 m spectrometer, where a 4 cm focal length lens is used for focussing light on the entrance slit of the spectrometer. Additional devices such as a white light

source and a CMOS camera in the setup are necessary for visualizing the sample. The spectrometer is equipped with 3 different gratings: 300, 600 and 1200 lines/mm for achieving different spectral resolution and a nitrogen cooled CCD camera with a chip of 100x1240 pixels. The sample is placed in vacuum in a cold finger inside a continuous flow He cryostat that allows to cool down to $\sim$ 6 K and achieve controllable temperatures up to room-T with a heater. Heavy duty XY stages are used to move the entire cryostat with an accuracy of $\sim$1 μm in order to align different parts of the sample under the excitation laser.

Electroluminescence

Electroluminescence (EL) is the generation of light in response to an electric current passing through a material[13]. As in the case of PL, EL is generated in an active region due to a radiative recombination of electrons and holes.

The first observation of the phenomenon of EL was on silicon carbide (SiC) in 1907 by H. J. Round in the Marconi Labs[14]. The first light-emitting diode (LED) was developed using the same material a few years later in 1923 [15]. Since then, LEDs have been rapidly developing in a large variety of ways and nowadays have many applications such as smart displays, efficient lighting, traffic lights, car lights, etc. This made solid-state LEDs a key component of today's technology [16]. Different materials and structures have been used for design and fabrication such as nitrides (GaN, InGaN)[17], porous silicon[18], polymers[19], carbon nanotubes[20], quantum dots[21], III-V materials (GaAs, AlGaAs, GaAsP, GaP)[22] and more recently graphene[23] and other 2D materials [24–26].

In fig. 2.9A-B the band diagram of the most common LEDs can be observed. It consists on a $p-n$ junction with heavily doped p and n regions to generate holes in the p-region and electrons in the n-region. In (A) when $V_b = 0$, a depletion region is
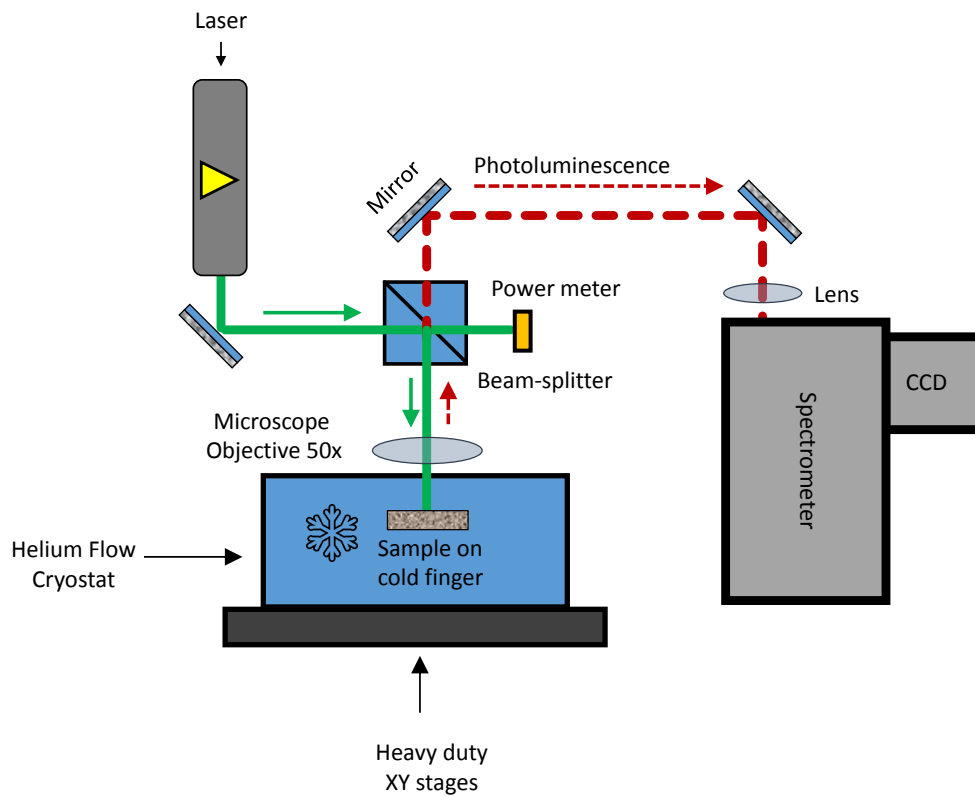
Fig. 2.8 Schematic diagram of the experimental cw μPL setup. A laser beam (green solid line) is directed and focused to the target sample with a 50x (NA=0.55) objective in a continuous flow He cryostat. PL emitted (red dashed line) is collected and guided to a spectrometer and a CCD camera. The laser power is monitored with a power meter after the beam-splitter. The cryostat is suitable for electrical measurements and is also used for EL.
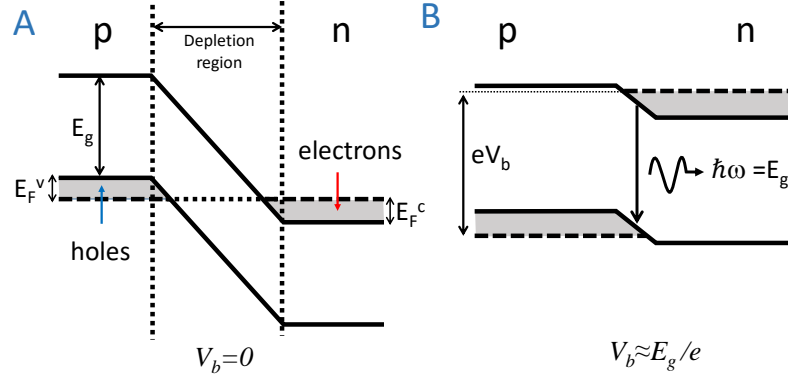
Fig. 2.9 Band diagram of a LED that consists on a $p-n$ junction. In (a) $V_b = 0$, no light is emitted due to absence of electrons and holes in the depletion region. (b) $V_b \approx E_g/e$, light is emitted the spatial overlap of e and h populations.

formed in between the two regions so light cannot be emitted. When $V_b \approx E_g/e$ (fig. 2.9B), current starts to flow through the device. A region is formed at the junction where both electrons and holes are present. Analogous to PL, light is emitted when the electrons recombine with holes in that region [13]. The emission wavelength will depend on E_g and on the binding of the $e-h$ pairs due to excitonic effects.

In this work, electroluminescence from LEDs made of 2D materials was measured using the μPL setup showed in fig. 2.8. The cryostat is equipped with wires that are able to connect the contacts in the sample to a voltage source (Keithley 2400) so when the laser is blocked, the setup allows to measure EL by injecting carriers with the source. Further experiments of PL or EL bias dependence with either the laser or electrical excitation are possible to perform with this setup.

Quantum efficiency

The conversion of electrical energy into light is the main function of an LED. So it is necessary to calculate the efficiency of a device, in other words, the proportion of the injected carriers converted into photons[27].

The internal quantum efficiency, or luminescence efficiency (described in sec. 2.2.1),

is the ratio of the radiative electron-hole recombination to the total (radiative and non-radiative) recombination coefficient (eq. 2.6). This parameter is important for a semiconductor material because it determines the efficiency of light generation. However, for a LED we need to take into account the injected current and compare it with the number of photons emitted [28, 29].

The internal photon flux Φ (photons per second), generated within a volume V of the semiconductor, is directly proportional to the carrier-pair injection rate R (pairs/cm^3-s). In the steady-state, the injected carrier concentration $\Delta n = R\tau$ (recombination rate = injection rate), where τ is the total recombination lifetime ($1/\tau = 1/\tau_R + 1/\tau_{NR}$). The injection of RV carrier pairs per second therefore leads to the generation of a photon flux:

$$\Phi = \eta_R RV = \eta_R i/e \tag{2.8}$$

where e is the electron charge and i the injection current.

The efficiency with which the internal photons can be extracted from the LED is known as the extraction efficiency η_e. The output photon flux Φ_o is related to the internal photon flux Φ:

$$\Phi_o = \eta_e \Phi = \eta_e(\eta_R i/e) \tag{2.9}$$

where the extraction efficiency η_e indicates how much of the internal photon flux Φ is transmitted outside the device.

We can define a single quantum efficiency based on both η_e and η_R as external quantum efficiency (EQE):

$$\eta_{ext} \equiv \eta_e \eta_R \tag{2.10}$$

48

So the output photon flux will be:

$$\Phi_o = \eta_{ext}i/e \tag{2.11}$$

We can think of η_{ext} as the ratio of the output photon flux Φ_o to the injected electron flux i/e.

Finally, we can deduce the LED optical power P:

$$P = h\nu\Phi_o = \eta_{ext}h\nu i/e \tag{2.12}$$

With this definition of EQE, an estimate of the efficiency of the devices described in chapters 5 and 6 will be carried out. Additional losses in the system used to measure EL that need to be taken into account in order to perform this calculation are discussed in Appendix B.

Another aspect to consider is the light extraction efficiency of an LED. Photons are created inside of a material rather than in air, where we would ultimately like them to go. Different techniques are employed to maximize the light extraction on the device depending on the chip refraction index. One way to improve the situation is to immerse the chip in a surrounding index that is higher than air. Typically, the material used is silicone, with an index of roughly 1.47. A dome larger than the chip is typically used, since it results in very little refraction (ray deviation) and therefore does not cause further issues. Additionally, a silver film is deposited below the active materials to reflect the light emitted [30].

There are two primary types of LED package architectures that have emerged over the years: dome and flat cast. For the most part, the LED manufacturers supply dome or flat cast LED sources, and optical designers choose from an array of off-the-shelf output optics or design their own optic implementations. Typically, when the most important specification in your application is total lumens, dome out-coupling optics

provide a better solution. [30].

In fig. 2.10 it shown the domed system geometry on the left and the relative source flux exiting the dome on the first pass to the right. A relatively modest dome radius of 1 mm allows >99.9% of the chip flux to exit.
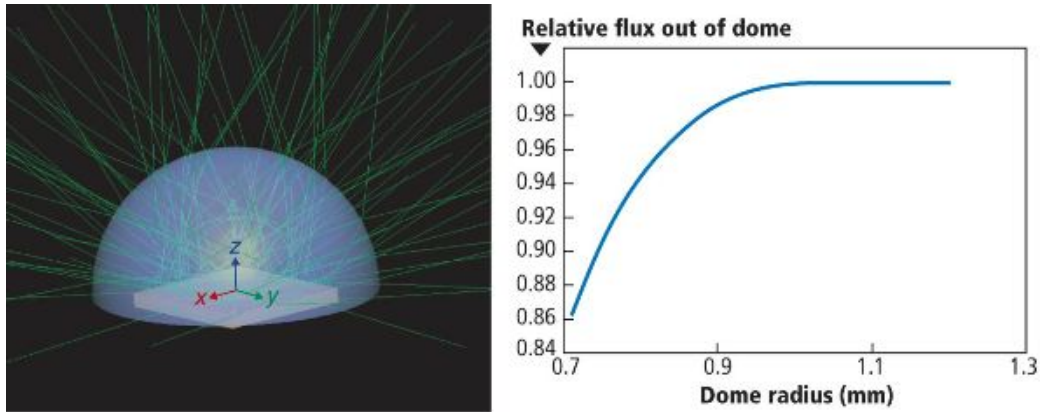

Fig. 2.10 Light flux on a domed LED system (left side). Relative flux out of dome plotted as a function of dome radius (right side) [30]

.

2.2.2   Time-resolved spectroscopy

Time-resolved spectroscopy is the technique to study dynamic processes that occur in materials after illumination. It is commonly used to study with temporal and spectral resolution the luminescence of excited materials such as semiconductors [31].

As discussed in previous subsections, semiconductor materials can emit light by different ways such as EL and PL. When the excitation needed in the process is not continuous but pulsed, study of the dynamics of the generated light can be performed. This allows the measurement of the overall lifetime τ described in section 2.2.1, that is given by $1/\tau = 1/\tau_R + 1/\tau_{NR}$.

An essential instrument to measure PL with temporal resolution is the Streak Camera. This tool is able to transform a temporal profile of a light pulse into a

spatial profile. It is achieved when the light pulse enters the camera and a deflection of the photons is rapidly executed in such a way that the photons that arrive first are detected in a different place on the detector that those that arrive later in the detector. When the streak camera is combined with a spectrometer, both temporal and spectral resolution can be achieved.

The experimental setup used in this work to measure time-resolved PL is presented in fig. 2.11. It is very similar to the standard μPL system of fig. 2.8. The excitation source is one of the main differences. A pulsed Ti:Sapphire laser tuned to 808 nm (red solid line) is directed into a second harmonic generator (SHG) in order to obtain a higher photon energy beam (blue solid line) at 404 nm. Then this light is guided with a 50:50 beam splitter to the sample focused with a 20x objective lens and to a power meter. The PL emitted is collected and directed with the same objective lens to the spectrometer. The light diffracted by the spectrometer is studied with a CCD camera to acquire the spectrum and with a streak camera that allows to acquire a time-resolved PL signal.

2.2.3   Raman spectroscopy

When light is scattered by atoms in a crystal lattice, most photons are scattered elastically with the same wavelength as the incident light. This process is known as elastic or Rayleigh scattering. However, a small amount of light is scattered following an inelastic process that results in a difference in wavelength [32]. The process leading to this inelastic scattering is called the Raman effect and occurs with a change in vibrational, rotational or electronic energy of atoms in the crystal [33].

Raman scattering was discovered by Sir C. V. Raman who won the Nobel prize for his work. A diagram of the different processes is shown in fig. 4.4. If the material being studied is illuminated by monochromatic light, like a laser, the spectrum of the
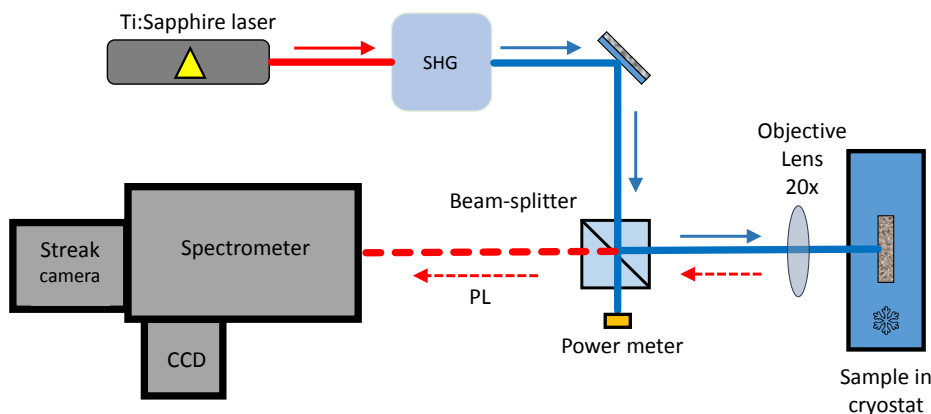
Fig. 2.11 Schematic diagram of the experimental time-resolved μPL setup. A laser beam (red solid line) enters to a second harmonic generator, then the resulting beam (blue solid line) is guided and focused to the target sample in a continuous He flow cryostat. PL emitted (red dashed line) is collected and directed to a spectrometer equipped with a CCD and a streak camera. Additional devices in the setup allow the measurement of laser power, movement of cryostat and visualisation of sample.

scattered light consists of a strong line (the laser line, green arrow) with the same frequency as the incident illumination together with lines with weaker intensities on either side shifted from the strong line by frequencies from a few to about 3500 cm^{-1}. The lines with frequency lower (higher) than the exciting laser are called Stokes (anti-Stokes) lines, red and purple arrows respectively. Each line corresponds to a different vibrational mode of the crystal.

Raman spectroscopy is, nowadays, an important technique used to identify molecules with the vibrational and rotational modes [34] and it has been an essential technique to investigate two-dimensional materials [8, 9, 35, 36]. In this work it was used to study the stability of two-dimensional films in chapter 4. The equipment employed was an InVia Renishaw System with a 532 nm laser for excitation at room temperature.
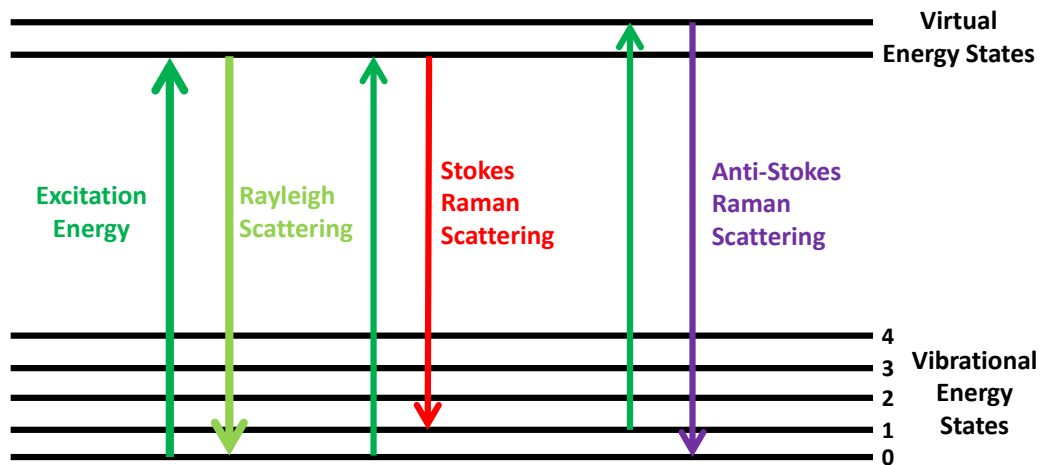
Fig. 2.12 Energy diagram showing the states and processes in Raman signal: Rayleigh scattering in light green arrow, Stokes Raman scattering in red and anti-Stokes scatering in purple. Excitation line is shown in green.

References

[1] Kostya S Novoselov, Andre K Geim, SV Morozov, D Jiang, Y_ Zhang, SV Dubonos, IV Grigorieva, and AA Firsov. Electric field effect in atomically thin carbon films. *Science*, 306(5696):666–669, 2004.

[2] K S Novoselov and A H Castro Neto. Two-dimensional crystals-based heterostructures: materials with tailored properties. *Physica Scripta*, 2012(T146):014006, 2012. URL `http://stacks.iop.org/1402-4896/2012/i=T146/a=014006`.

[3] Jeehwan Kim, Hongsik Park, James B. Hannon, Stephen W. Bedell, Keith Fogel, Devendra K. Sadana, and Christos Dimitrakopoulos. Layer-resolved graphene transfer via engineered strain layers. *Science*, 342(6160):833–836, 2013. doi: 10.1126/science.1242988. URL `http://www.sciencemag.org/content/342/6160/833.abstract`.

[4] AV Kretinin, Y Cao, JS Tu, GL Yu, R Jalil, KS Novoselov, SJ Haigh, A Gholinia,

References

A Mishchenko, M Lozada, et al. Electronic properties of graphene encapsulated with different two-dimensional atomic crystals. *Nano letters*, 14(6):3270–3276, 2014.

[5] Hai Li, Jumiati Wu, Xiao Huang, Gang Lu, Jian Yang, Xin Lu, Qihua Xiong, and Hua Zhang. Rapid and reliable thickness identification of two-dimensional nanosheets using optical microscopy. *ACS Nano*, 7(11):10344–10353, 2013. doi: 10.1021/nn4047474. PMID: 24131442.

[6] Ying Ying Wang, Ren Xi Gao, Zhen Hua Ni, Hui He, Shu Peng Guo, Huan Ping Yang, Chun Xiao Cong, and Ting Yu. Thickness identification of two-dimensional materials by optical imaging. *Nanotechnology*, 23(49):495713, 2012. URL `http://stacks.iop.org/0957-4484/23/i=49/a=495713`.

[7] M M Benameur, B Radisavljevic, J S Héron, S Sahoo, H Berger, and A Kis. Visibility of dichalcogenide nanolayers. *Nanotechnology*, 22(12):125706, 2011. URL `http://stacks.iop.org/0957-4484/22/i=12/a=125706`.

[8] Hong Li, Qing Zhang, Chin Chong Ray Yap, Beng Kang Tay, Teo Hang Tong Edwin, Aurelien Olivier, and Dominique Baillargeat. From bulk to monolayer mos2: Evolution of raman scattering. *Advanced Functional Materials*, 22(7): 1385–1390, 2012. ISSN 1616-3028. doi: 10.1002/adfm.201102111. URL `http://dx.doi.org/10.1002/adfm.201102111`.

[9] Changgu Lee, Hugen Yan, Louis E. Brus, Tony F. Heinz, James Hone, and Sunmin Ryu. Anomalous lattice vibrations of single- and few-layer mos2. *ACS Nano*, 4 (5):2695–2700, 2010. doi: 10.1021/nn1003937. PMID: 20392077.

[10] Qing Hua Wang, Kourosh Kalantar-Zadeh, Andras Kis, Jonathan N Coleman,

and Michael S Strano. Electronics and optoelectronics of two-dimensional transition metal dichalcogenides. *Nature nanotechnology*, 7(11):699–712, 2012.

[11] L Wang, I Meric, PY Huang, Q Gao, Y Gao, H Tran, T Taniguchi, K Watanabe, LM Campos, DA Muller, et al. One-dimensional electrical contact to a two-dimensional material. *Science*, 342(6158):614–617, 2013.

[12] AV Kretinin, Y Cao, JS Tu, GL Yu, R Jalil, KS Novoselov, SJ Haigh, A Gholinia, A Mishchenko, M Lozada, et al. Electronic quality of graphene on different atomically flat substrates. *arXiv preprint arXiv:1403.5225*, 2014.

[13] Mark Fox. *Optical Properties of Solids*. Oxford University Press, 2006.

[14] Henry J Round. A note on carborundum. *Electrical world*, 49(6):309, 1907.

[15] OV Losev. Luminous carborundum [silicon carbide] detector and detection with crystals. *Telegrafiya i Telefoniya bez Provodov*, 44:485–494, 1927.

[16] Nikolay Zheludev. The life and times of the led—a 100-year history. *Nature Photonics*, 1(4):189–192, 2007.

[17] FA Ponce and DP Bour. Nitride-based semiconductors for blue and green light-emitting devices. *Nature*, 386:351–359, 1997.

[18] Nobuyoshi Koshida and Hideki Koyama. Visible electroluminescence from porous silicon. *Applied Physics Letters*, 60(3), 1992.

[19] RH Friend, RW Gymer, AB Holmes, JH Burroughes, RN Marks, CDDC Taliani, DDC Bradley, DA Dos Santos, JL Bredas, M Lögdlund, et al. Electroluminescence in conjugated polymers. *Nature*, 397(6715):121–128, 1999.

[20] Phaedon Avouris, Marcus Freitag, and Vasili Perebeinos. Carbon-nanotube photonics and optoelectronics. *Nature photonics*, 2(6):341–350, 2008.

References

[21] Yasuhiro Shirasaki, Geoffrey J Supran, Moungi G Bawendi, and Vladimir Bulović. Emergence of colloidal quantum-dot light-emitting technologies. *Nature Photonics*, 7(1):13–23, 2013.

[22] E Fred Schubert, Thomas Gessmann, and Jong Kyu Kim. *Light emitting diodes*. Wiley Online Library, 2005.

[23] Xiaomu Wang, He Tian, Mohammad Ali Mohammad, Cheng Li, Can Wu, Yi Yang, and Tian-Ling Ren. A spectrally tunable all-graphene-based flexible field-effect light-emitting device. *Nature communications*, 6, 2015.

[24] Andreas Pospischil, Marco M Furchi, and Thomas Mueller. Solar-energy conversion and light emission in an atomic monolayer pn diode. *Nature nanotechnology*, 9(4):257–261, 2014.

[25] Rui Cheng, Dehui Li, Hailong Zhou, Chen Wang, Anxiang Yin, Shan Jiang, Yuan Liu, Yu Chen, Yu Huang, and Xiangfeng Duan. Electroluminescence and photocurrent generation from atomically sharp wse2/mos2 heterojunction p–n diodes. *Nano letters*, 14(10):5590–5597, 2014.

[26] Yu Ye, Ziliang Ye, Majid Gharghi, Hanyu Zhu, Mervin Zhao, Yuan Wang, Xiaobo Yin, and Xiang Zhang. Exciton-dominant electroluminescence from a diode of monolayer mos2. *Applied Physics Letters*, 104(19):193508, 2014.

[27] NG Sze. *Physics of semiconductor devices*. Wiley, 2007.

[28] John M Senior and M Yousif Jamro. *Optical fiber communications: principles and practice*. Pearson Education, 2009.

[29] Gerd Keiser. *Optical fiber communications*. Wiley Online Library, 2003.

[30] Tomas Davenport. *Design considerations for enhancing LED efficiency (MAGA-ZINE).* LEDs magazine, 2012.

[31] Andrew M. Weiner. *Ultrafast Time-Resolved Spectroscopy.* John Wiley and Sons, Inc., 2008. ISBN 9780470473467. doi: 10.1002/9780470473467.ch9. URL `http://dx.doi.org/10.1002/9780470473467.ch9`.

[32] Norman Colthup. *Introduction to infrared and Raman spectroscopy.* Elsevier, 2012.

[33] Shu-Lin Zhang. *Raman spectroscopy and its application in nanostructures.* John Wiley & Sons, 2012.

[34] Katrin Kneipp, Harald Kneipp, Irving Itzkan, Ramachandra R Dasari, and Michael S Feld. Ultrasensitive chemical analysis by raman spectroscopy. *Chemical reviews*, 99(10):2957–2976, 1999.

[35] Andrea C Ferrari and Denis M Basko. Raman spectroscopy as a versatile tool for studying the properties of graphene. *Nature nanotechnology*, 8(4):235–246, 2013.

[36] Sheneve Z Butler, Shawna M Hollen, Linyou Cao, Yi Cui, Jay A Gupta, Humberto R Gutierrez, Tony F Heinz, Seung Sae Hong, Jiaxing Huang, Ariel F Ismach, et al. Progress, challenges, and opportunities in two-dimensional materials beyond graphene. *ACS nano*, 7(4):2898–2926, 2013.

Chapter 3

Photoluminescence of two-dimensional GaTe and GaSe thin films

3.1 Introduction

In section 1.2.3 a description of the properties of III-VI semiconductor materials was discussed. In this chapter we present a photoluminescence study of thin films of two of these compounds: GaTe and GaSe.

GaTe and GaSe are layered crystals with strong covalent in-plane inter-atomic bonding (with some ionic contributions [1, 2]) and weaker predominantly van der Waals inter-plane bonding [1, 3–6]. Single tetralayer having hexagonal in-plane structure consists of two Ga atoms and two Se or Te atoms: Se-Ga-Ga-Se and Te-Ga-Ga-Te [5], see fig. 1.4. The bulk lattices are built by stacking tetralayers, which can occur in several ways[1, 3, 4]. For the wider studied GaSe, several types of stacking exist leading to different polytypes[1, 3, 4]. For GaTe having a monoclinic crystal lattice [2, 7] the polytypic behavior has not been observed [2, 6]. This may lead to lower

probability of stacking faults in GaTe resulting in a clearer observation (compared to GaSe) of the excitonic features in optical experiments [2, 6].

Here we study optical properties of GaSe and GaTe thin films as a function of the film thickness. Continuous-wave (cw) and time-resolved low-temperature micro-PL for a wide range of films from 200 nm to sub-nm (one tetralayer) thicknesses is measured. PL intensity is used to monitor the quantum yield (QY), which falls dramatically for thin films: integrated cw PL intensity drops by up to $\approx 10^4 - 10^5$ when the film thickness is reduced from 200 to 10 nm. Apart from the PL intensity decrease, no trends in spectral and temporal properties have been observed as a function of the film thickness. A similar observation of reduced PL for thin films was previously reported for InSe and was explained as transition to a band-structure with an indirect bandgap, the conclusion also based on the observed PL blue-shift with the decreasing film thickness [8]. Such indirect bandgap behavior is also theoretically predicted for single monolayers of GaSe and GaTe [5]. However, no size-quantization effects as in InSe are observed in our work for GaSe and GaTe. Furthermore neither shows any trends as a function of the film thickness observed in time-resolved PL. Based on the evidence from both cw and time-resolved spectroscopy, we develop a model that shows that the PL reduction can be explained by non-radiative carrier escape to surface states. Our explanation does not require introduction of the direct-to-indirect band-gap transition. Following the cw PL data analysis, we identify a critical film thickness of about 30-40 nm, below which the non-radiative carrier escape changes its character. In our work we use thin films encapsulated in Si_3N_4. The importance of surface states predicted by our results emphasizes the need for development of novel surface passivation for III-VI films, possibly involving oxygen-free dielectrics such as boron nitride [9].

60

3.2 Experimental procedure

3.2.1 Fabrication of GaTe and GaSe samples

Single crystals of GaSe and GaTe were grown by high-pressure vertical zone melting in graphite crucibles under Ar pressure. The detailed description of crystal growth processes and properties of GaSe and GaTe can be found in Refs.[10–13]. The gallium mono-chalcogenides used in this work were synthesized from high-purity materials: Ga and Te - 99.9999 %, Se - 99.9995 %. The crystals used are high-resistivity semi-conductors with low free carrier absorption, which has been confirmed in infra-red transmission measurements. GaSe and GaTe have n-type and p-type conductivity, re-spectively. This is a typical observation: selenides are usually of n-type conductivity, whereas tellurides often can have conductivity of both types, even within one ingot. Such behaviour is attributed to deviations of the crystal composition from stoichiome-try, usual for metal chalcogenides. In our case the n-type conductivity clearly indicates some excess of Ga (donor) in GaSe, whereas the p-type conductivity indicates a slight excess of Te (acceptor) in the GaTe.

The III-VI thin films studied in this work were fabricated using the mechanical exfoliation method from bulk described in section 2.1.1. The films were deposited on Si/SiO_2 substrates. Within the first 15 minutes after the exfoliation/deposition procedure, the films were placed in a plasma-enhanced chemical vapor deposition (PECVD) reactor and a 15 nm Si_3N_4 layer was deposited with the sample maintained at a temperature of 300 °C. This process leads to a complete encapsulation of the films, protecting them from interaction with oxygen and water present in the atmosphere. Although $_3N_4$ molecules could be grown in between multilayer films, this technique shows no substantial effects in the PL signal. Films with a wide variety of thicknesses were obtained from single unit cell (single monolayer, ML) shown in Fig.3.1 to 200
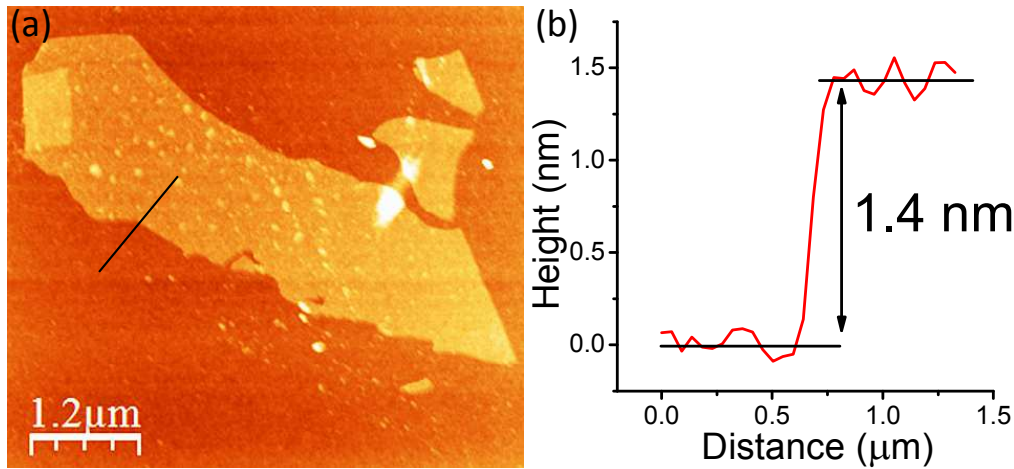
Fig. 3.1 (a) AFM image of a GaSe thin film having a single unit cell thickness. This film is obtained by mechanical exfoliation. (b) Cross-sectional plot along the black line in (a).

nm. The thicknesses of the films were determined using atomic force microscopy.

3.2.2 Optical characterization methods

Optical characterization of the GaTe and GaSe thin films was carried out using the low-temperature micro-photoluminescence (μPL) technique described in section 2.2.1. The sample was placed on a cold finger in a continuous flow He cryostat at a temperature of 10 K. A microscope objective was placed outside the cryostat and was used to focus the laser beam on the sample (in a $\approx 2\mu$m spot) and to collect the photoluminescence (PL) from the films. In continuous-wave (cw) experiments, PL was detected with a 0.5 m spectrometer and a liquid nitrogen cooled charge coupled device. For cw PL excitation a laser emitting at 532 nm (2.33 eV) was used. Ultra-fast spectroscopy experiments was obtained with the setup described in section 2.2.2. The excitation of GaTe and GaSe layers was performed using frequency-doubled titanium-sapphire (wavelength of 415 nm) focused on the sample in $\approx 10\mu$m spot. Time-resolved PL (TRPL) was detected using a streak camera. The temporal resolution of the experimental setup

for the time-resolved measurements was 10 ps.

3.3 Experimental results

3.3.1 Low-temperature cw PL results: GaTe

Fig.3.2(a) shows typical PL spectra measured for Si_3N_4-capped GaTe thin films at $T = 10K$ (cw laser power P=2 mW in Fig.3.2(a)). In this figure, in all films but the one with the thickness h_{film}=8 nm, a narrow feature is observed around 1.75 eV. It is observed at an energy where free exciton (FE) PL is expected. We will therefore refer to such features in GaTe (and GaSe) films as a 'free exciton' peak as opposed to the low energy broad PL bands corresponding to excitons bound to impurities/defects and observed in the range of 1.6-1.7 eV for GaTe. In reality the free excitons may also experience disordered potential and degree of localization as evidenced from a relatively broad line of 10-15 meV (varying from sample-to-sample). A different behaviour of the FE peak compared to the bound excitons has been verified in temperature and power-dependent measurements and is further confirmed in time-resolved studies discussed below. Although all spectra in Fig.3.2(a) show these typical features, no clear trend is observed in the relative intensities of the impurity/defect band and the FE peak as a function of h_{film}. The FE peak is usually pronounced in thick films of around 100 nm and above. In thin films as in the 8 nm film in the figure, the FE peak could only be observed under high power pulsed excitation, when the impurity/defect states saturate.

No size-quantization effects have been observed in GaTe thin films in contrast to InSe in Ref.[8] where the PL blue-shift was observed for thin layers. The sharpest PL feature in GaTe spectra, the FE line, has the peak energy varying from film to film in the range 1.74-1.76 eV. There are also no clear trends for the PL peak energies of the
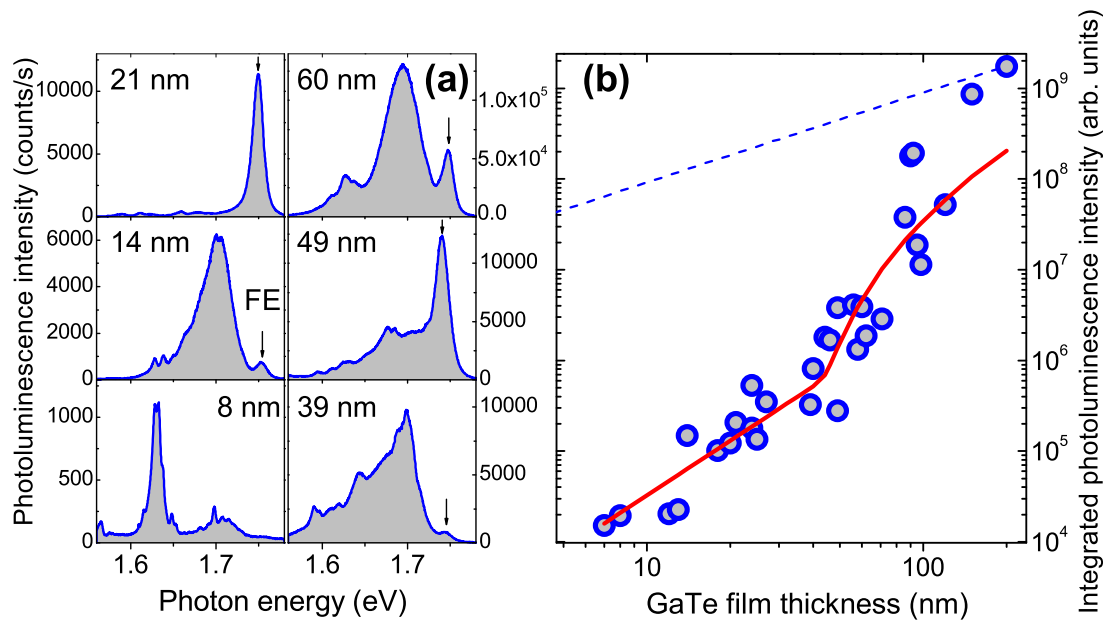
Fig. 3.2 Low-temperature cw PL results for GaTe thin films. (a) PL spectra for films of various thicknesses. h_{film} is marked on the plots. On the plot for the film with h_{film}=49 nm FE marks the free exciton peak observed at similar energies for all films on the figure except the one with h_{film}=8 nm. (b) Symbols show experimentally measured integrated PL (for T=10K) for the cw laser excitation power of 2 mW at 532 nm (2.33 eV). Dashed line shows expected variation of PL following the change in the absorption of the thin film assuming constant quantum efficiency. Solid line shows the results of calculations using the model discussed in text.

localized exciton band as a function of the film thickness.

A pronounced feature of PL measured from different films is a dramatic decrease of PL intensity with the decreasing thickness of the material [see Fig.3.2(b)]: about 10^5 (10^4) decrease is observed between 200 (100) and 7 nm. The strongest PL reduction by 3 orders of magnitude is detected between 200 and 40 nm. For h_{film} <40 nm, the PL intensity reduction slows down and decreases less than 100 times when h_{film} is varied between 40 and 7 nm. The dotted curve in the graph shows the expected PL intensity behaviour assuming thickness-independent quantum efficiency, i.e. when reduction in PL is caused solely by the reduced absorption and reduced number of e-h pairs created by the laser. The curve is described by the expression $I_{PL} = I_{GaTe}[1 - exp(-\alpha_{GaTe}h_{film})]$, where I_{GaTe} is the PL intensity for films with $h_{film} \approx$200 nm. The absorption coefficient α_{GaTe}=5000 cm^{-1} is used according to Ref.[14]. A discrepancy by a few orders of magnitude between the experiment and the calculated curve in a wide range of film thicknesses is evident on the graph.

3.3.2 Low-temperature cw PL results: GaSe

Fig.3.3(a) shows typical PL spectra measured for Si$_3$N$_4$-capped films of GaSe of several thicknesses between 8 and 70 nm (the cw laser power of 2 mW is used). The PL signal is observed in a range from 1.95 to 2.05 eV, which is below the emission energy of the free exciton, reported to be around 2.10 eV for some high purity GaSe samples (see e.g. Ref.[15]). The detected PL in our samples thus comes from impurity/defect states. The observed localized states may originate from the non-stoichiometric composition of the bulk material.

In Fig.3.3(a) it is observed that PL spectra of thin films <20 nm usually consist of multiple pronounced lines (a feature similar to GaTe in Fig.3.2(a)), whereas PL spectra tend to exhibit a single pronounced peak for thicker films. PL linewidths
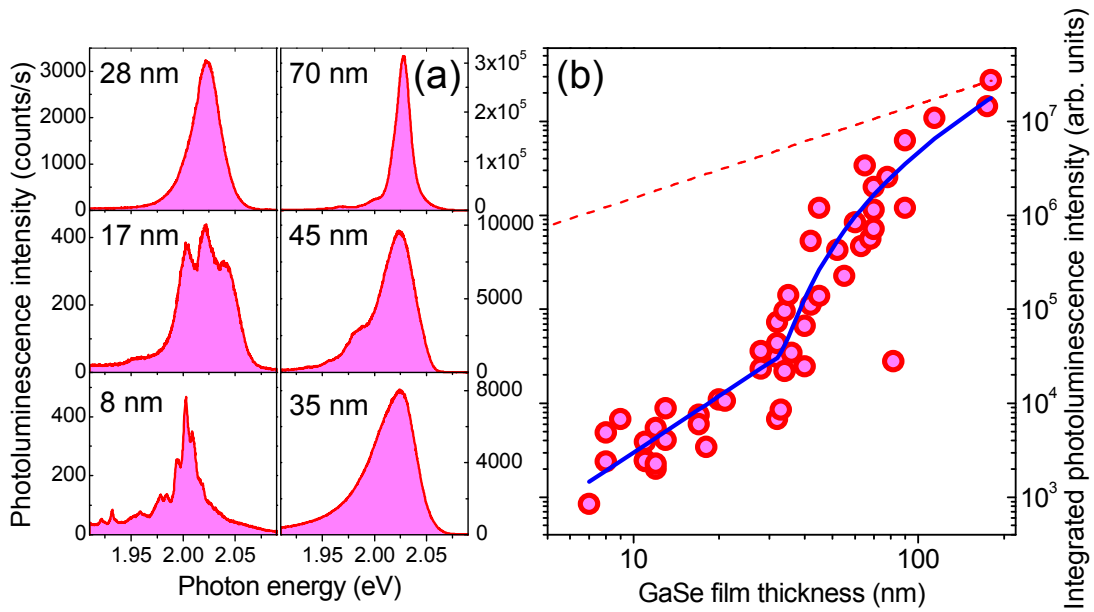
Fig. 3.3 Low-temperature cw PL results for GaSe thin films. (a) PL spectra for films of various thicknesses. (b) Symbols show experimentally measured integrated PL (for $T=10$K) for the cw laser excitation power of 2 mW at 532 nm (2.33 eV). Dashed line shows expected variation of PL following the change in the absorption of the thin film assuming constant quantum efficiency. Solid line shows the results of calculations using the model discussed in text.

vary between 15 and 60 meV. From the data measured on more than 50 films, we observe that PL peak energies have a very wide distribution in the range 1.99-2.06 eV. Similarly to GaTe, there is no evidence for size-quantization effects as a function of the film thickness.

In some GaSe films, when excited with low power (<1 μW), sharp PL lines with linewidths from 1 to 5 meV are observed (see fig. 3.4a-f). These lines are similar to the sharp features in the PL spectrum for the 8 nm film in Fig.3.3(a) and occur in the whole energy range of GaSe PL. This 'quantum dot-like' emissions can be originated from bound excitons due to impurities in the crystal [16]. A detailed study of such defect states is outside the scope of this thesis.

Further evidence for exciton localization in thin films is a pronounced Stokes blue-shift observed when the laser excitation density is increased as shown in Fig.3.5. The inset in Fig.3.5(a) shows that the PL peak shifts by $\approx$20 meV as the cw laser power is changed from 0.01 to 2 mW. This is a typical behaviour observed in all GaSe films independent on the film thickness: at high power, saturation of some of the PL features is observed accompanied in most cases with a blue-shift of PL of around 10-20 meV. This is a typical behaviour observed for localized exciton states in semiconductors, the effect also similar to the state-filling phenomenon in semiconductor quantum dots [17]. In some GaSe films, if the optical pumping is further increased, for example, by using pulsed excitation, a relatively broad free exciton feature can be observed, as shown in Fig.3.5(b). This behaviour is in agreement with that observed previously in GaTe and GaSe under pulsed excitation, and is related to saturation of the localized states having relatively slow recombination rates [18].

Similarly to GaTe films, a significant decrease of PL intensity with the decreasing thickness of the GaSe films is observed [see Fig.3.3(b)] by about 2×10^4 between 200 and 7 nm. As for the GaTe films in Fig.3.2(b), the strongest PL reduction by 3 orders
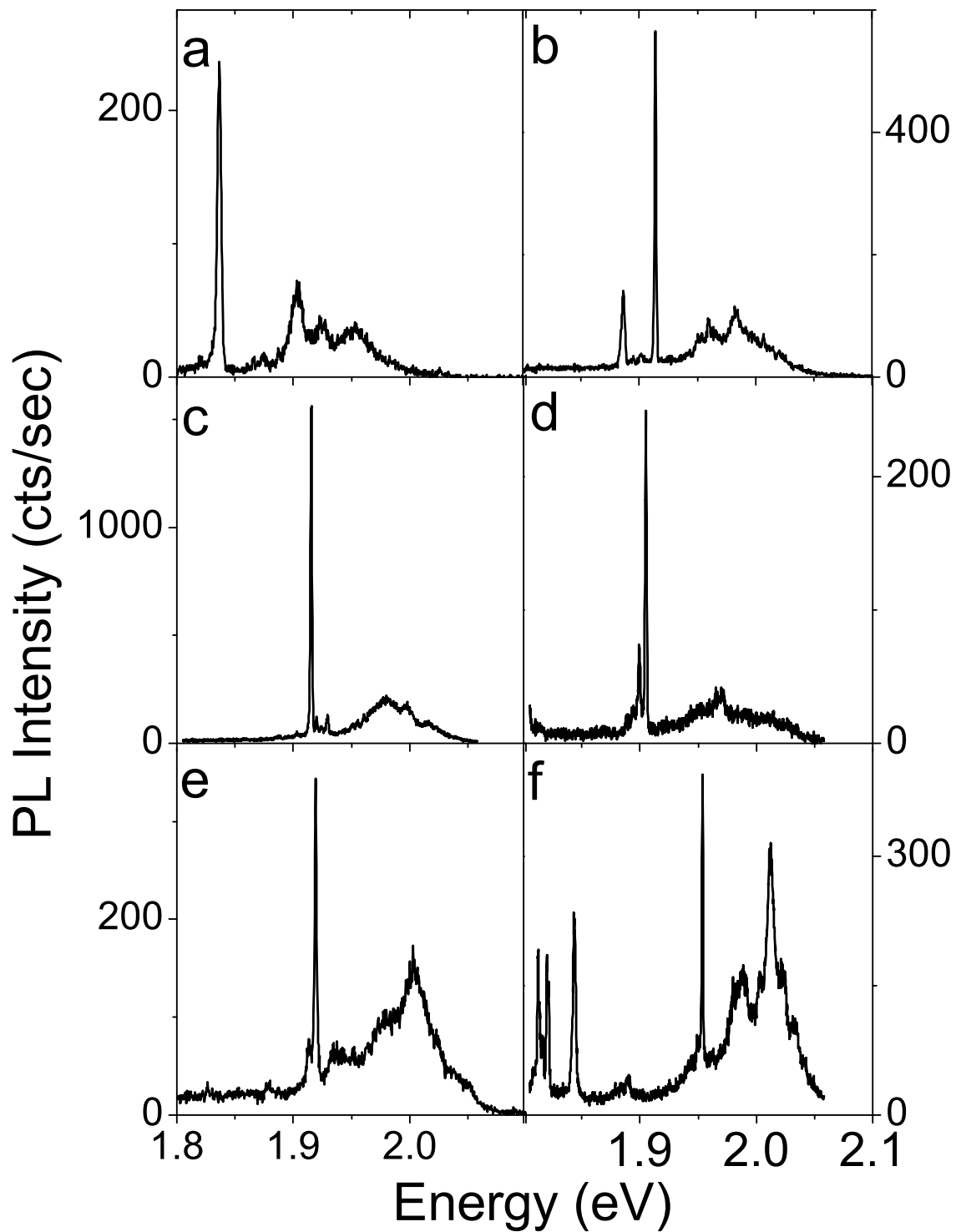
Fig. 3.4 (a-f) GaSe narrow emission lines at low excitation power (500 nW) on thick films (~80-100 nm). The linewidth of these peaks fluctuate from 1 to 5 meV.
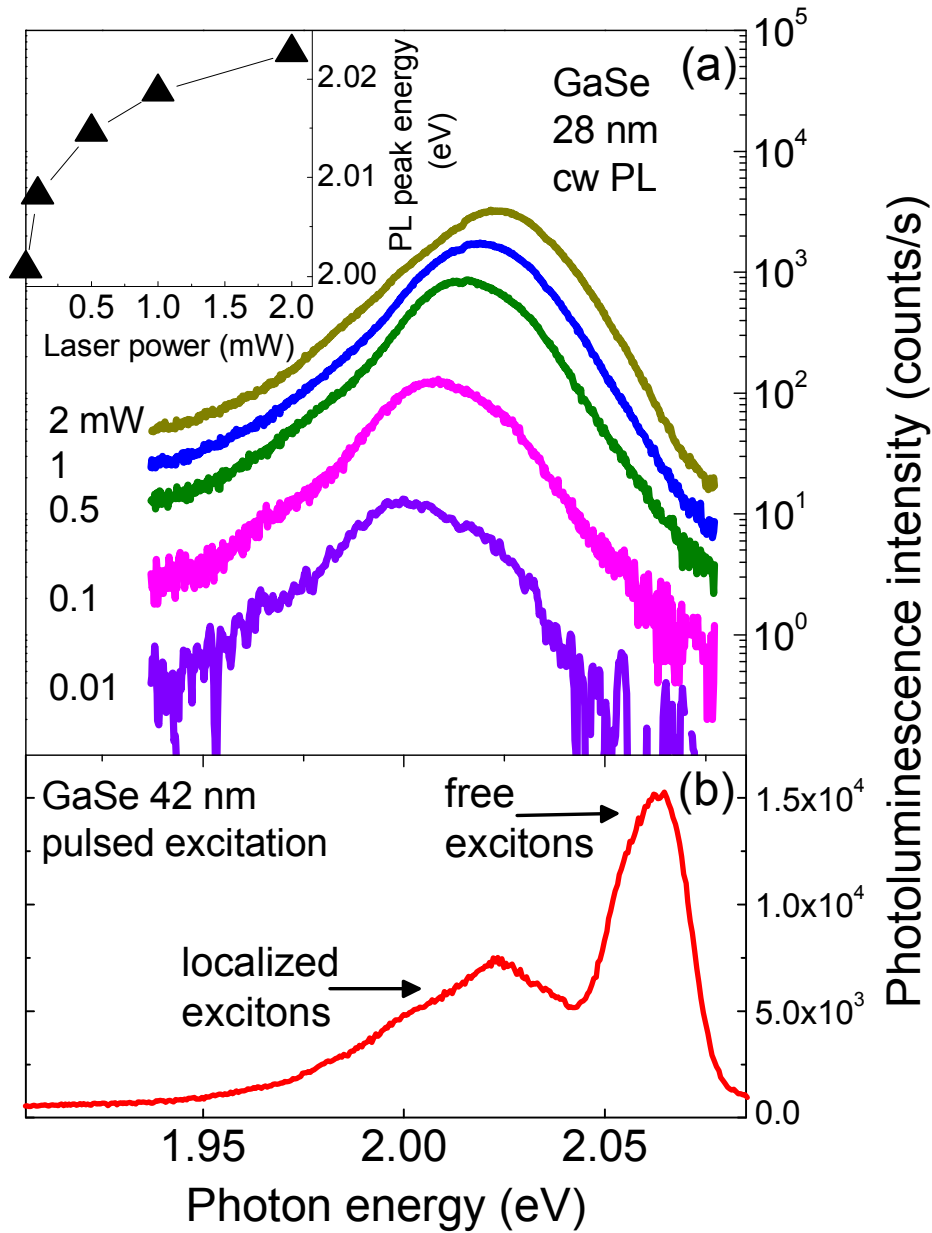
Fig. 3.5 (a) Observation of the Stokes shift of localized exciton states in cw PL of a 28 nm thick GaSe films. Excitation with a cw laser at 532 nm (2.33 eV) is used at T=10K. (a) Observation of the free exciton feature in PL of a 42 nm thick GaSe films. The time-integrated PL is shown measured for pulsed laser excitation at 420 nm (2.95 eV) with a power of 1 mW. A free exciton peak having a linewidth of $\approx$25 meV is observed at 2.06 eV.

of magnitude is detected between 200 and 30 nm. For $h_{film} <$30 nm, the PL intensity reduction slows down and is about 30 when h_{film} is varied between 30 and 7 nm. Similar to GaTe in films with $h_{film} <$7 nm PL is completely suppressed. Similarly to Fig.3.2, we show a curve that describes PL reduction due to the reduced absorption only calculated as $I_{PL} = I_{GaSe}[1 - exp(-\alpha_{GaSe}h_{film})]$, where I_{GaSe} is the PL intensity for films with h_{film}=150 nm and the absorption coefficient α=1000 cm^{-1} [14]. As for GaTe, a significant discrepancy by a few orders of magnitude between the experimental results and the calculated curve is clear in a wide range of film thicknesses.

3.3.3   Time-resolved PL measurements

In order to shed further light on the results of cw PL and also provide further experimental foundation for our theoretical model, time-resolved PL experiments have been carried out. We find that TRPL measurements show no trend in life-times as a function of the film thickness in both GaTe and GaSe as discussed below. Fig.3.6 shows typical TRPL data obtained at $T \approx$10K.

For GaTe, the difference in the origin of the PL features observed in Fig.3.2(a) is further evidenced in TRPL. Fig.3.6(a,b) shows data for a 27 nm thick film exhibiting a behavior typical for films with h_{film} in the range 20 to 200 nm. Fig.3.6(a) presents a streak-camera scan clearly showing two pronounced features at 1.76 eV and 1.71 eV corresponding to the free and localized excitons, respectively. The free exciton peak intensity decays considerably faster than that of the localized states, which does not change significantly on the time-scale of 130 ps shown in the figure. Fig.3.6(b) shows two decay curves measured at 1.76 eV (gray) and 1.71 eV (red). Fitting with single exponential decay functions is shown with blue curves and gives 10 ps for the free exciton and 150 ps for the localized states. The inset shows a PL decay curve measured at 1.73 eV on a larger time-scale, exhibiting an almost complete decay of the

signal at 1 ns. We find similar life-times for other films, however no clear dependence on the film thickness is observed: the free exciton PL decay time varies between 5 and 25 ps and that for the localized states between 100 and 200 ps. The lifetimes also weakly depend on the laser excitation power. We also note the rise times of $\approx$15 and 20 ps for the free and localized states, respectively, indicating fast carrier relaxation into light-emitting states.

Similar difference between the PL dynamics of the high and low energy part of the spectrum is observed for GaSe thin films in Fig.3.6(c),(d). Here a behaviour resembling the Stokes shift shown in Fig.3.5 is observed: as the carrier density decreases with time after the laser pulse, the PL intensity maximum progressively moves to lower energy. Fig.3.6(d) details the behaviour shown in Fig.3.6(c): two decay curves measured at 2.055 eV (gray) and 2.035 eV (red) are shown. In the center of the PL band at 2.035 eV, the non-exponential decay occurs with a characteristic time of 400 ps, which also shows a slow-decaying component. At around 2.055 eV, the initial PL time-dependence can be well fitted with a single-exponential decay with a lifetime of $\approx$40 ps, dominated most likely by carrier relaxation to lower energy. The complex behaviour in GaSe films occurs due to the partial saturation of the states at short times after the excitation pulse and fast relaxation to lower energy. We find similar behaviour for films with other thicknesses. Similarly to GaTe no clear dependence on the film thickness is observed and the rise times of $\approx$30 ps are found for the localized states.

3.3.4   Modeling

In order to describe the observed trend of photoluminescence (PL) intensity as a function of film thickness h_{film} in GaSe and GaTe thin films we have developed a simplified rate equation model described in detail in the Appendix A. As shown in Fig.3.7 we assume that the film is divided in three regions: (1) two regions of thickness
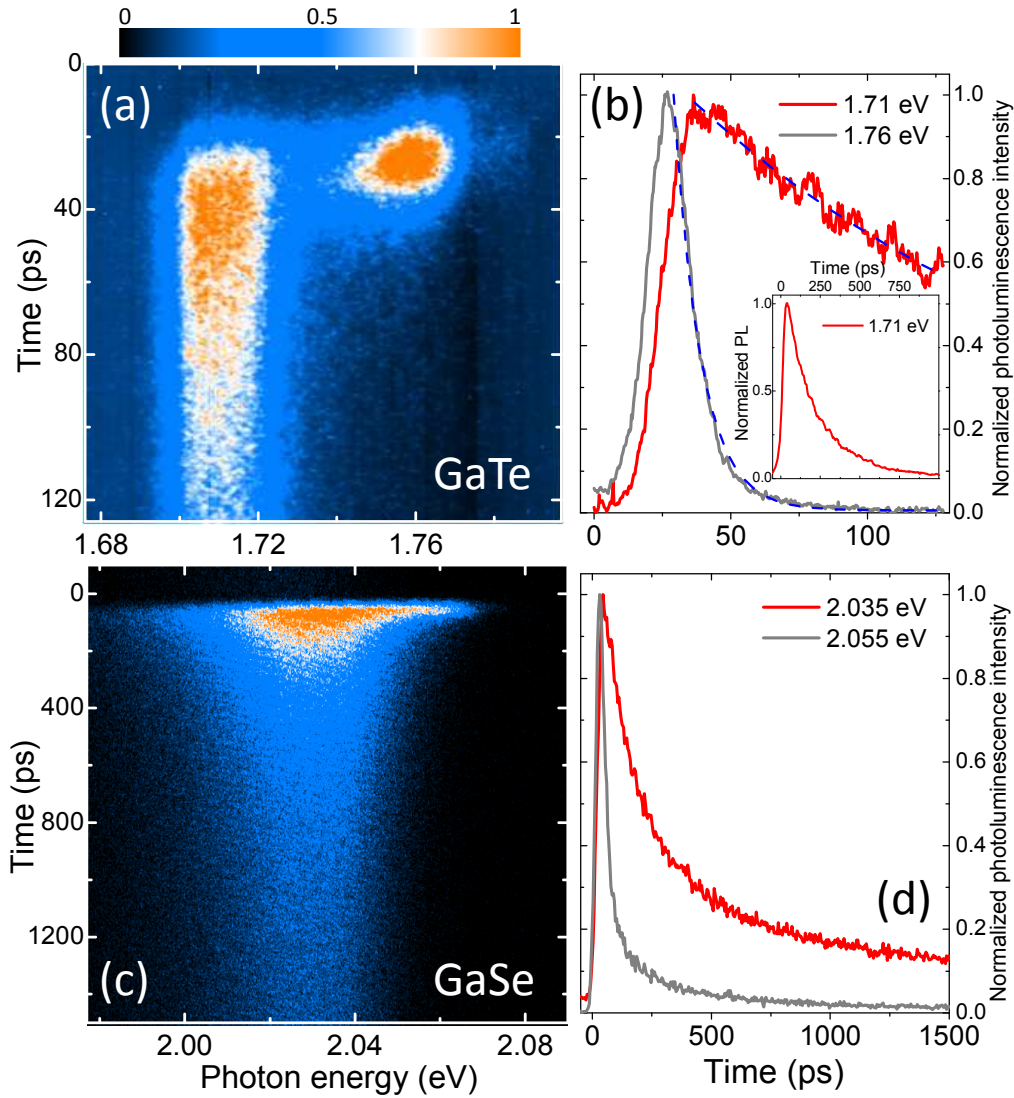
Fig. 3.6 Time-resolved PL data for GaTe (a,b) and GaSe (c,d) thin films measured at T=10K. Note different time-scales for the GaTe and GaSe data. (a) and (c) show streak-camera scans. (b) and (d) show PL traces measured at 1.76 (gray) and 1.71 eV (red) for GaTe and 2.055 (gray) and 2.035 eV (red) for GaSe. Blue lines in (b) show fitting with a single exponential functions as described in text.

h_0 near the film surfaces where fast carrier relaxation to surface traps occurs leading to non-radiative carrier escape; (2) a 'normal' region of thickness $h_{film} - 2h_0$ in the film's central part not containing the traps where the photo-excited carriers can escape into regions (1), where they undergo non-radiative decay. Here the h_0 value may be associated with a depletion depth or an average surface trap radius[19]. As shown in Fig.3.7 there are two possibilities: in Fig.3.7(a), where $h_{film} > 2h_0$ and both regions of type (1) and (2) exist; and in Fig.3.7(b), for films with $h_{film} \leq 2h_0$, where region (2) is not present. The model assumes that light absorption and PL occurs in both types of regions. In both regions, e-h pairs relax with the time τ_{rel} into the 'PL states' giving rise to radiative recombination. Non-radiative escape from the 'PL states' is neglected.

In region (1), in first approximation the average time it takes for the carrier/e-h pair to escape non-radiatively is proportional to half the thickness of region (1) (can be understood as the average time for the carrier to reach the surface or as the overlap of the wavefunction of the carrier and the trap). In region (2), the non-radiative escape time reflects the average time it takes for a carrier or an e-h pair to reach any of the regions (1). The underlying mechanism for this process may be depletion and band-bending expected at the film surface leading to charge separation and non-radiative decay [19]. We assume that once the carrier or e-h pair has reached region (1) it escapes non-radiatively. In first approximation, the average time it takes a carrier/e-h pair to reach region (1) is proportional to half the thickness of region (2). Thus we introduce non-radiative decay times in region (1) as $\tau_{nr1} = (h_0/2)/u_1$ for $h_{film} > 2h_0$, and $\tau_{nr1} = (h_{film}/4)/u_1$ for $h_{film} \leq 2h_0$. In region (2) it is $\tau_{nr2} = (h_{film}/2 - h_0)/u_2$. Here u_1 and u_2 have dimensions of m/s. In the case of region 2 where effectively we assume ballistic exciton (or electron/hole) transport preceding the non-radiative escape, u_2 can be interpreted as the average carrier velocity.
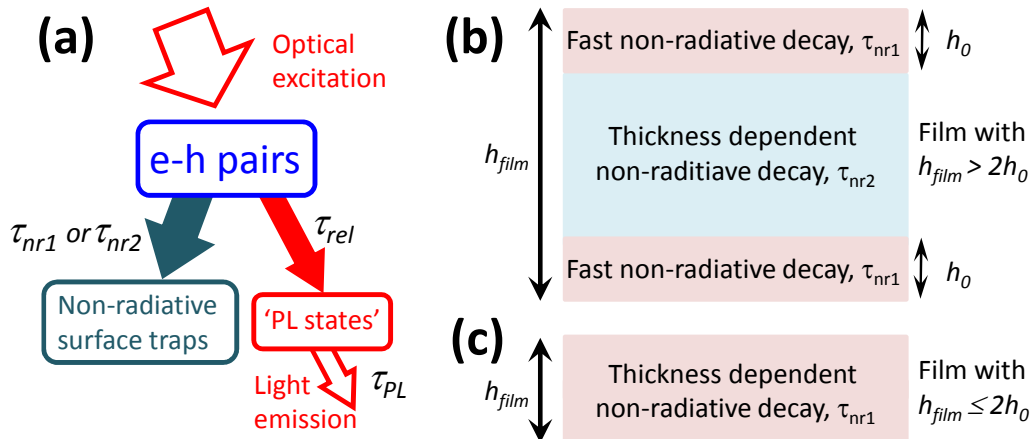
Fig. 3.7 Diagrams illustrating the theoretical model for the dependence of the cw PL intensity on the film thickness. (a) Processes included in the model (see text and supplementary information for more details): optical excitation of e-h pairs; relaxation into the non-radiative traps with a time τ_{nr1} or τ_{nr2} depending on the thickness of the film; relaxation with a time τ_{rel} into the light-emitting states denoted as 'PL states'; PL emission from these states with a time τ_{PL}. (b) and (c) shows two types of thin films with thicknesses above and below the critical thickness of $2h_0$. In (a) we show a relatively thick film with a thickness of $h_{film} > 2h_0$. This film has three regions: two regions of thickness h_0 near the film surfaces where fast carrier relaxation to surface traps occurs (shown in pink), and a 'normal' region of thickness $h_{film} - 2h_0$ in the middle of the film (blue) where non-radiative processes are weaker and occur through carrier escape into the surface regions. In (b) we show a thin film with $h_{film} \leq 2h_0$, where a region of one type only exists, where fast non-radiative carrier decay occurs.

3.3.5 Discussion

As detailed in Appendix A and observed in Fig.3.2(b) and Fig.3.3(b), we find that the proposed model provides a reasonable description of our data using four parameters (which are not completely independent as we find): the 'critical' thickness h_0, a parameter describing the amount of light absorbed by the film, and products $\tau_{rel}u_1$ and $\tau_{rel}u_2$. In particular the fitting functions that we produce capture the change in the 'slope' of the data observed at around 30 nm for GaSe and 40 nm for GaTe, which we interpret as the thickness of the film where $h_{film} \approx 2h_0$, i.e. the thickness of region (2) turns to zero, and non-radiative carrier escape changes its character.

However, we find that the accuracy of the fitting is not sufficient to extend our analysis beyond determination of the order of magnitude of the products $\tau_{rel}u_1$ and $\tau_{rel}u_2$. We find that $\tau_{rel}u_1$ and $\tau_{rel}u_2$ are of the order of 1000 nm and 100 nm, respectively, for both GaSe and GaTe. The solid line shown in Fig.3.2(b) for GaTe films is obtained for $\tau_{rel}u_1 = 3800$ nm and $\tau_{rel}u_2 = 200$ nm, whereas the fitting in Fig.3.3(b) for GaSe films is done for $\tau_{rel}u_1 = 2900$ nm and $\tau_{rel}u_2 = 150$ nm. We note that the description of GaSe PL is more satisfactory, possibly because in GaTe there is a contribution from free exciton PL, so additional non-radiative escape channels and relaxation processes need to be taken into account. For thicker GaTe films, much stronger PL than predicted by the model is observed, which probably signifies suppression of additional non-radiative escape that free excitons experience in relatively thin films. It is also notable that in GaTe the PL lifetime for localized states is shorter than in GaSe, which may be due to non-radiative escape. Such processes are not included in the model. Another reason could be deviation from the effectively 'ballistic' transport that we assume leads to the carrier escape into regions (1), and its replacement for the larger thicknesses with a slower 'diffusion' process leading to slower non-radiative escape.

Assuming that the measured PL rise-times of ≈ 20 ps are close to τ_{rel}, we can estimate characteristic non-radiative times τ_{nr1} and τ_{nr2} for several limiting cases. For example for GaSe we obtain the following values using $\tau_{rel}u_1$=1000 nm and $\tau_{rel}u_2$=100 nm: for h_{film}=10 nm τ_{nr1}=0.05 ps, for h_{film}=30 nm τ_{nr1}=0.15 ps, for h_{film}=100 nm τ_{nr2}=7 ps. For both h_{film} of 10 and 30 nm, the non-radiative decay occurs on a sub-picosecond time-scale. Here, the non-radiative escape is by a factor of the order of 100 faster than relaxation into the light emitting states, which is consistent with a low quantum yield of 10^{-3} reported previously for thin films of MoS_2[20]. For the middle region of a 100 nm film, the characteristic non-radiative escape time is comparable with the relaxation time into the states giving rise to PL, thus a much higher quantum

yield can be expected for films of this thickness.

We also note that in the case of region (2), u_2 should be of the order of a typical thermal velocity of an exciton, v_{th}. By using T=10 K and the exciton mass of 0.1 (or 0.2)[21] of the free electron mass we obtain $\tau_{rel}v_{th} \approx 1200$ (or 900) nm for $\tau_{rel} \approx$20 ps, very similar to the order of magnitude predicted by the model for the product $\tau_{rel}u_2$.

3.3.6   Conclusions

We have investigated thin films of GaTe and GaSe prepared by mechanical exfoliation from bulk crystals, deposited on SiO_2 substrates and capped with a thin layer of Si_3N_4. The study of optical properties of the thin films has been conducted by means of low-temperature cw and time-resolved micro-PL techniques. The most pronounced property observed is a significant reduction of cw PL intensity by up to 10^5 for thin films of thicknesses about 10 nm compared with the films of 150-200 nm. No measurable PL was observed in films thinner than 7 nm. Except for PL decrease, no other clear trends, including size-quantization effects and PL life-time modifications as a function of the film thickness were observed in cw and time-resolved PL. We argue that the reduction of quantum yield occurs due to the non-radiative processes associated with the surface states. The theoretical model that we develop differentiates between the fast non-radiative carrier escape to surface traps in the thin 15-20 nm layers near the film surface, and slower decay in the middle region of the film, where the carriers first diffuse to the surface layers and then decay. The model accounts for the change in the character of the PL decay for thin films with thicknesses less than 30-40 nm, where we expect only the fast direct relaxation to surface traps.

We do not refer in our model and interpretation to the direct-to-indirect bandgap transition found for thin InSe films in Ref.[8]. The observed strong PL decrease is not accompanied with any significant variation of the PL lifetime, which would most likely

accompany such a change in the band structure. This implies that the PL reduction in our case is not associated with this type of transition, and instead the reduction in the radiative recombination contribution is likely due to an increase in the non-radiative rate in thin films.

Strong non-radiative decay processes occur in the studied films despite complete encapsulation in Si_3N_4 and SiO_2 providing partial protection of the surface from chemical interactions with the ambient atmosphere. This emphasizes the need for development of novel surface passivation for III-VI films, possibly involving oxygen free substrates and encapsulation in additional layered materials such as boron nitride. Using this fabrication methods, the large family of III-VI materials may show weaker dependence of quantum yield on film thickness, which will allow them to play important role as building blocks in van der Waals heterostructures. It is likely that in the near future fabrication of such heterostructures will be carried out in oxygen and water free atmospheres and will include carefully designed passivating layers.

References

[1] M. O. D. Camara, A. Mauger, and I. Devos. Electronic structure of the layer compounds gase and inse in a tight-binding approach. *Phys. Rev. B*, 65:125206, Mar 2002. doi: 10.1103/PhysRevB.65.125206. URL `http://link.aps.org/doi/10.1103/PhysRevB.65.125206`.

[2] J. Z. Wan, J. L. Brebner, R. Leonelli, and J. T. Graham. Optical properties of excitons in gate. *Phys. Rev. B*, 46:1468–1471, 1992.

[3] F. Hulliger. *Structuml Chemistry of Layer TyPe Phases*. Reidel, Dordrecht, 1976.

[4] V. Capozzi. Direct and indirect excitonic emission in gase. *Phys. Rev. B*, 23: 836–840, 1981.

References

[5] V. Zólyomi, N. D. Drummond, and V. I. Fal'ko. Band structure and optical transitions in atomic layers of hexagonal gallium chalcogenides. *Phys. Rev. B*, 87: 195403, May 2013. doi: 10.1103/PhysRevB.87.195403. URL `http://link.aps.org/doi/10.1103/PhysRevB.87.195403`.

[6] Aishi Yamamoto, Atsushi Syouji, Takenari Goto, Erkin Kulatov, Kaoru Ohno, Yoshiyuki Kawazoe, Kazuhito Uchida, and Noboru Miura. Excitons and band structure of highly anisotropic gate single crystals. *Phys. Rev. B*, 64:035210, Jun 2001. doi: 10.1103/PhysRevB.64.035210. URL `http://link.aps.org/doi/10.1103/PhysRevB.64.035210`.

[7] V Grasso, G Mondio, M A Pirrone, and G Saitta. Modulation of optical constants of gate single crystals. *Journal of Physics C: Solid State Physics*, 8(1):80, 1975.

[8] G. W. Mudd, S. A. Svatek, T. Ren, A. Patanè, O. Makarovsky, L. Eaves, P. H. Beton, Z. D. Kovalyuk, G. V. Lashkarev, Z. R. Kudrynskyi, and A. I. Dmitriev. Tuning the bandgap of exfoliated inse nanosheets by quantum confinement. *Advanced Materials*, 25(40):5714–5718, 2013. ISSN 1521-4095. doi: 10.1002/adma.201302616. URL `http://dx.doi.org/10.1002/adma.201302616`.

[9] A. V. Kretinin, Y. Cao, J. S. Tu, G. L. Yu, R. Jalil, K. S. Novoselov, S. J. Haigh, A. Gholinia, A. Mishchenko, M. Lozada, T. Georgiou, C. R. Woods, F. Withers, P. Blake, G. Eda, A. Wirsig, C. Hucho, K. Watanabe, T. Taniguchi, A. K. Geim, and R. V. Gorbachev. Electronic properties of graphene encapsulated with different two-dimensional atomic crystals. *Nano Letters*, 14(6):3270–3276, 2014.

[10] N.N. Kolesnikov, E.B. Borisenko, D.N. Borisenko, and V.K. Gartman. Influence of growth conditions on microstructure and properties of gase crystals. *Journal of Crystal Growth*, 300(2):294 – 298, 2007.

[11] N.N. Kolesnikov, E.B. Borisenko, D.N. Borisenko, and S.I. Bozhko. Fractal structures of dendrites in gase crystals. *Journal of Crystal Growth*, 310(14):3287 – 3289, 2008.

[12] E.B. Borisenko, N.N. Kolesnikov, D.N. Borisenko, and S.I. Bozhko. Microhardness and structural defects of gase layered semiconductor. *Journal of Crystal Growth*, 316(1):20 – 24, 2011.

[13] N.N. Kolesnikov, E.B. Borisenko, D.N. Borisenko, and A.V. Timonina. Structure and microstructure of gate crystals grown by high-pressure vertical zone melting. *Journal of Crystal Growth*, 365(0):59 – 63, 2013.

[14] J. Camassel, P. Merle, H. Mathieu, and A. Gouskov. Near-band-edge optical properties of Gase$_x$te$_{1-x}$ mixed crystals. *Phys. Rev. B*, 19:1060–1068, 1979.

[15] A. Mercier, E. Mooser, and J. P. Voitchovsky. Resonant exciton in gase. *Phys. Rev. B*, 12:4307–4311, 1975.

[16] Philipp Tonndorf, Robert Schmidt, Robert Schneider, Johannes Kern, Michele Buscema, Gary A. Steele, Andres Castellanos-Gomez, Herre S. J. van der Zant, Steffen Michaelis de Vasconcellos, and Rudolf Bratschitsch. Single-photon emission from localized excitons in an atomically thin semiconductor. *Optica*, 2(4): 347–352, Apr 2015.

[17] S. Raymond, X. Guo, J. L. Merz, and S. Fafard. Excited-state radiative lifetimes in self-assembled quantum dots obtained from state-filling spectroscopy. *Phys. Rev. B*, 59:7624–7631, Mar 1999. doi: 10.1103/PhysRevB.59.7624. URL `http://link.aps.org/doi/10.1103/PhysRevB.59.7624`.

[18] R A Taylor and J F Rayn. Time-resolved exciton photoluminescence in gase and gate. *Journal of Physics C: Solid State Physics*, 20(36):6175, 1987.

References

[19] Raffaella Calarco, Michel Marso, Thomas Richter, Ali I. Aykanat, Ralph Meijers, André v.d. Hart, Toma Stoica, and Hans Lüth. Size-dependent photoconductivity in mbe grown gan nanowires. *Nano Letters*, 5(5):981–984, 2005.

[20] Kin Fai Mak, Changgu Lee, James Hone, Jie Shan, and Tony F Heinz. Atomically thin MoS2: a new direct-gap semiconductor. *Physical review letters*, 105(13): 136805, September 2010. ISSN 1079-7114. URL `http://www.ncbi.nlm.nih.gov/pubmed/21230799`.

[21] K. Watanabe, K. Uchida, and N. Miura. Magneto-optical effects observed for gase in megagauss magnetic fields. *Phys. Rev. B*, 68:155312, 2003.

Chapter 4

Photoluminescence and Raman investigation of stability of InSe and GaSe thin films

4.1   Introduction

An important issue for a variety of layered materials is stability of thin films in ambient conditions[3, 15–18]. This has particularly showed significance in recent studies of semiconducting black phosphorus [15], $MoTe_2$[19] and layered superconductors such as $NbSe_2$[20]. We show in this chapter that film stability issues have to be taken into account for III-VI films, in particular GaSe.

Both InSe and GaSe are layered crystals with strong covalent in-plane inter-atomic bonding and weaker van der Waals inter-plane bonding [21, 22] as discussed in 1.2.3. The single tetralayer having hexagonal in-plane structure consists of two Se atoms and two In or Ga atoms: Se-Ga-Ga-Se and Se-In-In-Se as shown in Fig.4.1(a) where the crystal structure of both materials is presented. InSe is a direct gap semiconducting material in its bulk form and has important applications in photo-voltaic devices

81

[23]. More recently it has been studied in its layered form [10, 24, 25], where tuning of its band-gap by varying the film thickness has been demonstrated making this material promising for van der Waals heterostructures such as light emitting diodes [6]. GaSe is well known for its nonlinear properties[26] and in the past few years thin films of this material were used for fabrication of photo-detectors [27] and in optical microcavities, where control of light-matter interaction was demonstrated for two-dimensional films[28].

In this chapter we investigate the stability of mechanically exfoliated thin films of InSe and GaSe with thicknesses ranging from 9 to 75 nm using micro-photoluminescence (μPL) and micro-Raman spectroscopy. We observe decrease of both the PL and Raman signal over a few days. Between the optical measurements the films are kept in air at room temperature. We interpret the decrease of both signals as gradual reduction of the effective film thickness due to interaction with oxygen and water in the atmosphere. This results in significant changes of the crystal properties, leading to modification and decrease of the Raman signal, and also weaker PL following occurrence of non-radiative centers at the layers adjacent to the films surfaces [11]. For GaSe, we estimate the rate of erosion of 0.14±0.05 nm/hour based on our previous detailed measurements of thickness-dependent PL, where we observed a strong reduction of PL intensity with the decreasing film thickness[11] (see chapter 3). Here we also demonstrate that encapsulation of the films in SiO_2 or Si_xN_y allows to overcome the problem of film degradation and prolongs the life-time of the films by two orders of magnitude up to several months.

4.2   Samples and experimental methods

Bulk GaSe studied in this chapter was grown by high-pressure vertical zone melting in graphite crucibles under Ar pressure from high-purity materials: Ga - 99.9999 % and

Se - 99.9995 % [29, 30]. InSe single crystals were grown by the Bridgman-Stockbarger method from a preliminarily synthesized ingot [31]. The conductivity of both materials is n-type, a typical observation in selenides.

InSe and GaSe films were exfoliated from bulk using a mechanical cleavage method discussed in detailed in section 2.1.1 and were deposited on thermally oxidized silicon substrates. This process generates a variety of films with different thicknesses. Encapsulated GaSe samples were fabricated with the same method and completed with additional deposition of a 10 nm capping layer of Si_xN_y or SiO_2 by plasma-enhanced chemical vapor deposition (PECVD). Atomic force microscopy (AFM) was used to measure the thickness of all studied films, including the capped structures. In Fig. 4.1(b) an AFM image of a multi-layer GaSe film is presented showing that the material thickness varies from ∼20 nm to ∼80 nm across the film (see the scale on the right). In 4.1(c) a group of InSe films with various thickness is presented in an optical microscope image. Here, film areas with different thicknesses are observed as different colors[32]. As evidenced from both images, by using a laser spot with a diameter of $\approx 1.5 - 2\mu$m, film areas with constant thickness can be reliably addressed in micro-PL and micro-Raman experiments.

Optical characterization of GaSe and InSe thin films was carried out using two different techniques: micro-PL (μPL) and micro-Raman spectroscopy. The μPL set-up, described in section 2.2.1, was equipped with a 532 nm continuous wave (cw) semiconductor diode laser for excitation of the sample placed in a flow cryostat at T=10K. The laser spot on the sample was $\approx 2\mu$m. PL signal was collected with an NA=0.55 objective and detected with a 0.5 m single spectrometer and a liquid nitrogen cooled charge coupled device. Micro-Raman was measured at room temperature using an InVia Renishaw System equipped with a 532 nm laser for excitation.

We study PL signal in GaSe and InSe films following their exposure to air starting
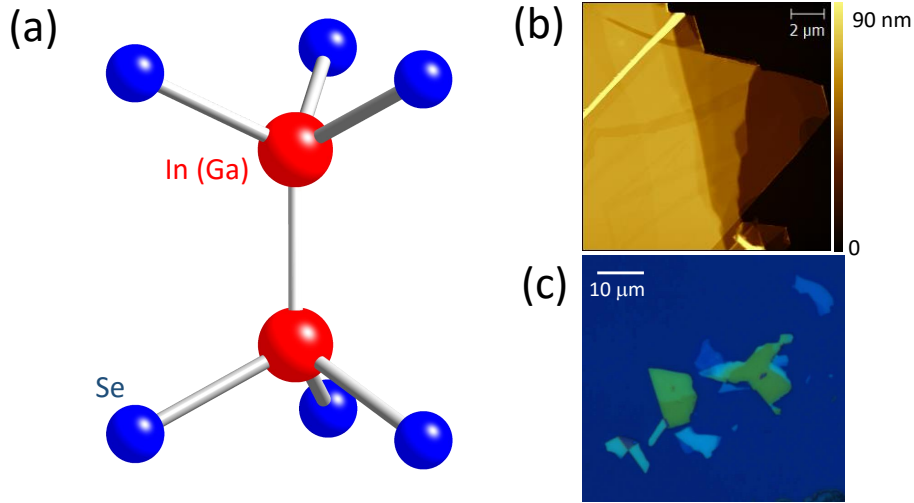
Fig. 4.1 (a) Crystal structure of InSe and GaSe. (b) AFM image of a multi-layer GaSe film. (c) Optical image of various isolated InSe thin films on SiO_2/Si substrates. Different colors in the image are associated with different film thicknesses.

from 1 hour after sample fabrication up to 100 hours. The time the sample is kept in the cryostat during the cool-down, the experiment itself and warm-up is not counted, as during this period the sample is kept in vacuum. After the measurement is complete and the sample returns to room temperature in the cryostat, it is taken out and stored in ambient conditions. The measurements in the cryostat were repeated after keeping the sample in air for 24 hours with a maximum total exposure of 100 hours. Raman experiments were carried out on the day of fabrication within a few hours after exfoliation and one week later.

4.3   Results

Fig.4.2 shows low-T μPL spectra of (a) a 31 nm InSe and (b) a 52 nm GaSe films measured with 1 mW laser power. The spectra are recorded from the same area of both films after different exposure to air. The InSe film shows a typical excitonic peak at ~1.3 eV in agreement with previous reports [24, 25, 33]. PL intensity exhibits a
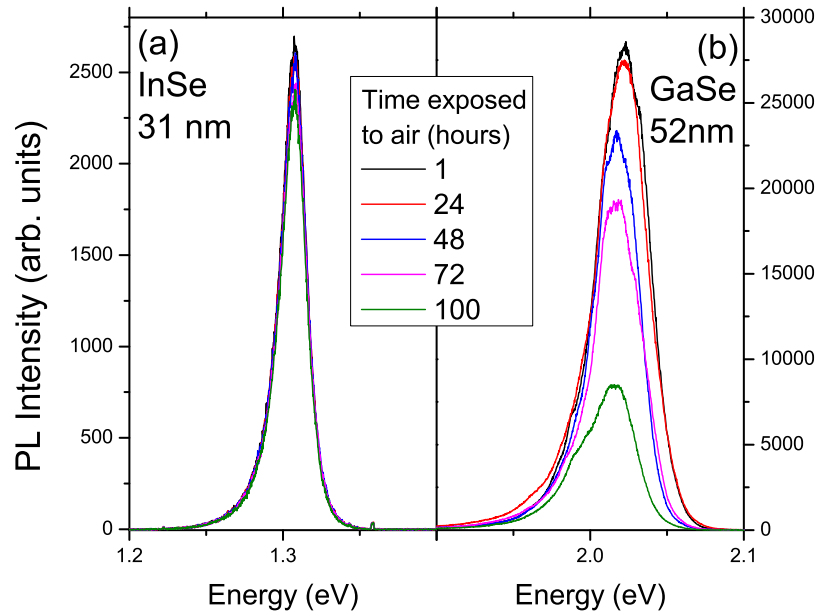
Fig. 4.2 Micro-photoluminescence spectra measured at low temperature of 10 K for (a) a 31 nm InSe film and (b) a 52 nm GaSe film after exposure to air from 1 to 100 hours.

negligible decrease from measurement to measurement that can be attributed to the re-alignment accuracy. For GaSe, a peak at ~ 2.02 eV is observed that we relate to impurity/defect states, which typically show bright PL in this material [11]. In the material studied in this work, the free exciton feature is only observed under pulsed excitation when the impurity states are saturated [11]. In contrast to the InSe film in Fig.4.2(a), for GaSe, PL signal changes its spectral shape and decreases significantly after the film has been exposed to air for several days.

Similar PL experiment was performed for 10 thin films of different thicknesses for each material. Figure 4.3 shows a comparison of integrated PL intensity of these InSe and GaSe thin films normalized by their intensity during the first measurement (1 hour after exfoliation). In order to reveal typical trends, we averaged over two groups of films showing similar behaviour: for group 1 we selected relatively thick films, 20-60 nm for InSe and 48-75 nm for GaSe; for group 2 we included thin films of 9-12 nm for

InSe and 10-25 nm for GaSe. For group 1 InSe films (blue squares) the PL intensity decreases by only about 12 % after 100 hours of exposure to air. For group 2 InSe films (blue dots) during the same period of time it decreases by a factor of two more, 25 %. For the GaSe films (red squares), we find that after just 24 hours exposed to air the intensity reduction is 15 % for group 1 thick films and 60 % for the thin films (red dots). Such rapid reduction of PL intensity is observed for both types of GaSe films, with the strongest effect for the case of the thin films where PL completely vanishes after 100 hours of exposure to air, whereas for the thick GaSe films, PL falls to 30 % of its initial intensity.

Similar behaviour of the signal intensities from the two materials is observed in Raman spectroscopy. In Fig. 4.4 Raman spectra of a 16 nm InSe and a 24 nm GaSe films are presented measured at room temperature. Typical modes reported previously for bulk GaSe and InSe [25, 34–37] are observed for these thin films. For InSe (top panel), the prominent peaks at 117.5, 179.5, 201.7 and 228.6 cm^{-1} correspond to the the vibrational modes A'$_1$, E", E'(TO) and A'$_1$ respectively. In the case of GaSe (bottom panel) the modes A'$_1$, E'(TO), E'(LO) and A'$_1$ at 135.6, 215.6, 308.7 cm^{-1} respectively, are observed. These Raman modes were clearly observed in both samples on the day when the samples were fabricated. The measurements were then repeated one week later, during which time both samples were stored at room temperature in air. As seen in the figure, the Raman intensity for InSe remains unchanged. In contrast, the Raman spectra for GaSe show significant variation with time: (i) the intensity drops by a factor of 10 and (ii) different relative strengths of the Raman modes are observed. These changes indicate significant modification of physical properties of GaSe films after exposure to air for 1 week.
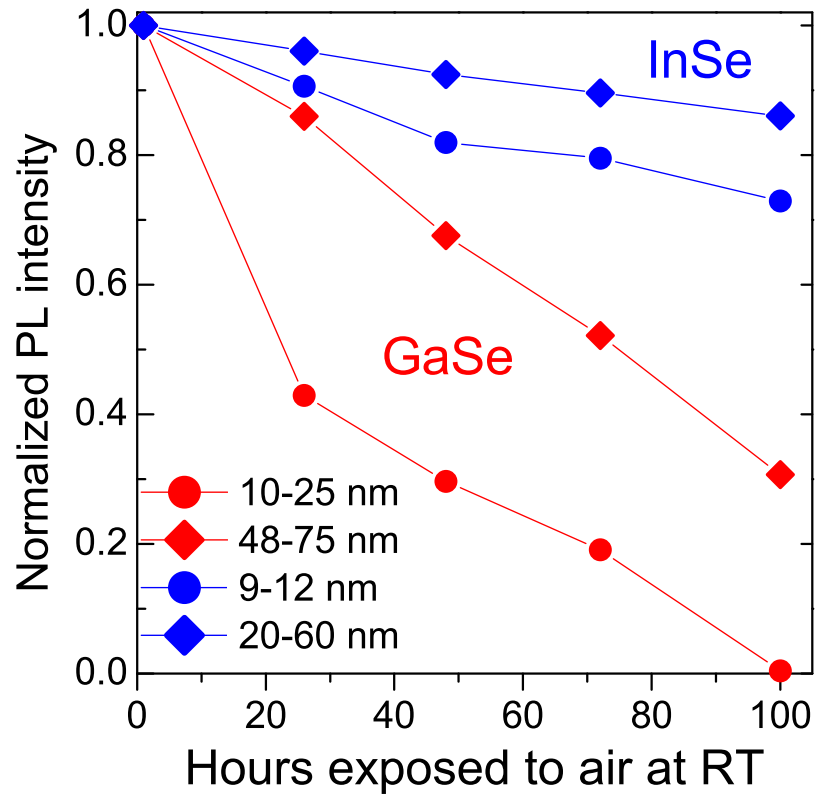
Fig. 4.3 (a) PL intensity measured at T=10 K as a function of time t_{exp} the InSe and GaSe thin films were exposed to air at room temperature. For InSe, the results are averaged and normalized by the intensity for t_{exp}=1 hour for two groups of five films with thicknesses in the range 9-12 nm (blue dots) and 20-60 nm (blue squares). For GaSe the same procedure is carried out for films with thicknesses in the range of 10-25 nm (red dots) and 48-75 nm (red squares).
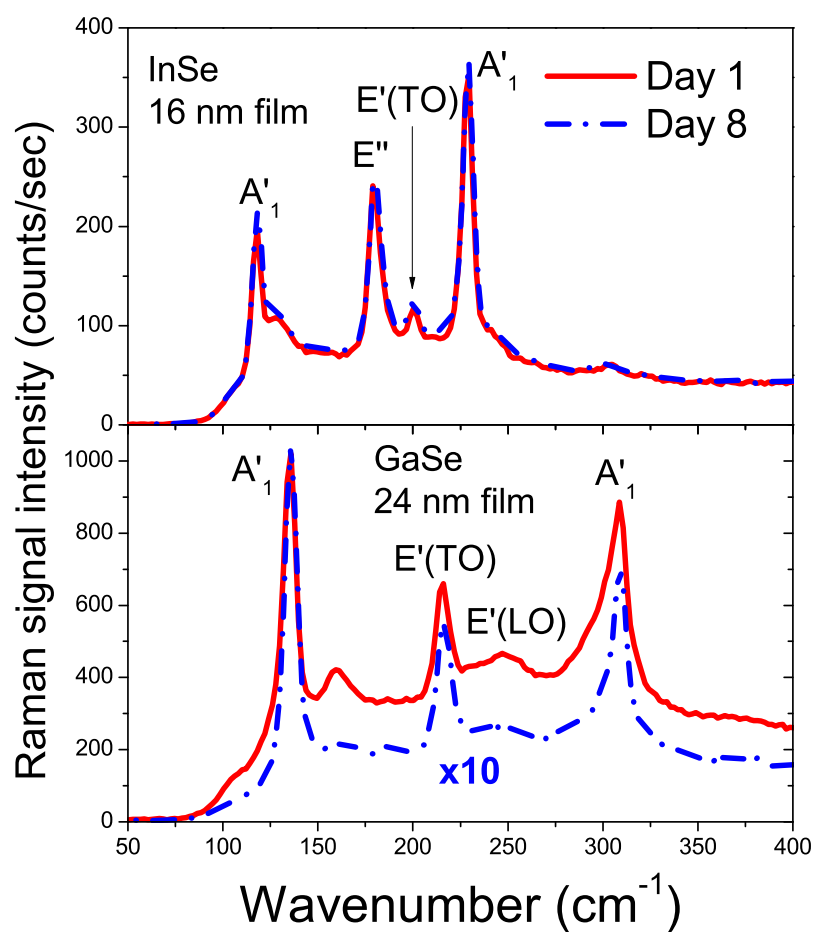
Fig. 4.4 Room temperature Raman spectra for a 16 nm InSe (top) and a 24 nm GaSe (bottom) film. The spectra were measured right after fabrication (solid line) and one week later (dashed line).

4.4   Discussion

The significant decrease of PL and Raman signals for GaSe can be attributed to the interaction of the film layers with water and oxygen in the atmosphere, similar to recent reports on black phosphorus [15, 16]. Such processes occur in the layers adjacent to the surface(s) of the film, leading to a significant change of the material properties. In a simplified way, this can be described as reduction of the effective film thickness with time when it is exposed to air, as it can be reasonably assumed that only the unaffected material would give rise to typical PL and Raman signals, whereas the eroded GaSe would show very low PL intensity (no PL emission at new wavelengths compared with the original samples were found).

Using our previous results for the detailed thickness-dependence of PL intensity in GaSe thin films presented in chapter 3, we can estimate the time-dependent changes of the effective film thickness in our present experiments. First, the PL dependence on exposure time for each film was analysed and effective thicknesses were obtained for each exposure time. This was carried out by matching the observed changes in PL intensities with those previously measured for a large number of films of different thicknesses, where we observed a strong reduction of PL intensity with the decreasing film thickness[11]. By performing this procedure, we deduced the erosion rate for each of the ten films, and finally obtained an average rate for all films of 0.14±0.05 nm/hour.

In contrast, for InSe we suggest that the crystal erosion occurs just for a small number of atomic layers at the surface and then possibly saturates causing insignificant impact on PL and Raman intensities.

The fact that GaSe thin films are sensitive to the environmental effects highlights that additional techniques are required in order to protect this material from interaction with atmosphere. Alternative methods such as fabrication of samples in an

inert atmosphere as well as encapsulation of the films with dielectric materials like boron nitride (hBN) [38], SiO_2 or Si_xN_y[39, 40] is required. For example, thin layers of black phosphorus exposed to air have been reported to degrade over a few minutes under environmental influences such as humidity, oxygen and exposure to visible light [15, 41]. However, such processes have been reported to be suppressed if films are exfoliated in an oxygen-free atmosphere [16, 38].

In this work, we fabricated a large number of GaSe films of different thicknesses capped with 10 nm Si_xN_y or SiO_2. The films were initially produced by mechanical exfoliation in air, after which PECVD deposition was carried out. In Fig.4.5 μPL spectra of a 32 nm GaSe film capped with Si_xN_y are presented. The spectrum shown in black was acquired one hour after fabrication, and the spectrum shown with a red curve was measured one month later. The difference between the intensity and lineshape of the two spectra is negligible, indicating significant slowing of the degradation processes. Similar degradation slow down was observed for films of any thickness for either Si_xN_y and SiO_2 capping.

4.5   Conclusions

Our results show that chemical interactions in the normal atmosphere lead to erosion of GaSe layers adjacent to the film surface with an average rate of 0.14±0.05 nm/hour, leading to significant decay over time of PL and Raman intensity. Such degradation is significantly weaker for InSe thin films. We relate this behaviour of GaSe with surface oxidation and interaction with water in the atmosphere. Our findings imply that InSe will be the least demanding III-VI layered material for the use in devices based on van der Waals heterostructures, as it requires minimum protection from atmosphere. GaSe thin films are in contrast relatively unstable under ambient conditions. However, the stability of these films can be significantly improved using encapsulation with
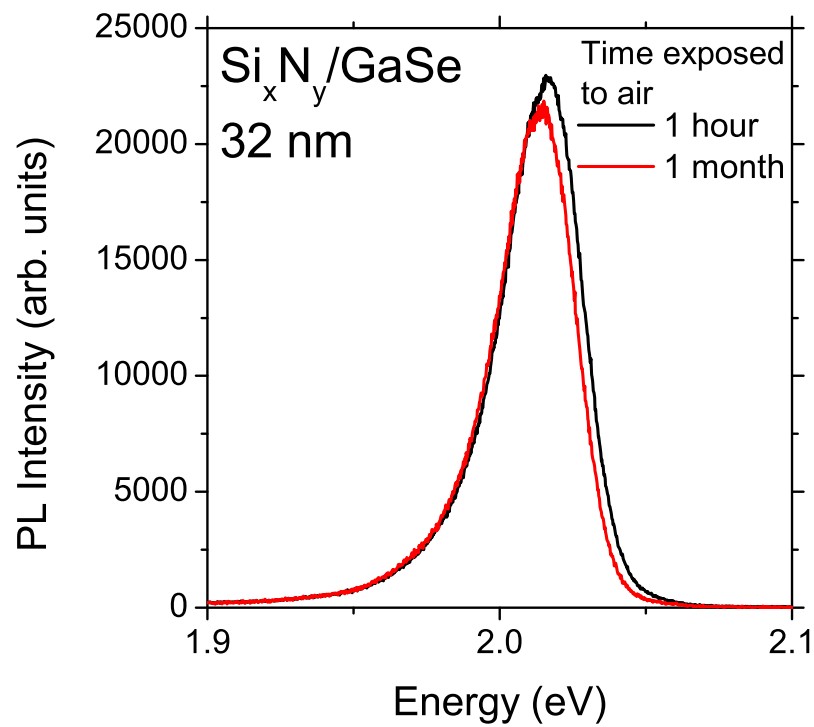
Fig. 4.5 PL spectra measured at T=10 K for a 32 nm thick GaSe film capped by a 10 nm PECVD layer of Si_xN_y. The film was measured one hour (black) and one month (red) after fabrication showing negligible signal decay.

dielectrics such as Si_xN_y or SiO_2, which slow down the degradation rate by more than two orders of magnitude.

References

[1] Kostya S Novoselov, Andre K Geim, SV Morozov, D Jiang, Y_ Zhang, SV Dubonos, IV Grigorieva, and AA Firsov. Electric field effect in atomically thin carbon films. *Science*, 306(5696):666–669, 2004.

[2] K. S. Novoselov, D. Jiang, F. Schedin, T. J. Booth, V. V. Khotkevich, S. V. Morozov, and A. K. Geim. Two-dimensional atomic crystals. *Proceedings of the National Academy of Sciences of the United States of America*, 102(30):10451–10453, 2005. doi: 10.1073/pnas.0502848102.

[3] Mingsheng Xu, Tao Liang, Minmin Shi, and Hongzheng Chen. Graphene-like two-dimensional materials. *Chemical Reviews*, 113(5):3766–3798, 2013. doi: 10.1021/cr300263a.

[4] Zhenxing Wang, Kai Xu, Yuanchang Li, Xueying Zhan, Muhammad Safdar, Qisheng Wang, Fengmei Wang, and Jun He. Role of ga vacancy on a multilayer gate phototransistor. *ACS Nano*, 8(5):4859–4865, 2014. doi: 10.1021/nn500782n.

[5] AK Geim and IV Grigorieva. Van der waals heterostructures. *Nature*, 499(7459):419–425, 2013.

[6] F Withers, O. Del Pozo-Zamudio, A Mishchenko, AP Rooney, A Gholinia, K Watanabe, T Taniguchi, SJ Haigh, AK Geim, and AI Tartakovskii. Light-emitting diodes by bandstructure engineering in van der waals heterostructures. *Nature Materials*, 14:301–306, 2015.

[7] Garry W. Mudd, Simon A. Svatek, Lee Hague, Oleg Makarovsky, Zakhar R. Kudrynskyi, Christopher J. Mellor, Peter H. Beton, Laurence Eaves, Kostya S. Novoselov, Zakhar D. Kovalyuk, Evgeny E. Vdovin, Alex J. Marsden, Neil R. Wilson, and Amalia Patanè. High broad-band photoresponsivity of mechanically formed inse–graphene van der waals heterostructures. *Advanced Materials*, pages n/a–n/a, 2015. ISSN 1521-4095.

[8] Andrea Splendiani, Liang Sun, Yuanbo Zhang, Tianshu Li, Jonghwan Kim, Chi-Yung Chim, Giulia Galli, and Feng Wang. Emerging photoluminescence in mono-layer mos2. *Nano Letters*, 10(4):1271–1275, 2010. doi: 10.1021/nl903868w. PMID: 20229981.

[9] Kin Fai Mak, Changgu Lee, James Hone, Jie Shan, and Tony F. Heinz. Atomically thin mos$_2$: A new direct-gap semiconductor. *Phys. Rev. Lett.*, 105:136805, Sep 2010.

[10] Garry W. Mudd, Simon A. Svatek, Tianhang Ren, Amalia Patanè, Oleg Makarovsky, Laurence Eaves, Peter H. Beton, Zakhar D. Kovalyuk, George V. Lashkarev, Zakhar R. Kudrynskyi, and Alexandr I. Dmitriev. Tuning the bandgap of exfoliated inse nanosheets by quantum confinement. *Advanced Materials*, 25 (40):5714–5718, 2013. ISSN 1521-4095. doi: 10.1002/adma.201302616. URL `http://dx.doi.org/10.1002/adma.201302616`.

[11] O. Del Pozo-Zamudio, S. Schwarz, M. Sich, I. A. Akimov, M. Bayer, R. C. Schofield, E. A. Chekhovich, B. J. Robinson, N. D. Kay, O. V. Kolosov, A. I. Dmitriev, G. V. Lashkarev, D. N. Borisenko, N. N. Kolesnikov, and A. I. Tartakovskii. Optical properties of two-dimensional gallium chalcogenide films. *arXiv*, 1501.02214, 2015. URL `http://arxiv.org/abs/1501.02214`.

[12] Fucai Liu, Hidekazu Shimotani, Hui Shang, Thangavel Kanagasekaran, Viktor

References

Zólyomi, Neil Drummond, Vladimir I. Fal'ko, and Katsumi Tanigaki. High-sensitivity photodetectors based on multilayer gate flakes. *ACS Nano*, 8(1):752–760, 2014. doi: 10.1021/nn4054039.

[13] Yanhao Tang, Wei Xie, Krishna C Mandal, John A McGuire, and Chih-Wei Lai. Linearly polarized remote-edge luminescence in gase nanoslabs. *arXiv preprint arXiv:1502.06070*, 2015.

[14] Dattatray J. Late, Bin Liu, Jiajun Luo, Aiming Yan, H. S. S. Ramakrishna Matte, Matthew Grayson, C. N. R. Rao, and Vinayak P. Dravid. Gas and gase ultra-thin layer transistors. *Advanced Materials*, 24(26):3549–3554, 2012. ISSN 1521-4095. doi: 10.1002/adma.201201361. URL http://dx.doi.org/10.1002/adma.201201361.

[15] Joshua O Island, Gary A Steele, Herre S J van der Zant, and Andres Castellanos-Gomez. Environmental instability of few-layer black phosphorus. *2D Materials*, 2(1):011002, 2015.

[16] Alexandre Favron, Etienne Gaufrès, Frédéric Fossard, Anne-Laurence Phaneuf-L'Heureux, Nathalie YW Tang, Pierre L Lévesque, Annick Loiseau, Richard Leonelli, Sébastien Francoeur, and Richard Martel. Photooxidation and quantum confinement effects in exfoliated black phosphorus. *Nature materials*, 2015.

[17] Elisabeth Bianco, Sheneve Butler, Shishi Jiang, Oscar D. Restrepo, Wolfgang Windl, and Joshua E. Goldberger. Stability and exfoliation of germanane: A germanium graphane analogue. *ACS Nano*, 7(5):4414–4421, 2013. doi: 10.1021/nn4009406.

[18] Sheneve Z. Butler, Shawna M. Hollen, Linyou Cao, Yi Cui, Jay A. Gupta, Humberto R. Gutiérrez, Tony F. Heinz, Seung Sae Hong, Jiaxing Huang,

Ariel F. Ismach, Ezekiel Johnston-Halperin, Masaru Kuno, Vladimir V. Plashnitsa, Richard D. Robinson, Rodney S. Ruoff, Sayeef Salahuddin, Jie Shan, Li Shi, Michael G. Spencer, Mauricio Terrones, Wolfgang Windl, and Joshua E. Goldberger. Progress, challenges, and opportunities in two-dimensional materials beyond graphene. *ACS Nano*, 7(4):2898–2926, 2013. doi: 10.1021/nn400280c.

[19] Bin Chen, Hasan Sahin, Aslihan Suslu, Laura Ding, Mariana I. Bertoni, F. M. Peeters, and Sefaattin Tongay. Environmental changes in mote2 excitonic dynamics by defects-activated molecular interaction. *ACS Nano*, 9(5):5326–5332, 2015. doi: 10.1021/acsnano.5b00985. PMID: 25868985.

[20] Mohammed S El-Bana, Daniel Wolverson, Saverio Russo, Geetha Balakrishnan, Don Mck Paul, and Simon J Bending. Superconductivity in two-dimensional nbse 2 field effect transistors. *Superconductor Science and Technology*, 26(12):125020, 2013. URL `http://stacks.iop.org/0953-2048/26/i=12/a=125020`.

[21] M. O. D. Camara, A. Mauger, and I. Devos. Electronic structure of the layer compounds gase and inse in a tight-binding approach. *Phys. Rev. B*, 65:125206, Mar 2002. doi: 10.1103/PhysRevB.65.125206. URL `http://link.aps.org/doi/10.1103/PhysRevB.65.125206`.

[22] V. Capozzi. Direct and indirect excitonic emission in gase. *Phys. Rev. B*, 23: 836–840, Jan 1981. doi: 10.1103/PhysRevB.23.836. URL `http://link.aps.org/doi/10.1103/PhysRevB.23.836`.

[23] Mohammad Afzaal and Paul O'Brien. Recent developments in ii-vi and iii-vi semiconductors and their applications in solar cells. *J. Mater. Chem.*, 16:1597–1602, 2006. doi: 10.1039/B512182E. URL `http://dx.doi.org/10.1039/B512182E`.

[24] G. W. Mudd, A. Patanè, Z. R. Kudrynskyi, M. W. Fay, O. Makarovsky, L. Eaves,

References

Z. D. Kovalyuk, V. Zólyomi, and V. Falko. Quantum confined acceptors and donors in inse nanosheets. *Applied Physics Letters*, 105(22):221909, 2014. doi: http://dx.doi.org/10.1063/1.4903738. URL `http://scitation.aip.org/content/aip/journal/apl/105/22/10.1063/1.4903738`.

[25] JuanF. Sánchez-Royo, Guillermo Muñoz Matutano, Mauro Brotons-Gisbert, JuanP. Martínez-Pastor, Alfredo Segura, Andrés Cantarero, Rafael Mata, Josep Canet-Ferrer, Gerard Tobias, Enric Canadell, Jose Marqués-Hueso, and BrianD. Gerardot. Electronic structure, optical properties, and lattice dynamics in atomically thin indium selenide flakes. *Nano Research*, 7(10):1556–1568, 2014. ISSN 1998-0124. doi: 10.1007/s12274-014-0516-x. URL `http://dx.doi.org/10.1007/s12274-014-0516-x`.

[26] J. M. Auerhammer and E. R. Eliel. Frequency doubling of mid-infrared radiation in gallium selenide. *Opt. Lett.*, 21(11):773–775, Jun 1996. doi: 10.1364/OL.21.000773.

[27] PingAn Hu, Zhenzhong Wen, Lifeng Wang, Pingheng Tan, and Kai Xiao. Synthesis of few-layer gase nanosheets for high performance photodetectors. *ACS Nano*, 6(7):5988–5994, 2012. doi: 10.1021/nn300889c.

[28] S. Schwarz, S. Dufferwiel, P. M. Walker, F. Withers, A. A. P. Trichet, M. Sich, F. Li, E. A. Chekhovich, D. N. Borisenko, N. N. Kolesnikov, K. S. Novoselov, M. S. Skolnick, J. M. Smith, D. N. Krizhanovskii, and A. I. Tartakovskii. Two-dimensional metal–chalcogenide films in tunable optical microcavities. *Nano Letters*, 14(12):7003–7008, 2014. doi: 10.1021/nl503312x.

[29] N.N. Kolesnikov, E.B. Borisenko, D.N. Borisenko, and V.K. Gartman. Influence of growth conditions on microstructure and properties of gase crystals. *Journal of Crystal Growth*, 300(2):294 – 298, 2007. ISSN 0022-0248. doi: http:

//dx.doi.org/10.1016/j.jcrysgro.2007.01.001. URL `http://www.sciencedirect.`
`com/science/article/pii/S0022024807000425`.

[30] E.B. Borisenko, N.N. Kolesnikov, D.N. Borisenko, and S.I. Bozhko. Microhard-
ness and structural defects of gase layered semiconductor. *Journal of Crystal
Growth*, 316(1):20 – 24, 2011. ISSN 0022-0248. doi: http://dx.doi.org/10.1016/
j.jcrysgro.2010.12.021. URL `http://www.sciencedirect.com/science/article/`
`pii/S0022024810011826`.

[31] A.I. Dmitriev, V.V. Vishnjak, G.V. Lashkarev, V.L. Karbovskyi, Z.D. Kovaljuk,
and A.P. Bahtinov. Investigation of the morphology of the van der waals surface
of the inse single crystal. *Physics of the Solid State*, 53(3):622–633, 2011. ISSN
1063-7834. doi: 10.1134/S1063783411030085. URL `http://dx.doi.org/10.1134/`
`S1063783411030085`.

[32] A Castellanos-Gomez, N Agraït, and G Rubio-Bollinger. Optical identification of
atomically thin dichalcogenide crystals. *Applied Physics Letters*, 96(21):213116,
2010. doi: http://dx.doi.org/10.1063/1.3442495. URL `http://scitation.aip.`
`org/content/aip/journal/apl/96/21/10.1063/1.3442495`.

[33] V. Zólyomi, N. D. Drummond, and V. I. Fal'ko. Electrons and phonons in single
layers of hexagonal indium chalcogenides from *ab initio* calculations. *Phys. Rev.
B*, 89:205416, May 2014. doi: 10.1103/PhysRevB.89.205416. URL `http://link.`
`aps.org/doi/10.1103/PhysRevB.89.205416`.

[34] K. Allakhverdiev, T. Baykara, Ş. Ellialtioğlu, F. Hashimzade, D. Huseinova,
K. Kawamura, A.A. Kaya, A.M. Kulibekov (Gulubayov), and S. Onari.
Lattice vibrations of pure and doped gase. *Materials Research Bulletin*,
41(4):751 – 763, 2006. ISSN 0025-5408. doi: http://dx.doi.org/10.

1016/j.materresbull.2005.10.015. URL `http://www.sciencedirect.com/science/article/pii/S0025540805003855`.

[35] Raul D. Rodriguez, Susanne Mueller, Evgeniya Sheremet, Dietrich R. T. Zahn, Alexander Villabona, Santos A. Lopez-Rivera, Philipp Tonndorf, Steffen Michaelis de Vasconcellos, and Rudolf Bratschitsch. Selective raman modes and strong photoluminescence of gallium selenide flakes on sp2 carbon. *Journal of Vacuum Science & Technology B*, 32(4):04, 2014.

[36] N. Kuroda and Y. Nishina. Resonant raman scattering at higher {M0} exciton edge in layer compound inse. *Solid State Communications*, 28(6):439 – 443, 1978. ISSN 0038-1098. doi: http://dx.doi.org/10.1016/0038-1098(78)90834-7. URL `http://www.sciencedirect.com/science/article/pii/0038109878908347`.

[37] N. Kuroda and Y. Nishina. Resonance raman scattering study on exciton and polaron anisotropies in inse. *Solid State Communications*, 34(6):481 – 484, 1980. ISSN 0038-1098. doi: http://dx.doi.org/10.1016/0038-1098(80)90656-0. URL `http://www.sciencedirect.com/science/article/pii/0038109880906560`.

[38] Y. Cao, A. Mishchenko, G. L. Yu, K. Khestanova, A. Rooney, E. Prestat, A. V. Kretinin, P. Blake, M. B. Shalom, G. Balakrishnan, I. V. Grigorieva, K. S. Novoselov, B. A. Piot, M. Potemski, K. Watanabe, T. Taniguchi, S. J. Haigh, A. K. Geim, and R. V. Gorbachev. Quality heterostructures from two dimensional crystals unstable in air by their assembly in inert atmosphere. *arXiv*, 1502.03755, 2015. ISSN 2. URL `http://arxiv.org/abs/1502.03755`.

[39] D. Sercombe, S. Schwarz, O. Del Pozo-Zamudio, F. Liu, B. J. Robinson, E. A. Chekhovich, I. I. Tartakovskii, O. Kolosov, and A. I. Tartakovskii. Optical investigation of the natural electron doping in thin mos2 films deposited on di-

electric substrates. *Scientific Reports*, 3:3489, 2013. ISSN 2045-2322. doi: 10.1038/srep03489. URL `http://www.nature.com/srep/2013/131212/srep03489`.

[40] A. V. Kretinin, Y. Cao, J. S. Tu, G. L. Yu, R. Jalil, K. S. Novoselov, S. J. Haigh, A. Gholinia, A. Mishchenko, M. Lozada, T. Georgiou, C. R. Woods, F. Withers, P. Blake, G. Eda, A. Wirsig, C. Hucho, K. Watanabe, T. Taniguchi, A. K. Geim, and R. V. Gorbachev. Electronic properties of graphene encapsulated with different two-dimensional atomic crystals. *Nano Letters*, 14(6):3270–3276, 2014. doi: 10.1021/nl5006542.

[41] Andres Castellanos-Gomez, Leonardo Vicarelli, Elsa Prada, Joshua O Island, K L Narasimha-Acharya, Sofya I Blanter, Dirk J Groenendijk, Michele Buscema, Gary A Steele, J V Alvarez, Henny W Zandbergen, J J Palacios, and Herre S J van der Zant. Isolation and characterization of few-layer black phosphorus. *2D Materials*, 1(2):025001, 2014. URL `http://stacks.iop.org/2053-1583/1/i=2/a=025001`.

Chapter 5

Light-emitting diodes by band-structure engineering in van der Waals heterostructures

5.1 Introduction

The advent of graphene and related 2D materials [1, 2] has recently led to a new technology: heterostructures based on these atomically thin crystals [3]. As described in section 1.2.5, many different devices and applications have been developed. In this chapter we take the complexity and functionality of such van der Waals heterostructures to the next level by introducing quantum wells (QWs) engineered with one atomic plane precision. We describe light emitting diodes (LEDs) made by stacking up metallic graphene, insulating BN and various semiconducting monolayers into complex but carefully designed sequences. Our first devices already exhibit extrinsic quantum efficiency of nearly 10% and the emission can be tuned over a wide range of wavelengths by appropriately choosing and combing 2D semiconductors (monolayers of TMDCs).

Light-emitting diodes by band-structure engineering in van der Waals heterostructures

Two-dimensional materials, that started with graphene, now include a large variety of compounds[4]. However the real diversity can be achieved when combining these materials to make heterostructures. If we take into account their different band-structures, distinct potential landscapes for electrons to live in can be created.

Such band-structure engineering has previously been exploited to create LEDs and lasers based on semiconductor heterostructures grown by molecular beam epitaxy[5]. Here we demonstrate that using graphene as a transparent conductive coating, hexagonal boron nitride (hBN) as tunnel barriers and different TMDCs[6] as the materials for QWs, we can create efficient LEDs. In our devices, electrons and holes are injected to a layer of TMDC from the two graphene electrodes. Because of the long lifetime of the quasiparticles in the QWs (determined by the height and thickness of the neighbouring hBN barriers), electrons and holes recombine, emitting a photon. The emission wavelength can be fine-tuned by the appropriate selection of TMDC and quantum efficiency (QE) can be enhanced by using multiple QWs (MQWs).

We chose TMDC because of wide choice of such materials and the fact that monolayers of many TMDC are direct band gap semiconductors[7–11]. Until this work, electroluminescence (EL) in TMDC devices has been reported only for lateral monolayer devices and attributed to thermally assisted processes arising from impact ionization across a Schottky barrier[12] and formation of p-n junctions[11, 13, 14]. The use of vertical heterostructures allows us to improve the performance of LED's in many respects: reduced contact resistance, higher current densities allowing brighter LEDs, luminescence from the whole device area (Figs. 5.4A-B) and wider choice of TMDC and their combinations allowed in designing such heterostructures. The same technology can be extended to create other QW-based devices such as indirect excitonic devices[15], LEDs based on several different QWs and lasers.

5.2   Samples and experimental methods

Figure 5.1 shows schematically the architecture of (a) single quantum well (SQW) and (b) MQW structures. In the SQW a TMDC single layer is sandwiched by hBN, graphene (for electrical injection) and again hBN for encapsulation. In the case of MQW the two or more TMDC layer are separated by hBN (for tunnel barriers) and then the structure is completed with the sandwich as in SQW. A peel/lift van der Waals technique[16] was used to produce the devices (see section 2.1.2 for further details on device fabrication). Electrical contacts connected to the top and bottom graphene electrodes are patterned using electron-beam lithography followed by evaporation of 5 nm Cr/60 nm Au. Different QW structures comprising single and multiple layers of TMDC flakes from three different materials, MoS_2, WS_2 and WSe_2 were produced by Sheffield's collaborator Dr. F. Withers.

Cross sectional bright field scanning transmission electron microscope (STEM) images of the SQW and MQW devices, provided by Dr. S. Haigh (Manchester), demonstrate that the heterostructures are atomically flat and free from interlayer contamination [17]; Fig. 5.1b,d. The large atomic numbers for TMDC allow the semi-conductor crystals to be clearly identified due to strong electron-beam scattering (dark contrast observed in Fig. 5.1b-d). Other layers were identified by energy dispersive X-ray spectroscopy. The large intensity variation partially obscures the lattice contrast between adjacent layers but, despite this, the hBN lattice fringes can clearly be seen in Figs. 5.1b-d. The different contrast of the four MoS2 monolayers in the MQW of Fig. 5.1d is attributed to their different crystallographic orientations, (confirmed by rotating the sample around the heterostructure's vertical direction which changes the relative intensity of different layers).

Optical characterization of the devices was carried out using micro-photoluminescence and electroluminescence spectroscopy within a helium flow cryostat at 6 K. The setup

103

is described in sections 2.2.1 and 2.2.1. A 532 nm laser was used for PL measurements, focused to a spot size of ∼1-2 μm using a 50x objective. EL was produced with a voltage source (Keithley 2400) with different bias voltages depending on device characteristics.

5.3   Results

In fig. 5.2(A-C) the band diagrams of a SWQ based on MoS_2 (that can be extended to any TMDC) for the case of zero applied bias (A), intermediate bias V_b (B) and high bias (C) are shown. It shows how electrons and holes tunnel through the hBN barrier when V_b reach the onset bias. When this happens, excitons are created and able to recombine to create photons. Here the charge neutrality point of graphene lies 1.5 eV above the valence band of h-BN and 0.5 eV below the conduction bands of MoS_2 as found earlier in tunnelling experiments [18]. The devices often demonstrate some small asymmetry with respect to the reversal of V_b, which we associate with unintentional chemical doping being slightly different for Gr_B and Gr_T. In nearly all devices, EL could be observed both for positive and negative V_b, though with somewhat different intensity.

To gain insight into the operation of the SQW devices current-voltage characteristics and photoluminescence (PL) and EL spectra were measured. Three different SQW LEDs were characterised using MoS_2, WS_2 and WSe_2. The concerned heterostructures are shown schematically in Fig. 5.1(a).

5.3.1 MoS_2 single quantum well LED

In Fig. 5.3(a-c) the spectral characterisation of the MoS_2 SQW device (named SL MoS_2-1) at T=6 K is presented. Fig.5.3(a) shows the PL bias (V_b) dependence from
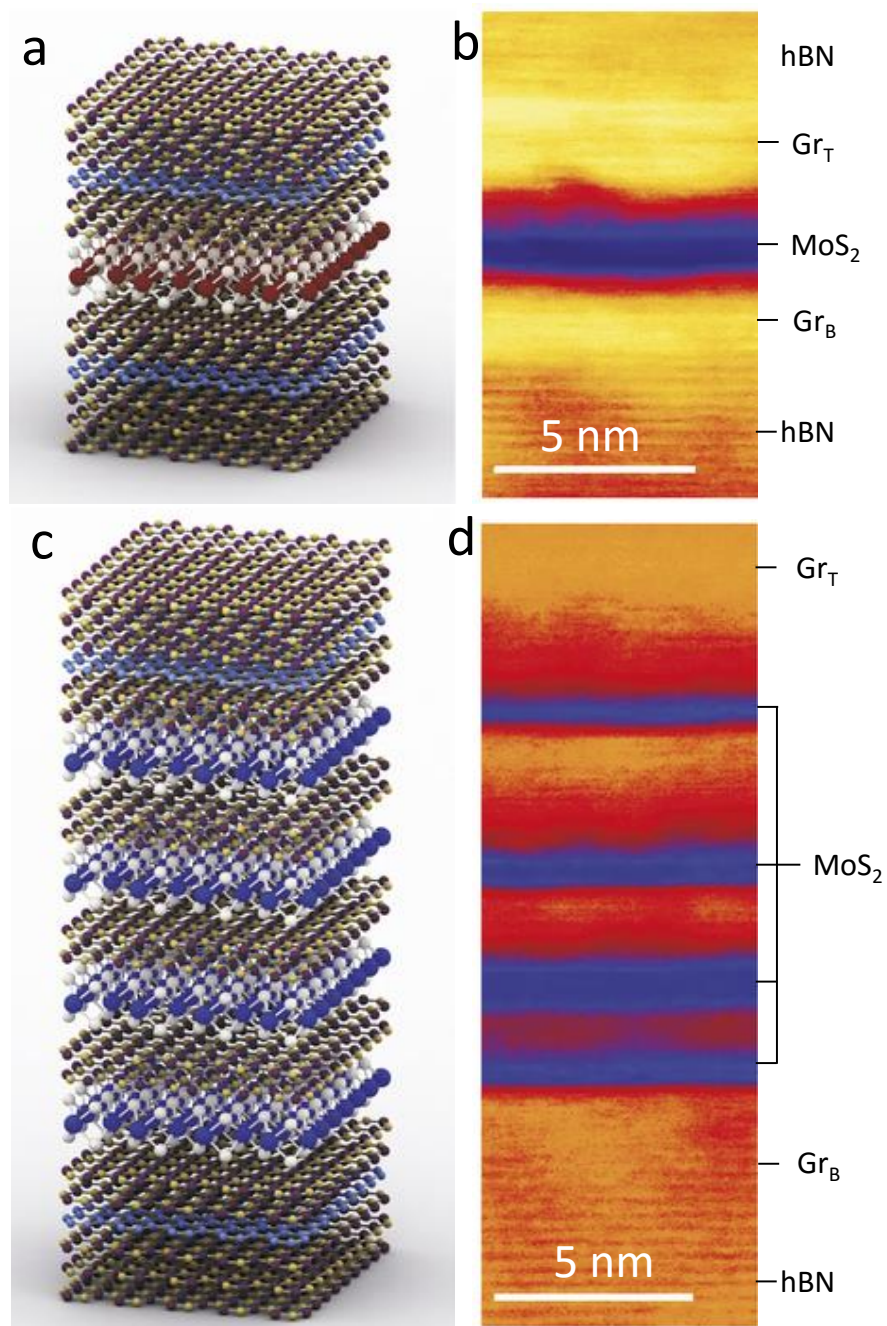
Fig. 5.1 Schematics of the (a) SQW heterostructure hBN/Gr$_B$/2hBN/MoS$_2$/2hBN/Gr$_T$/hBN. (b) Cross-sectional bright field STEM image of the type of heterostructures presented in (a). (c) MQW heterostructure hBN/Gr$_B$/2hBN/MoS$_2$/2hBN/MoS$_2$/2hBN/MoS$_2$/2hBN/MoS$_2$/Gr$_T$/hBN. (d) Cross-sectional bright field STEM image of the type of heterostructures presented in (c).
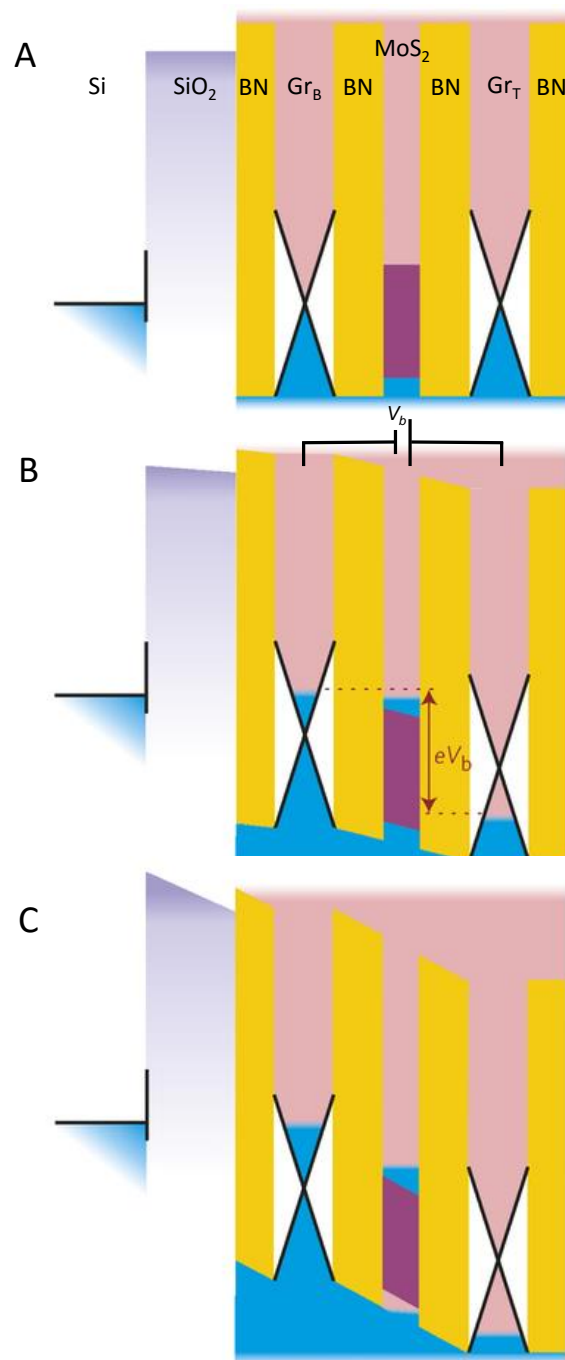
Fig. 5.2 Band diagrams for the case of zero applied bias (A), intermediate applied bias V_b (B) and high bias (C) for the heterostructure presented in Fig. 5.1(a), electrons and holes recombine to produce EL with energy $\hbar\omega_{EL}$.
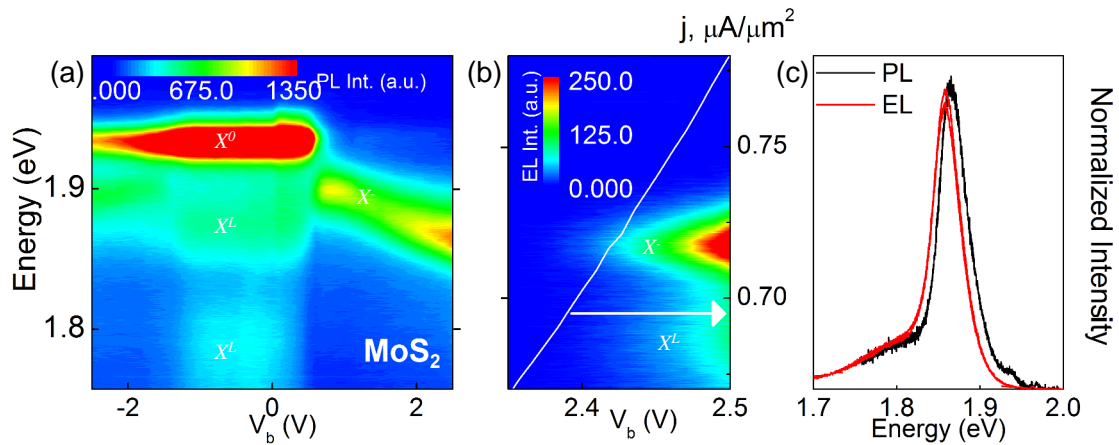
Fig. 5.3 Optical and transport characterization of a MoS_2 SQW device (SL MoS_2-1). (a) PL bias dependence of MoS_2 LED. (b) EL bias dependence of MoS_2 LED. (c) Comparison of EL and PL spectra for MoS_2 LED at 2.3 V.

-2.2 to 2.2 V. At low V_b, the PL is dominated by the peak at 1.93 eV, which we interpret as the neutral A exciton, X^0 [8]. We attribute the two weaker and broader peaks at 1.87 and 1.79 eV to bound excitons, X^L [19, 20] . For -0.8 V $<V_b<$ 0.6 V no significant change occurs in the spectrum. However, at V_b=0.65 V, the PL spectrum changes abruptly with another peak emerging at a lower energy of 1.90 eV. We explain this transition as being due to the fact that at this voltage the Fermi level in Gr_B rises above the conduction band in MoS_2, allowing injection of electrons into the QW (Fig. 5.3(c)). This leads not only to an increase in tunnelling conductivity but, also, to accumulation of electrons in MoS_2 and formation of negatively charged excitons, X^- [13]. The X^- peak is positioned at a lower energy compared to the X^0 peak due to the binding energy, E_B, of X^-. In the case of MoS_2 it is estimated as ~36 meV near the onset of X^-. As the bias is increased, the energy of the X^- shifts to lower values which we attribute to the quantum confined Stark effect or increase in the Fermi energy in MoS_2[8].

In contrast to PL, EL starts only at V_b above a certain threshold (Fig. 5.3b). Such

Light-emitting diodes by band-structure engineering in van der Waals heterostructures
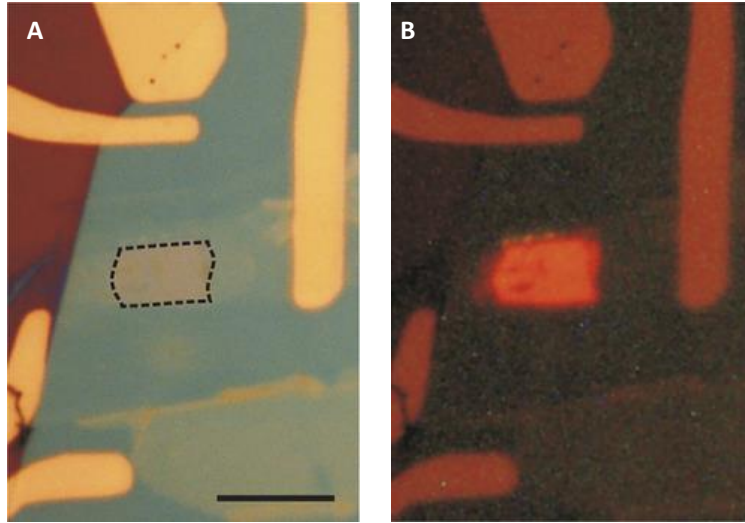

Fig. 5.4 Optical image of a SQW device based on MoS_2 (SL MoS_2-1). (A) Device with no voltage applied, the dashed line outlines the heterostructure are. Scale bar, 10 μm. (B) The same device emitting light with a voltage of 2.5 V.

behaviour is associated with the Fermi level of Gr_T being brought below the edge of the valence band so that holes can be injected to MoS_2 from Gr_T (in addition to electrons already injected from Gr_B) as sketched in Fig. 5.2C. This creates conditions for exciton formation inside the QW and their radiative recombination.

We find that the EL frequency is close to that of PL at V_b 2.4 V (Figs. 5.3a-c), which allows us to attribute the EL to radiative recombination of X^-. A comparison of both EL and PL spectra is shown in fig. 5.3c with V_b=2.4 V. A real image of this device is presented in fig. 5.4, (A) shows the device with no voltage applied. Here dashed line highlight the overlaping area of the layers. In (B) this area emits red light due to a voltage V_b=2.5 V applied through the graphene contacts. The black scale bar corresponds to 10 μm.
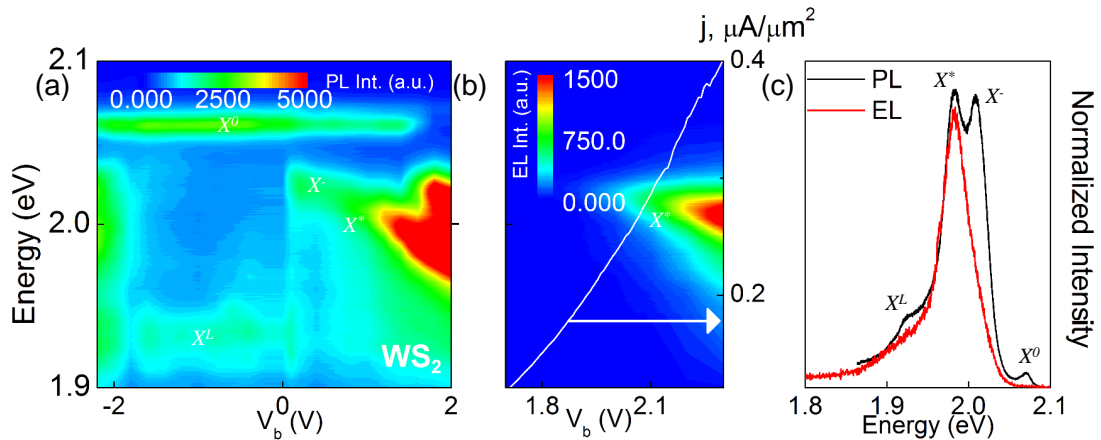
Fig. 5.5 Optical and transport characterization of a WS$_2$ SQW device (SL WS$_2$-1). (a) PL bias dependence of WS$_2$ LED. (b) EL bias dependence of WS$_2$ LED. (c) Comparison of EL and PL spectra for WS$_2$ LED at 2 V.

5.3.2 WS$_2$ single quantum well LED

Similar behaviour is observed for a WS$_2$ QW device (SL WS$_2$-1), see Figs. 5.5a-c. PL spectra show a neutral exciton X^0 peak [21] at 2.06 eV from -2.1 to 1.8 V (fig. 5.5a). At positive bias V$_b$ a trion peak X^- is tuned from 2.01 eV to lower energies down to 1.95 eV. At negative bias an additional peak at lower energy (1.91 eV) is observed, this emission is associated with the bound excitons [19]. EL arises from $\sim$1.9 V from X^*, as can be seen in fig. 5.5b. White line in this figure shows the current density as a function of V$_b$. The difference in EL and PL spectra is notable in this material at 2V (fig 5.5c), showing two pronounced peaks in PL and only one peak and a shoulder at lower energy beyond X^0 and X^- peaks in EL, the origin of other spectral lines cannot be established at present with certainty. It is likely that X^* peak correspond to emission from impurity-bound excitons, similarly to X^L.

5.3.3 Multiple quantum well LED devices

As described above, MQW devices were fabricated. The same optical characterisation as for SQW devices was carried out.

Figs. 5.6 and 5.7 show results for two such MQW structures with three (3MQW MoS$_2$-1) and four MoS2 QWs (4MQW MoS$_2$-1), respectively. The current increases with V$_b$ in a step-like manner, which is attributed to sequential switching of tunnelling through individual MoS$_2$ QW (see Figs. 5.6 and 5.7).

In the three-QW device PL is qualitatively similar to that of SQW devices (Fig. 5.6a) but the X_0 peak is replaced with X^- peak at a V$_b$=-0.4 V. The X^0 peak reappears again at V$_b$>1.2V. This can be explained by charge redistribution between different QWs. The EL first becomes observable at V$_b$>3.9 V and j of 1.8 nA/μm^2; Fig. 5.6d. This current density is nearly 2 orders of magnitude smaller than the threshold current required to see EL in similar SQWS. Figure 5.6e shows EL and PL spectra where it can be seen that both X^0 (width 24 meV) and X^- (width 78 meV) peaks appear in EL at energies of 1.94 and 1.86 eV, respectively, similar to their positions in SQWs. The width of the X^- exciton line, however, has been significantly broadened compared to the SQWs.

For the four-QW device, PL spectra are dominated by X_0 and X^- (Fig. 5.7b). A broad peak at 1.6 eV appears at negative bias from 2.5 V originating from the localized excitons X^L. EL is seen from 0.9 nA/μm^2 (blue curve in Fig. 5.7d), less than in the 3 QWs device with a photon energy of 1.8 eV originated from only X^-. Two more individual spectra with higher injection currents are shown in Fig. 5.7d in green and red. Comparison of both EL and PL at 7 V is observed in Fig. 5.7e.

The described technology of making designer MQWs offers the possibility of combining various semiconductor TMDCs in one device. Figs. 5.8(a-c) describe an LED made from WSe$_2$ and MoS$_2$ QWs: Si/SiO$_2$/hBN/Gr$_B$/3hBN/WSe$_2$/3hBN/MoS$_2$/3hBN/Gr$_T$/hBN
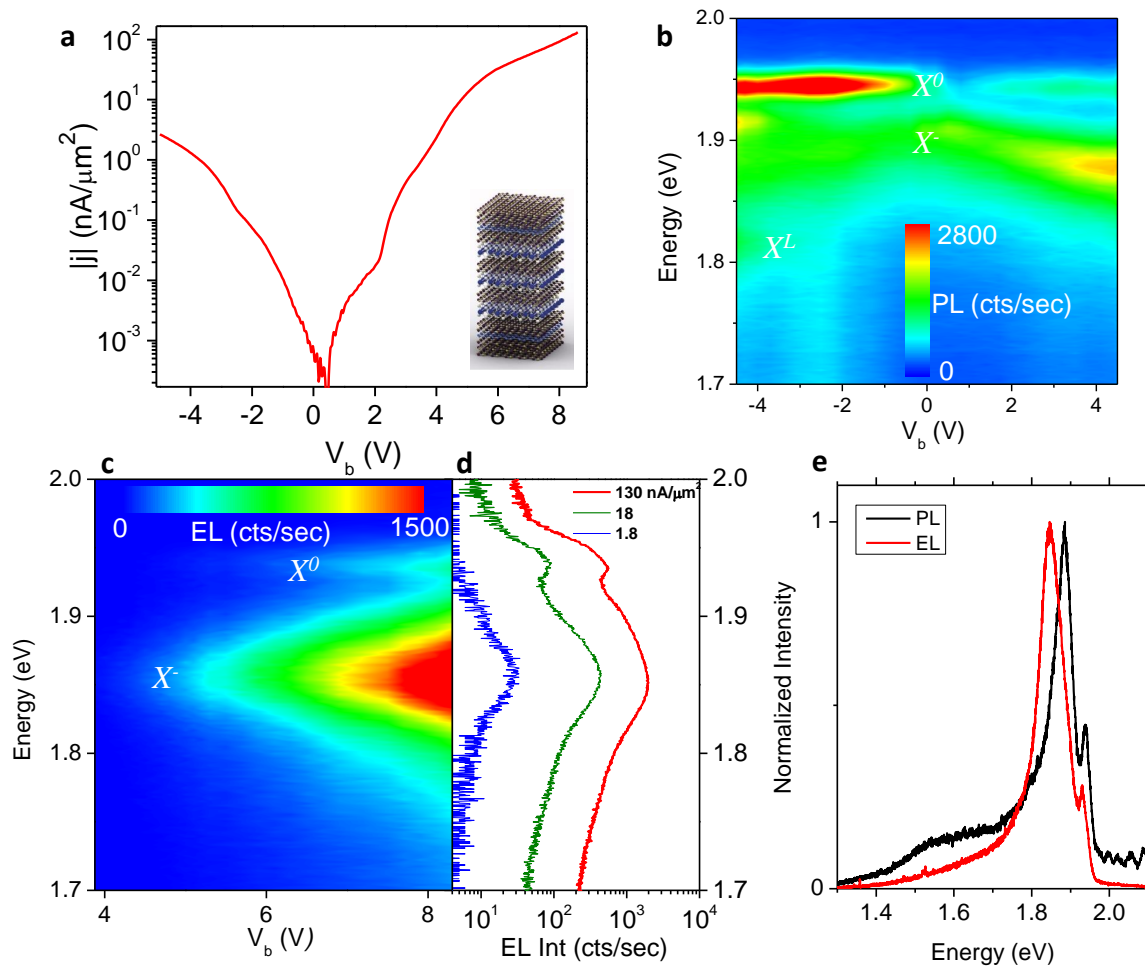
Fig. 5.6 (a) Modulus of the current density through a tree-QW structure based on MoS_2 (3MQW MoS_2-1). (b,c) Maps of PL and EL spectra for this device. (d) Individual EL spectra plotted on logarithmic scale to show the onset of EL at 1.8 nA/μm^2 (blue curve). (f) Comparison of EL and PL spectra.
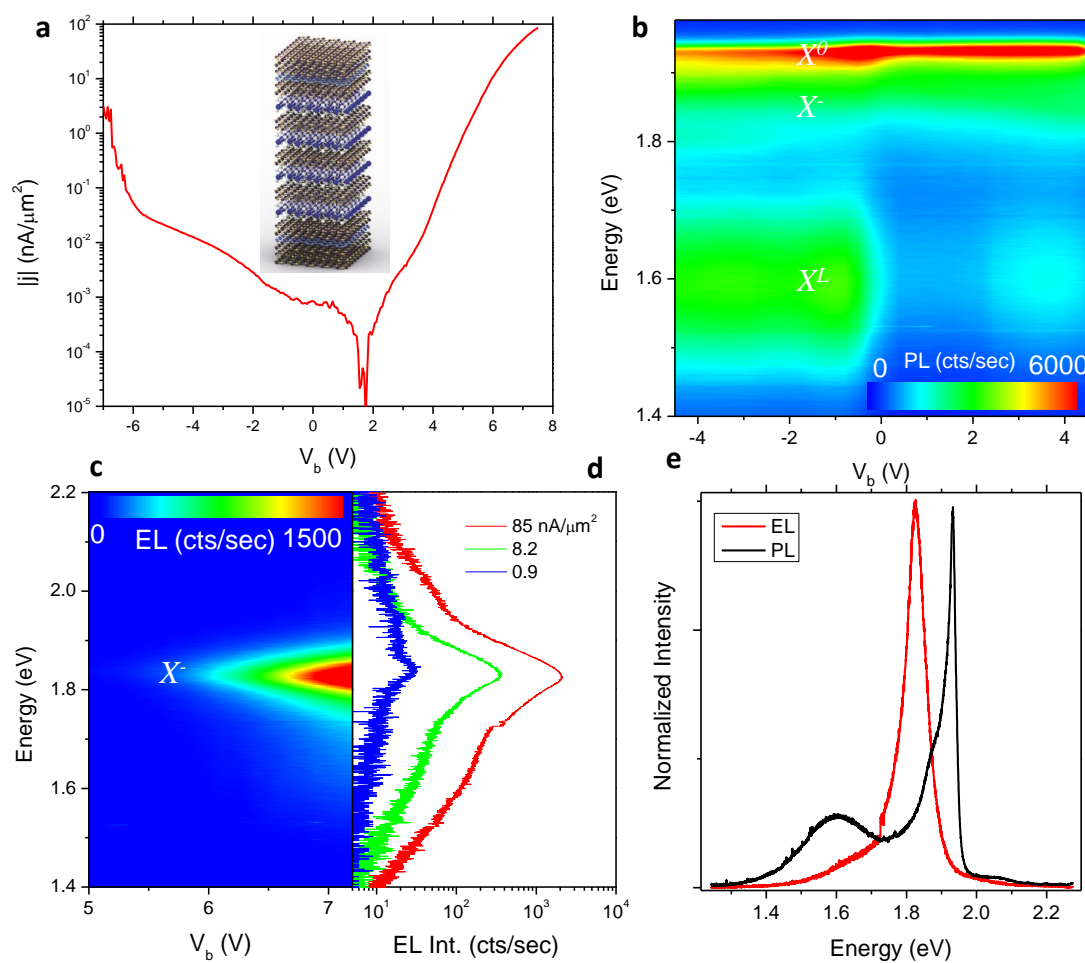
Fig. 5.7 (a) Modulus of the current density through a four-QW structure based on MoS_2 (4MQW MoS_2-1). (b,c) Maps of PL and EL spectra for this device. (d) Individual EL spectra plotted on logarithmic scale to show the onset of EL at 0.9 nA/μm^2 (blue curve). (f) Comparison of EL and PL spectra.
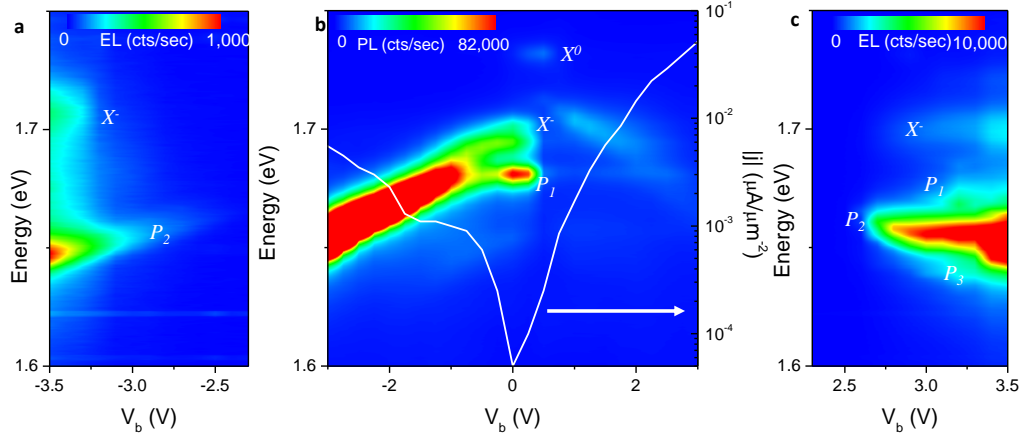
Fig. 5.8 Multiple QW well: $hBN/Gr_B/3hBN/WSe_2/3hBN/MoS_2/3hBN/Gr_T/hBN$ (WSe_2/MoS_2 QW-1). (a) EL intensity map for negative bias. (b) PL intensity map bias dependence. (c) EL intensity map for positive bias.

(WSe_2/MoS_2 QW-1). EL and PL occur here in the low energy part of the spectra and can be associated with excitonic states proposed by You *et al.* [22] in WSe_2. EL is shown in 5.8(a and c) and originates from both X^- and P_2 for negative bias and from X^-, P_1, P_2 and P_3 for positive bias. In the case of PL (5.8b)) it is much brighter at negative bias showing a notable shift of emission from 1.7 eV to lower energies for X^- and, less intense, P_1. At positive bias a relatively weak emission from X^- is seen. X^0 is observed with very low intensity at 1.72 eV and $V_b \approx 0$ V. In comparison with SQW devices, the combinational device in Fig. 5.8 exhibits more than an order of magnitude stronger both PL and EL. We associate this with charge transfer between the MoS_2 and WSe_2 layers such that electron-hole pairs are created in both layers but transfer to and recombine in the material with the smaller band-gap [23]. Such process is expected to depend strongly on band alignment, which is controlled by bias and gate voltages. This explains the complex, asymmetric V_b dependence of PL and EL in Fig. 5.8b.

5.4 Discussion

EL is seen from all nine devices characterised showing different intensities and emission wavelengths depending on the active material. An important parameter for any light emission device is the QE that is defined as the number of emitted photons N to the number of injected electron-hole pairs, as discussed in section 2.2.1. To perform an accurate estimation of EQE, a detailed study of the losses in the system was performed in order to obtain a relation between the number of counts taken with the CCD and the current. This study is presented in Appendix B.

For the SQW structures we estimate η up to 1%, this value by itself is ten times larger than that of planar p–n diodes [11, 13, 14] and 100 times better than EL from Schottky barrier devices based on single atomic layer TMDCs [12]. Our rough estimations show that the EQE for PL is lower than that for EL. Relatively low EQE found in PL indicates that the crystal quality itself requires improvement and that even higher EQE in EL may then be achieved [21]. Further improvements to η could be expected, if fabrication procedures are developed to reduce the exposure of the crystals to oxygen and atmospheric water, which may lead to their partial oxidation.

Another route to improve the QE is to increase the time quasiparticles spend in the QWs. To this end, we have employed multiple QWs stacked in series (see figs. 5.6 and 5.7), which increases the overall thickness of the tunnel barrier and enhances the probability for injected carriers to recombine radiatively. For these devices, η reaches values of $\sim$8.4 % for four QW MoS_2 device (4MQW MoS_2-1) and 5.4% for MoS_2/WSe_2 LED (MoS_2/WSe_2 QW-2), figs. 5.8. These values of QE are comparable to modern-day organic LED lighting and the concept is compatible with the popular idea of flexible and transparent electronics due to the thickness of 10–40 atoms.

A summary of all devices studied showing EL peak position, linewidth and quantum efficiency at highest injection current at 6 K is presented in table 5.1. Linewidths

Device	EL Peak Position (eV)	FWHM (meV)	QE (%)
SL $MoS_2 - 1$	1.86	30	0.30
SL $MoS_2 - 2$	1.81	90	0.51
SL WS_2	2.00	23	1.32
3MQW MoS_2	1.94	78	6.00
4MQW MoS_2	1.83	65	8.40
WSe_2/MoS_2 QW-1	1.66	14	4.80
WSe_2/MoS_2 QW-2	1.68	21	5.40

Table 5.1 The main peak position, width and quantum efficiency at highest injection current T=6 K for the electroluminescence spectra for different devices based on TMDC materials.

as narrow as 14 meV were observed in MoS_2/WSe_2 devices.

5.5 Conclusions

In summary, we have demonstrated band-structure engineering with one atomic layer precision by creating QW heterostructures from various 2D crystals including several TMDC, hBN and graphene. Our LEDs based on a single QW already exhibit quantum efficiency of the order of 1% and linewidths down to 14 meV, despite the relatively poor quality of currently available TMDC layers. This QE can be improved significantly by using multiple QWs, and LED devices consisting of 3 to 4 QWs show the QE up to 8.4% at low temperature. Combining different 2D semiconductor materials allows fine tuning of the emission spectra, and the demonstrated concept is compatible with the popular idea of flexible and transparent electronics. The range of functionalities for the demonstrated heterostructures is expected to grow further with the rapid progress in technology of chemical vapour deposition growth that will allow scaling up of production of similar devices.

References

[1] K. S. Novoselov, D. Jiang, F. Schedin, T. J. Booth, V. V. Khotkevich, S. V. Morozov, and A. K. Geim. Two-dimensional atomic crystals. *Proceedings of the National Academy of Sciences of the United States of America*, 102(30):10451–10453, 2005. doi: 10.1073/pnas.0502848102. URL `http://www.pnas.org/content/102/30/10451.abstract`.

[2] K. S. Novoselov, A. K. Geim, S. V. Morozov, D. Jiang, Y. Zhang, S. V. Dubonos, I. V. Grigorieva, and A. A. Firsov. Electric field effect in atomically thin carbon films. *Science*, 306(5696):666–669, 2004. doi: 10.1126/science.1102896. URL `http://www.sciencemag.org/content/306/5696/666.abstract`.

[3] AK Geim and IV Grigorieva. Van der waals heterostructures. *Nature*, 499(7459): 419–425, 2013.

[4] K. S. Novoselov. Nobel lecture: Graphene: Materials in the flatland*. *Rev. Mod. Phys.*, 83:837–849, Aug 2011. doi: 10.1103/RevModPhys.83.837. URL `http://link.aps.org/doi/10.1103/RevModPhys.83.837`.

[5] Yu Yao, Anthony J Hoffman, and Claire F Gmachl. Mid-infrared quantum cascade lasers. *Nature Photonics*, 6(7):432–439, 2012.

[6] Qing Hua Wang, Kourosh Kalantar-Zadeh, Andras Kis, Jonathan N Coleman, and Michael S Strano. Electronics and optoelectronics of two-dimensional transition metal dichalcogenides. *Nature nanotechnology*, 7(11):699–712, 2012.

[7] Kin Fai Mak, Changgu Lee, James Hone, Jie Shan, and Tony F. Heinz. Atomically thin mos_2: A new direct-gap semiconductor. *Phys. Rev. Lett.*, 105:136805, Sep 2010. doi: 10.1103/PhysRevLett.105.136805. URL `http://link.aps.org/doi/10.1103/PhysRevLett.105.136805`.

[8] Kin Fai Mak, Keliang He, Changgu Lee, Gwan Hyoung Lee, James Hone, Tony F Heinz, and Jie Shan. Tightly bound trions in monolayer mos2. *Nature materials*, 12(3):207–211, 2013.

[9] Di Xiao, Gui-Bin Liu, Wanxiang Feng, Xiaodong Xu, and Wang Yao. Coupled spin and valley physics in monolayers of mos$_2$ and other group-vi dichalcogenides. *Phys. Rev. Lett.*, 108:196802, May 2012. doi: 10.1103/PhysRevLett.108.196802. URL `http://link.aps.org/doi/10.1103/PhysRevLett.108.196802`.

[10] Jason S Ross, Sanfeng Wu, Hongyi Yu, Nirmal J Ghimire, Aaron M Jones, Grant Aivazian, Jiaqiang Yan, David G Mandrus, Di Xiao, Wang Yao, et al. Electrical control of neutral and charged excitons in a monolayer semiconductor. *Nature communications*, 4:1474, 2013.

[11] Jason S Ross, Philip Klement, Aaron M Jones, Nirmal J Ghimire, Jiaqiang Yan, DG Mandrus, Takashi Taniguchi, Kenji Watanabe, Kenji Kitamura, Wang Yao, et al. Electrically tunable excitonic light-emitting diodes based on monolayer wse2 pn junctions. *Nature nanotechnology*, 9(4):268–272, 2014.

[12] RS Sundaram, M Engel, A Lombardo, R Krupke, AC Ferrari, Ph Avouris, and M Steiner. Electroluminescence in single layer mos2. *Nano letters*, 13(4):1416–1421, 2013.

[13] Andreas Pospischil, Marco M Furchi, and Thomas Mueller. Solar-energy conversion and light emission in an atomic monolayer pn diode. *Nature nanotechnology*, 9(4):257–261, 2014.

[14] Britton WH Baugher, Hugh OH Churchill, Yafang Yang, and Pablo Jarillo-Herrero. Optoelectronic devices based on electrically tunable pn diodes in a monolayer dichalcogenide. *Nature nanotechnology*, 9(4):262–267, 2014.

References

[15] Pasqual Rivera, John R Schaibley, Aaron M Jones, Jason S Ross, Sanfeng Wu, Grant Aivazian, Philip Klement, Kyle Seyler, Genevieve Clark, Nirmal J Ghimire, et al. Observation of long-lived interlayer excitons in monolayer mose2–wse2 heterostructures. *Nature communications*, 6, 2015.

[16] L. Wang, I. Meric, P. Y. Huang, Q. Gao, Y. Gao, H. Tran, T. Taniguchi, K. Watanabe, L. M. Campos, D. A. Muller, J. Guo, P. Kim, J. Hone, K. L. Shepard, and C. R. Dean. One-dimensional electrical contact to a two-dimensional material. *Science*, 342(6158):614–617, 2013. doi: 10.1126/science.1244358. URL `http://www.sciencemag.org/content/342/6158/614.abstract`.

[17] SJ Haigh, A Gholinia, R Jalil, S Romani, L Britnell, DC Elias, KS Novoselov, LA Ponomarenko, AK Geim, and R Gorbachev. Cross-sectional imaging of individual layers and buried interfaces of graphene-based heterostructures and superlattices. *Nature materials*, 11(9):764–767, 2012.

[18] L. Britnell, R. V. Gorbachev, R. Jalil, B. D. Belle, F. Schedin, A. Mishchenko, T. Georgiou, M. I. Katsnelson, L. Eaves, S. V. Morozov, N. M. R. Peres, J. Leist, A. K. Geim, K. S. Novoselov, and L. A. Ponomarenko. Field-effect tunneling transistor based on vertical graphene heterostructures. *Science*, 335(6071):947–950, 2012. doi: 10.1126/science.1218461. URL `http://www.sciencemag.org/content/335/6071/947.abstract`.

[19] Sefaattin Tongay, Joonki Suh, Can Ataca, Wen Fan, Alexander Luce, Jeong Seuk Kang, Jonathan Liu, Changhyun Ko, Rajamani Raghunathanan, Jian Zhou, et al. Defects activated photoluminescence in two-dimensional semiconductors: interplay between bound, charged, and free excitons. *Scientific reports*, 3, 2013.

[20] D Sercombe, S Schwarz, O Del Pozo-Zamudio, F Liu, BJ Robinson, EA Chekhovich, II Tartakovskii, O Kolosov, and AI Tartakovskii. Optical inves-

tigation of the natural electron doping in thin mos2 films deposited on dielectric substrates. *Scientific reports*, 3, 2013.

[21] Humberto R Gutiérrez, Nestor Perea-López, Ana Laura Elías, Ayse Berkdemir, Bei Wang, Ruitao Lv, Florentino López-Urías, Vincent H Crespi, Humberto Terrones, and Mauricio Terrones. Extraordinary room-temperature photoluminescence in triangular ws2 monolayers. *Nano letters*, 13(8):3447–3454, 2012.

[22] Yumeng You, Xiao-Xiao Zhang, Timothy C Berkelbach, Mark S Hybertsen, David R Reichman, and Tony F Heinz. Observation of biexcitons in monolayer wse2. *Nature Physics*, 2015.

[23] Chul-Ho Lee, Gwan-Hyoung Lee, Arend M van Der Zande, Wenchao Chen, Yilei Li, Minyong Han, Xu Cui, Ghidewon Arefe, Colin Nuckolls, Tony F Heinz, et al. Atomically thin p–n junctions with van der waals heterointerfaces. *Nature nanotechnology*, 2014.

Chapter 6

Temperature-dependent behaviour of MoSe$_2$ and WSe$_2$ van der Waals heterostructure LEDs

6.1   Introduction

Recently molybdenum and tungsten dichalcogenides (MoX$_2$ and WX$_2$), have attracted considerable attention following the discovery of the indirect-to-direct band gap transition [1, 2] and the coupling of the spin and valley degrees of freedom in atomically thin layers[3]. Both in WX$_2$ and MoX$_2$, electrons and holes form excitons exhibiting very high binding energies [4–6] and stability at room temperature [1–3, 7, 8], making them attractive for optoelectronic devices.

Further to this, an important band-structure property arising from the strong spin-orbit interaction in these compounds has been predicted by density functional theory [9, 10] (see Fig. 6.1A-B): in WX$_2$ (MoX$_2$) the lowest energy states in the conductance band and the highest energy states in the valence band have the opposite (same) spin orientations preventing (enabling) their recombination with emission of a photon. For

this reason, according to the spin-state ordering predicted by the theory, the lowest energy excitonic sub-band in WX$_2$ corresponds to dark excitons, separated from the bright exciton sub-band by the energy approximately equal to the electron spin-orbit splitting Δ_{SO} of the order of 30-40 meV [9–12]. In this chapter we will show that such band-structure properties of WX$_2$ strongly impact on the LED performance, similar to the structures presented in chapter 5, leading to significant enhancement of the room temperature external quantum efficiency of ∼10 % for the WSe$_2$ LEDs in the EL regime. A comparison with a MoSe$_2$ LED will be carried out, where a more common behaviour is observed: EL intensity falls by up to 100 times when the temperature is varied from 10 to 300 K leading to a reduction of the quantum efficiency.
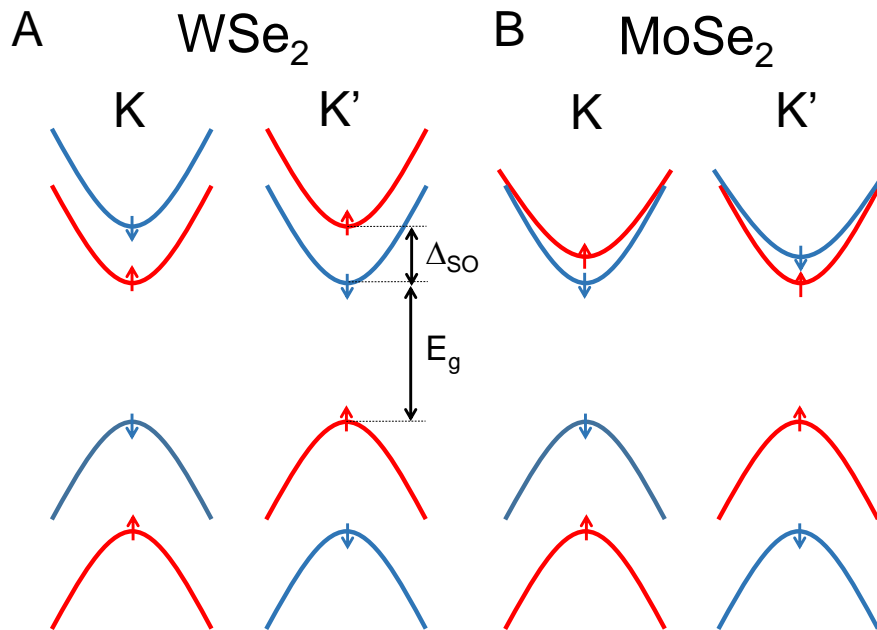

Fig. 6.1 Schematic representation of the band structure of (A) WSe$_2$ and (B) MoSe$_2$. Red and blue arrows denote spin orientation.

6.2   Samples and experimental methods

The LEDs used in this chapter are identical to the devices presented in chapter 5 fabricated with the lift/peel method described in section 2.1.2. In the present case the TMDCs used were single layers of WSe_2 and $MoSe_2$. Fig. 6.2A shows schematically the structure: Gr_B/3hBN/WSe_2/3hBN/Gr_T. A bias voltage V_B is applied between the two graphene contacts, hBN layers act as tunnel barriers and the WSe_2 is the active semiconductor layer.

Optical characterisation of the LEDs was carried out using μPL setup shown in fig. 2.8 with a 532 nm diode laser for excitation and a helium flow cryostat that allows temperature dependent measurements from 6 to 300 K. EL was obtained applying bias voltage with a source-meter device (Keithley 2400).
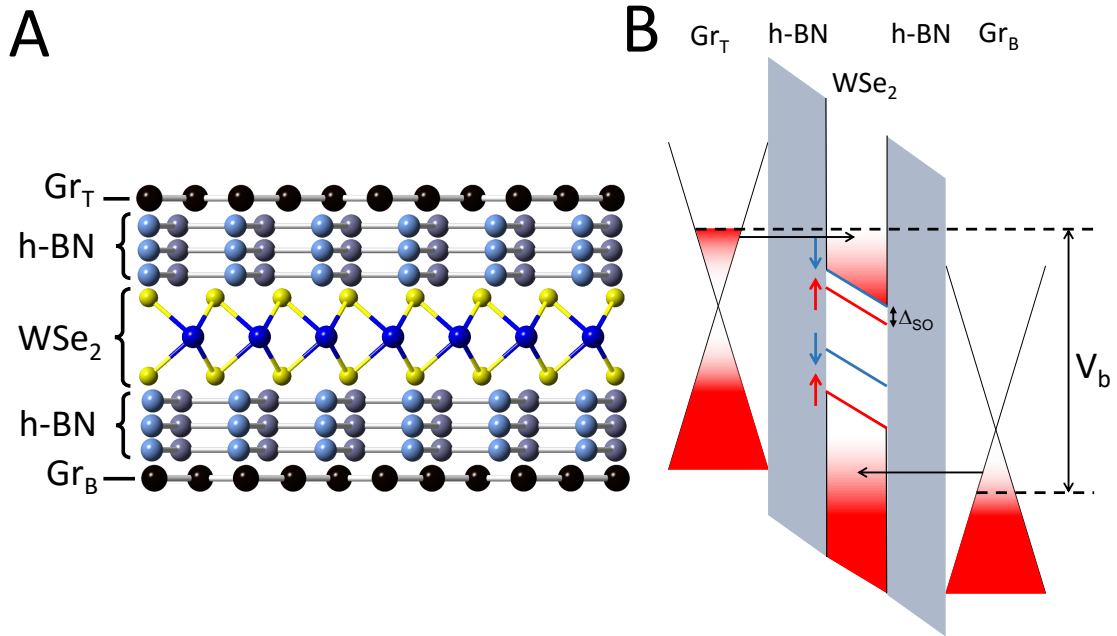

Fig. 6.2 (A) Schematic of the WSe_2 LED architecture. (B) Band alignment at high bias of a WSe_2 LED.

6.3 Results

Fig. 6.2B shows the band structure of an LED based on WSe$_2$. By applying bias voltage, V$_b$, between the two graphene electrodes, it is possible to set conditions for electron (hole) injection into the conductance (valence) band of the WSe$_2$ layer. The hBN barriers act to control the lifetime of the charge carriers inside the TMDC layer leading to increased probability of radiative recombination: for a long enough dwell time of the charge carriers controlled by the thickness of hBN, excitons forming in the WSe$_2$ layer can recombine with light emission. The same effect occurs in a MoSe$_2$ based LED. Full optical characterisation including EL and PL at different temperatures was performed for both structures in order to make a comparison and analyse the results influenced by the spin-orbit effects described above.

6.3.1 MoSe$_2$ device

As the temperature dependence of the LEDs is the key study of this work, it is necessary to describe the behaviour of the excitons in the devices. For this reason a temperature dependence of PL was carried out. This is presented in fig. 6.3A-D. In 6.3A, a PL spectrum at 5 K can be observed, the two well resolved peaks correspond to X^0 (1.65 eV) and X^- (1.62 eV, binding energy E_c=30 meV) with linewidths of 10.4 meV and 8.6 meV respectively (calculated with the lorentzian fits shown in blue and red solid lines, respectively). In 6.3B, a normalized temperature dependence from 5 to 300 K is shown. X^- line dominates up to 55 K when it starts vanishing while X^0 remains up to room temperature. The peak positions of both lines are plotted in 6.3C as a function of temperature in order to see the band gap (E_g) dependence with T (red circles for X^0 and black squares for X^-). Solid lines are fittings done using the

Bose-Einstein model [13]:

$$E_g(T) = E_g(0) - \frac{2\alpha_B}{e^{\frac{\Theta_E}{T}} - 1} \tag{6.1}$$

where $E_g(0)$ is the band gap at base temperature, α_B represents the strength of the exciton-phonon interaction and Θ_E corresponds to the average phonon temperature. The values obtained were $E_g(0)$=1.648 eV, α_B=45 meV and Θ_E=250 K for X^0 and $E_g(0)$=1.618 eV, α_B=50 meV and Θ_E=250 K for X^-. In 6.3D, Arrhenius fits using the following equation:

$$\frac{I(T)}{I(T = 5K)} = \frac{1}{1 + e^{-E_1/k_B T}} \tag{6.2}$$

for PL intensities of both lines are shown, this allows to calculate a activation energies E_1 of 20 and 25 eV for X^0 and X^-, respectively. This plot clearly shows how X^- (black squares) decays faster with temperature than X^0 (red circles).

Once knowing the excitonic behaviour of MoSe$_2$ through PL, electrically driven experiments on LEDs were performed. This is summarized in fig. 6.4A-F. PL bias-dependence at T=6 K is shown in fig. 6.4B, X^0 and X^- are observed for $|V_b|$ <1.5 V at 1.63 meV and 1.61 meV, respectively. X^0 gets weaker for $|V_b|$ >1.5 V. The current density is plotted with a white line in fig. 6.4B). Fig. 6.4A shows EL negative bias-dependence, where strong emission appears when V_b <-1.85 V from X^-. A different behaviour is seen for positive bias (fig. 6.4C) where EL, from both X^0 and X^-, is 1000 times weaker possibly due to asymmetry in the thickness of hBN barriers. An EL spectrum for V_b=2 V is plotted in fig. 6.4E showing features similar to those in the PL regime. Temperature dependent EL measurements were also performed: in fig. 6.4D spectra taken at 6 K (blue), 150 K (green) and 300 K (red) for V_b=-2 V are presented showing a significant EL reduction with T. For positive bias, EL rapidly decreases to zero when T≃40 K. The Arrhenius fit in 6.4F for EL at -2V shows an
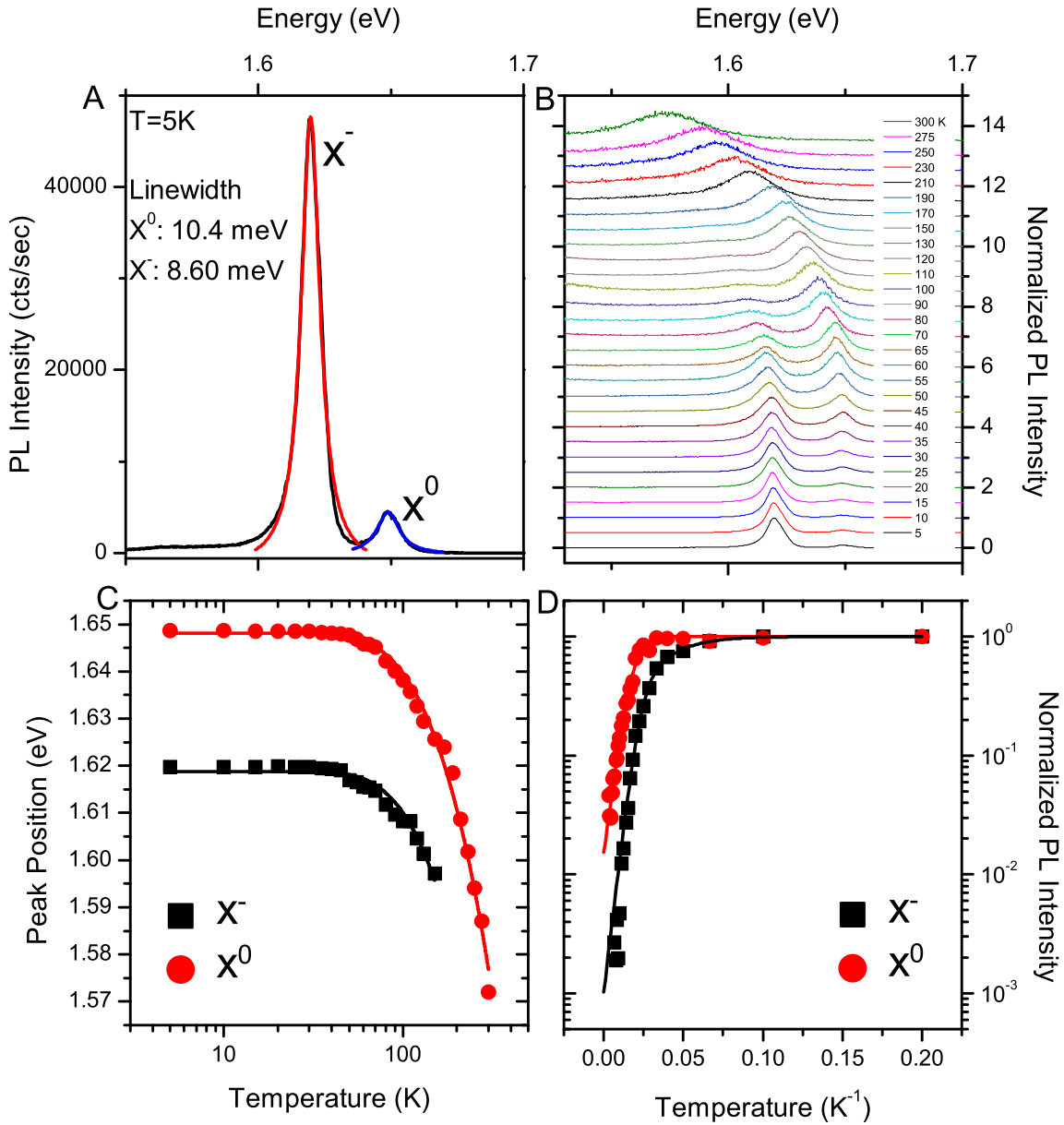
Fig. 6.3 (A) Typical PL spectrum of MoSe$_2$ LED taken at T=5 K with 10 μW showing two characteristic peaks attributed to a neutral (X^0) and charged (X^-) exciton with a measured linewidth of 10.4 meV and 8.6 meV respectively obtained from the Lorentzian fittings (red and blue solid lines). (B) Normalized PL temperature dependence of MoSe$_2$ LED from 5 to 300 K. (C) Peak positions of X^0 (red) and X^- (black) as a function of temperature. Solid lines indicate fittings with Bose-Einstein model (eq. 6.1). (D) Arrhenius plot of the PL yield for both X^0 (red) and X^- (black), fittings with eq. 6.2 are showed in red and solid lines to calculate activation energies E_1 of 20 and 25 meV for X^0 and X^-, respectively.

activation energy of 30 meV.

6.3.2 WSe$_2$ device

Similar to the experiments presented for a MoSe$_2$ LED, PL was first studied in WSe$_2$. Fig. 6.5A shows a PL spectra taken at T=6 K and excitation power of 50 μW. Using the notation adopted in You et al [14], the peaks observed are neutral exciton X^0 (1.733 eV, blue line) and trion X^- (1.70 eV, red) as well as a number of additional features, with the most pronounced peaks P_1 (1.675 eV) and P_2 (1.652 eV). Linewidths obtained with lorenzian fits are shown in the graph. In fig. 6.5B, normalized PL temperature dependence from 6 to 300 K can be observed. X^0 is visible at all temperatures while the three additional peaks eventually disappear with P_1 and P_2 becoming negligible above 80 K. The band gap temperature dependence for X^0 and X^- is plotted in fig. 6.5C. By doing the same analysis as in MoSe$_2$ using eq. 6.1, the following values are calculated: $E_g(0)$=1.734 eV, α_B=70 meV and Θ_E=270 K for X^0 and $E_g(0)$=1.706 eV, α_B=60 meV and Θ_E=270 K for X^-. The Arrhenius plot in 6.5D was obtained with integrated PL intensities over the whole spectra for all temperatures to calculate an activation energy of ∼40 meV. Strikingly PL intensity increases with temperature, opposite to the behaviour observed in MoSe$_2$.

Fig. 6.6A,C shows typical light emission behaviour of a WSe$_2$ LED at low T=6K. 6.6A,C show that for biases |V$_b$|>2 V, strong EL is observed. The peaks in EL spectra are clearly identifiable, using the description of PL features as shown in figs. 6.6A,C. For negative bias, EL originates from X^- and P_1 while for positive bias the four peaks X^0, X^-, P_1 and P_2 are observed. Similar to PL, when T increases, the neutral exciton line dominates. This can be corroborated in fig. 6.6D where EL spectra for V_b=2.3 V at 6K (black), 20 K (red), 40 K (green) and 80 K (blue) are plotted. It is worth noting that, although features P_1, P_2 are always present in all the LEDs measured,
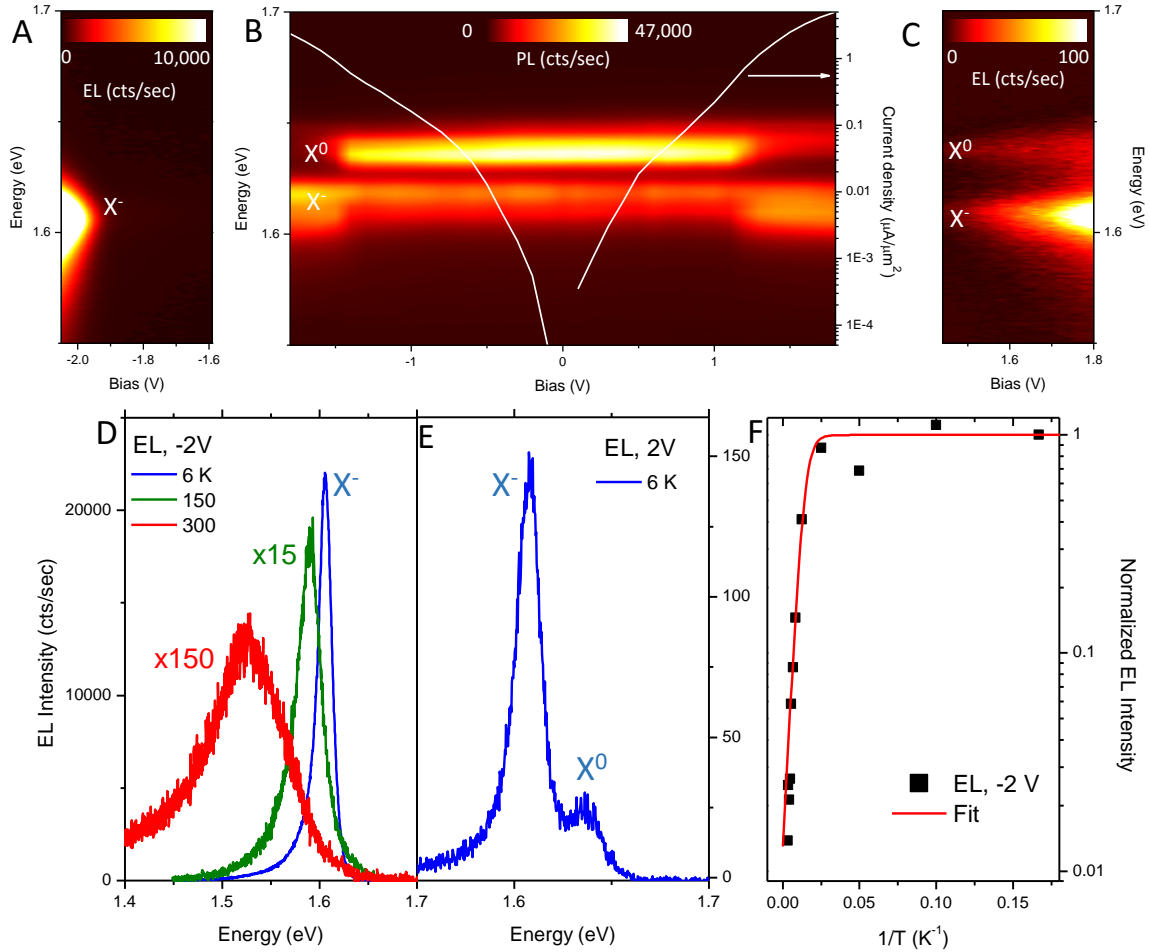
Fig. 6.4 Contour maps of the EL spectra from a MoSe2 LED at T=6 K for negative (A) and positive (C) bias voltage. (B) PL contour map as a function of V$_b$, measured at an excitation power of 20 μW and excitation energy of 2.33 eV. White curve in (B) is the j-V curve. (D) Low temperature electroluminescence spectra collected for a MoSe$_2$ LED at several temperatures at a fixed excitation bias voltage. (E) Electroluminescence spectra taken at 6 K with V$_b$=2 V for a MoSe$_2$ LED. (F) Arrhenius plot of the EL yield with temperature for the MoSe$_2$ LED, fit shown with a red solid line using eq. 6.2 gives calculated activation energy E_1 of $\sim$30 meV.
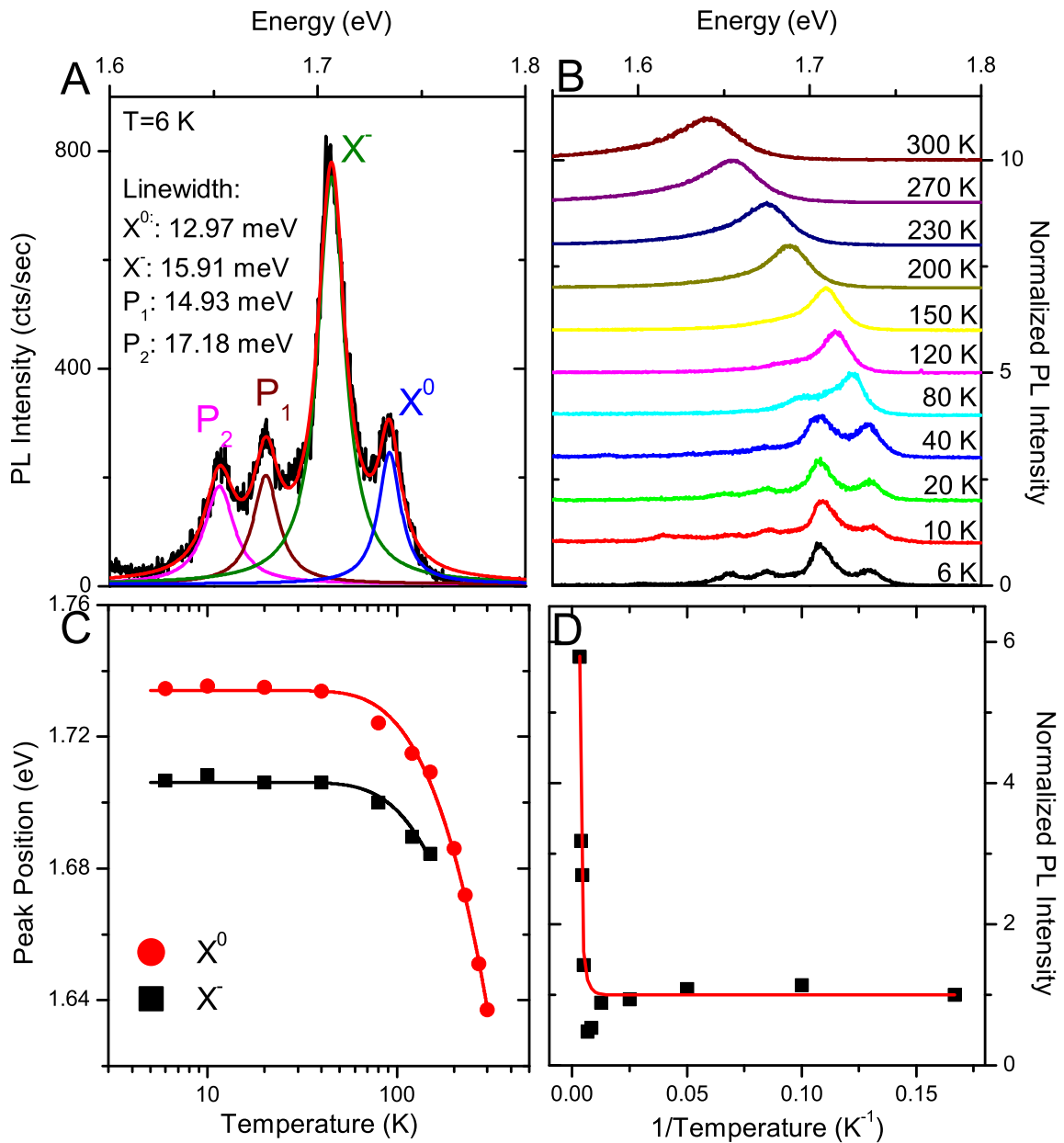
Fig. 6.5 (A) Typical PL spectrum of WSe$_2$ LED taken at T=6 K with 50 μW showing four characteristic peaks attributed to a neutral (X^0) and charged(X^-) excitons and two additional feature (P_1 and P_2) with a measured linewidth of 12.97, 15.91, 14.93 and 17.18 meV respectively calculated with lorentzian fittings (blue, green, brown and pink solid lines). (B) Normalized PL temperature dependence of WSe$_2$ LED from 6 to 300 K. (C) Peak positions of X^0 (red) and X^- (black) as a function of temperature. Solid lines indicate fittings with Bose-Einstein model (eq. 6.1). (D) Arrhenius plot of the WSe$_2$ PL yield to calculate, using the eq.6.2, an activation energy E_1 of $\sim$40 meV.

their intensities relative to X^0 and X^- vary from device to device. For example, in 6.6E EL obtained at three different temperatures with a different device (WSe$_2$-LED2) (V$_b$=2.3 V) shows only emission from X^- (1.698 eV at 6 K) up to room temperature with an increase of $\sim$400 times compared to low-T. This kind of device is made with thin h-BN barriers (2 single layers) and no X^0 is observed. Finally, EL enhancement is studied in fig. 6.6F with an Arrhenius fit. Like in PL, this result contrasts with the T-dependent behaviour of EL from MoSe$_2$.

6.4   Discussion

MoSe$_2$ LED exhibits a typical behaviour with temperature: PL and EL intensity decrease when increasing temperature up to 300 K. WSe$_2$ shows the opposite behaviour with an enhancement of both PL and EL intensities at room temperature. This comparison is illustrated in Fig. 6.7. WSe$_2$ EL, shown in red squares, increases with a factor of 200 from 5 to 300 K while MoSe$_2$ EL (blue squares) decreases by a factor of $\sim$100.

The devices described in chapter 5 show a significant decrease in EL intensity by a factor exceeding 10 when the temperature was varied between 10 and 300 K. As an example, Fig. 6.8 shows EL temperature dependence of a MoS$_2$ LED. In 6.8A I-V curves from 6 to 300 K are plotted showing an increase in the current through the device with temperature of $\sim$20 μA at high bias (|V$_b$|>2 V). EL spectra in the same range of temperatures for V$_b$=2.7 V can be observed in Fig. 6.8B. An Arrhenius fit of EL yield is plotted in fig. 6.8C that allows to calculate an activation energy of 15.57 meV. The decrease in intensity corresponds to a reduction in EQE to $\sim$0.1 % at room temperature.

The strong increase of the EL with temperature in WSe$_2$ corresponds to a rise of EQE. This makes van der Waals heterostructures with embedded WSe$_2$ monolayers
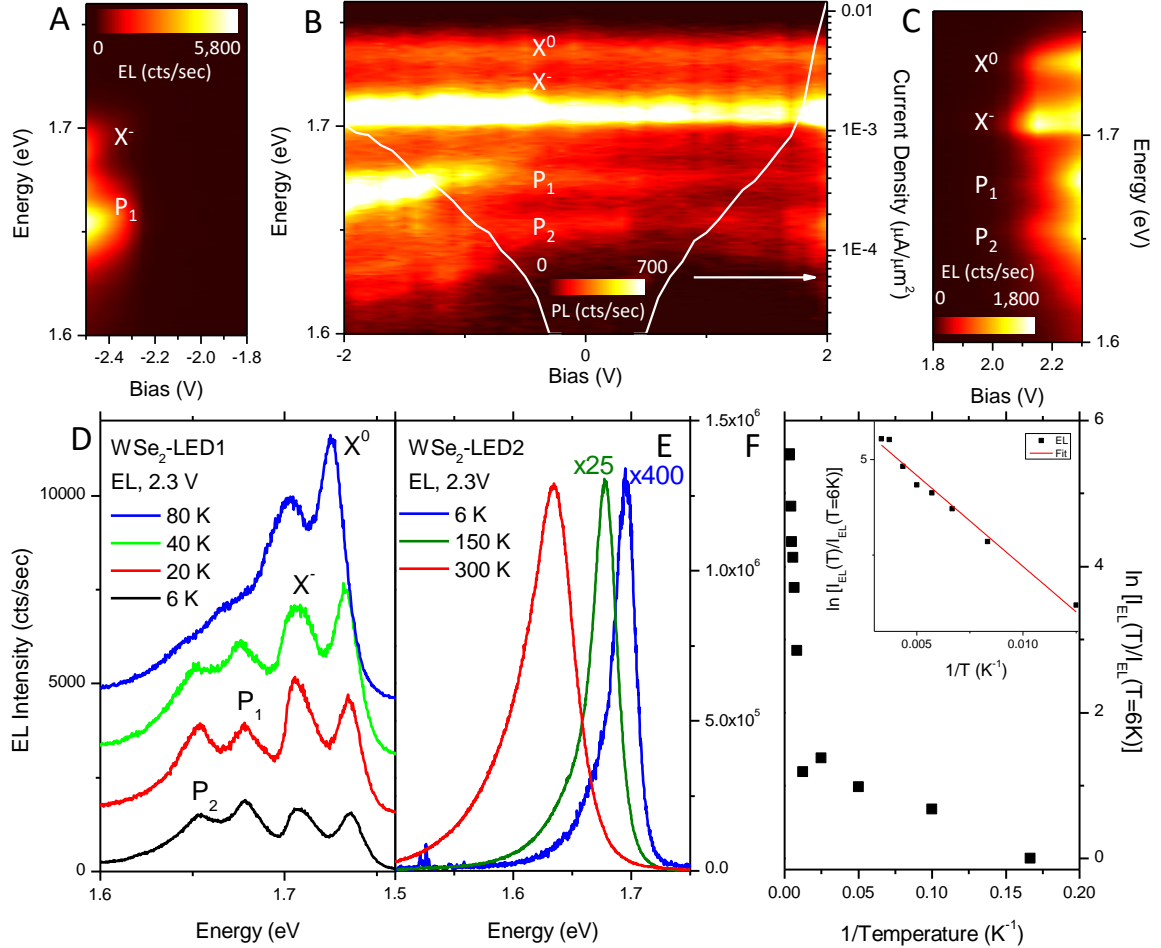
Fig. 6.6 Contour maps of the EL spectra from the WSe$_2$ LED1 at T= 6 K for negative (A) and positive (C) bias voltage. (B) PL contour map as a function of V$_b$, measured at an excitation power of 50 μW and excitation energy of 2.33 eV. White curve in (B) is the j-V curve. (D) Electroluminescence spectra collected for the WSe$_2$-LED1 at several temperatures at a fixed excitation bias voltage. (E) Electroluminescence spectra taken at different temperatures for the WSe$_2$-LED2 with two layer hBN tunnel barriers. This sample demonstrates a 200x increase of the EL output when the temperature is increased from T= 6 K to T = 300 K. (F) Arrhenius plot of the EL yield with temperature for the WSe$_2$ device shown in (E) inset: zoom in around the high temperature region used for the linear fit to calculate an activation energy of ~40 meV.
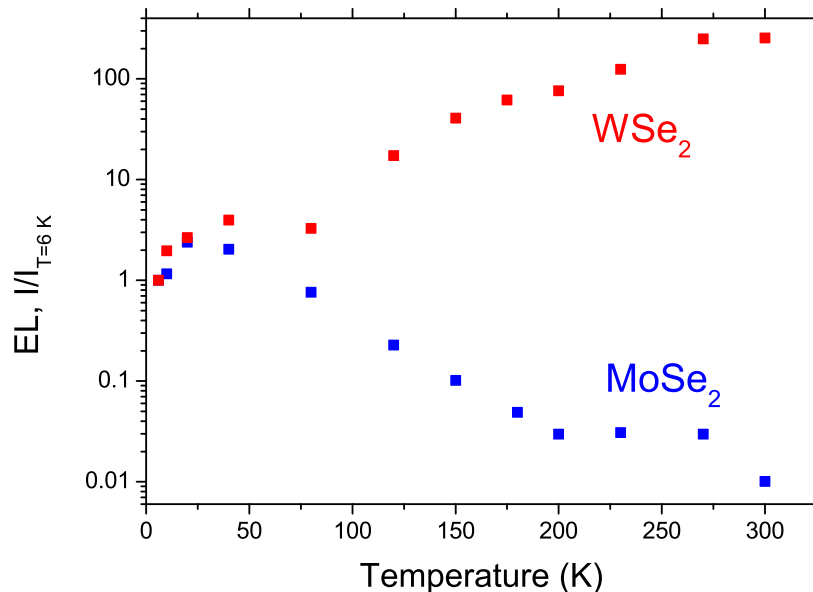
Fig. 6.7 Comparison between the temperature dependence of the electroluminescence intensity for the WSe$_2$-LED2 (blue) and MoSe$_2$ (red) showing opposite trends with increasing T. The intensities are normalised by those measured for each device at T=6 K.
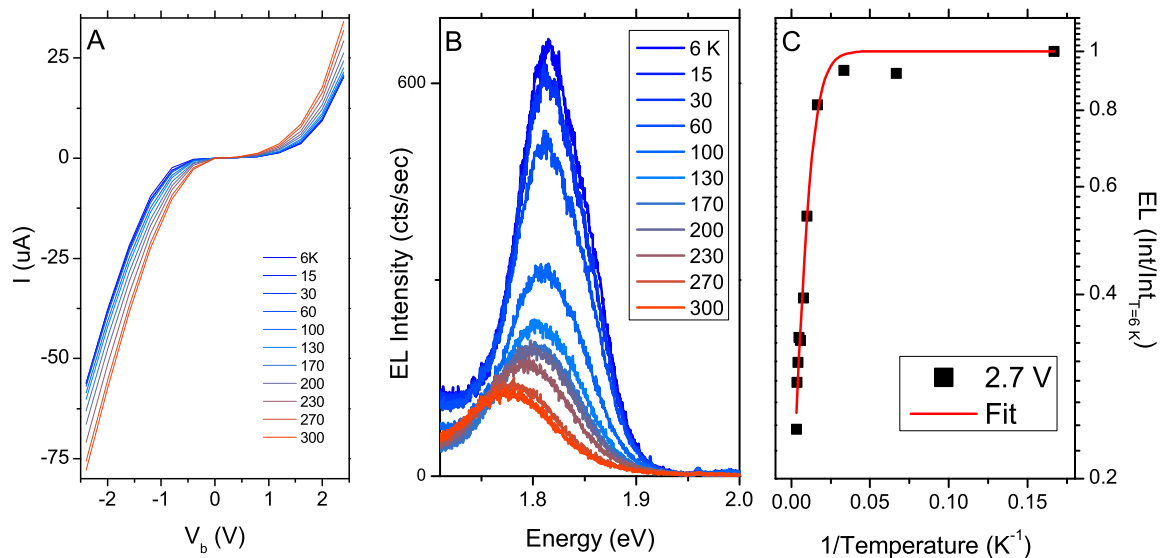

Fig. 6.8 MoS$_2$ EL Temperature dependence. (A) I-V curves taken from 6 to 300 K. (B) EL spectra with V_b=2.7 V, T=6 to 300 K. (C) Arrhenius plot for EL intensity of spectra in (B).

132

highly promising material for ultra-thin flexible LEDs. Fig. 6.9A shows EQE T-dependence for three WSe$_2$ devices. Here the EQE is calculated as described in section 2.2.1 and appendix B, similar to previous chapter. It is observed in Fig. 6.9A that the EQE shows the characteristic increase with temperature reaching 10% at T = 300 K, a factor 200-500 improvement in the room temperature performance as compared to the single-monolayer MoS$_2$ or MoSe$_2$ LEDs. In addition to this, in Fig. 6.9C we observe a monotonically increasing EQE as a function of bias voltage and injection current density to a maximum measured value of j=103 A/cm^2. Fig. 6.9B shows the EL spectra obtained from device 3 in Fig. 6.9A operated at room temperature at increasing injection current densities with a peak emission of more than 1.3 million counts per second.
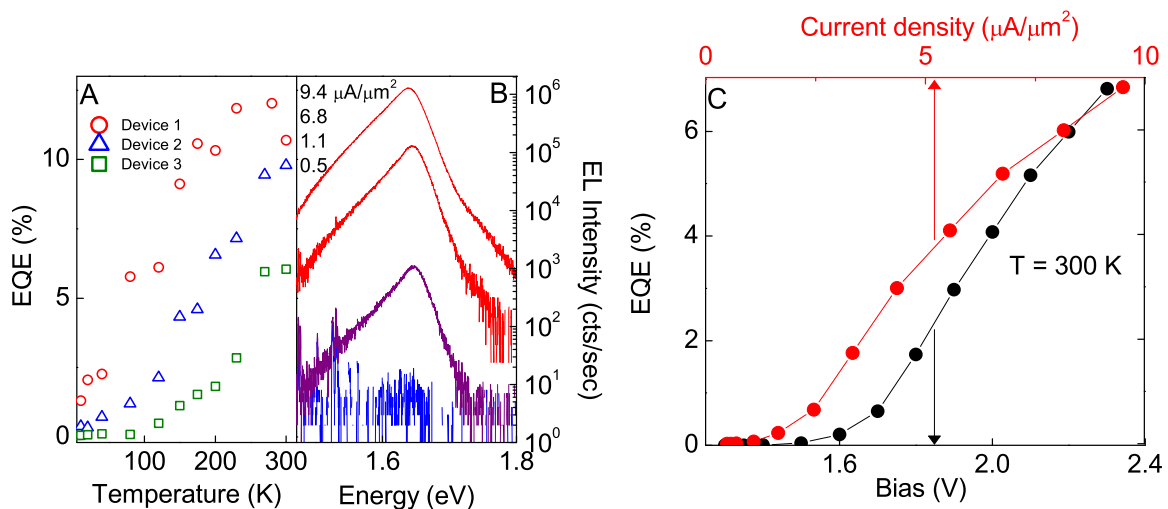
Fig. 6.9 (A) Temperature dependence of the quantum efficiency for three separate WSe$_2$ LEDs measured measured at bias voltages and injection currents of, Device 1 (2.8 V, j=0.15 μA/μm^2), Device 2 (2.8 V, j=0.5 μA/μm^2) and Device 3 (2.3 V, j=8.8 μA/μm^2). (B) Individual electroluminescence spectra plotted for four different injection current densities for Device 3. (C) The external quantum efficiency plotted against bias voltage and injection current density at T = 300 K for device 3. Note, the EQE monotonically increases even up to current densities of 10 μA/μm^2 or 1000 A/cm^2.

Indeed, a common drawback of commercial LED lighting is a suppression of the

EQE (so-called 'efficiency droop') at high injection currents caused by increased non-radiative processes [15, 16]. In contrast, the presented WSe$_2$-based van der Waals heterostructure LEDs become brighter at higher temperature, and their efficiency remains high and increases with current densities even at high j as shown in Fig. 6.9C.

We suggest that the mechanism of the unusual T-dependence of EL and PL in WSe$_2$ LEDs is related to the ordering of the spin states in the free carrier bands as illustrated in Fig. 6.1, leading to the specific ordering of the bright and dark exciton sub-bands in these materials [9, 10]. The discussion below will be focused on the behaviour of the neutral exciton, the PL and EL of which dominate at room T in the majority of LEDs described. The dark and bright exciton sub-bands are split by approximately $\Delta_{SO} \sim$ 30-40 meV. The splitting is further modified by the electron-hole exchange interaction, which is different for the bright and dark states but is of the order of 1-2 meV [9–12] and is therefore neglected in the following discussion.

At low temperature the exciton population accumulates in the low energy dark exciton sub-band, which mostly decay via (i) non-radiative escape, and (ii) phonon- and electron-assisted light-emission processes. In processes (ii), momentum and energy conservation is fulfilled as a result of the exciton scattering with phonons or electrons. It is possible, that the origin of the features P_1-P_2 is exactly through such phonon or electron assisted decay of the dark exciton, which would explain the strong intensity of those features at low T. At the same time, at low T the bright exciton sub-band is weakly populated as it is shifted to higher energy by $\sim \Delta_{SO}$ with respect to the dark exciton sub-band and therefore the intensity of the X^0 line is low.

As the temperature increases, the thermal equilibrium dictates the increase of the exciton population in the bright exciton sub-band in WSe$_2$. This population will be mostly contained in the high-k exciton 'reservoir' outside the small-k light-cone

134

states. Excitons from the reservoir will then be scattered into the light-cone where they recombine radiatively. The scattering will occur as a result of interaction with phonons and electrons, the latter is particularly significant in the EL regime.

The fact that at high T the intensity of the X^0 line increases both in PL and EL is the manifestation of such thermal activation behaviour. The rate of the X^0 line intensity increase with T depends on several factors, and will not only reflect the equilibrium Boltzmann distribution of excitons among the four exciton and trion sub-bands. In a simplified approximation, the light emission intensity will be proportional to the product of such equilibrium population in the bright exciton sub-band and the ratio of $\tau_{nr}/(\tau_{rel} + \tau_{nr})$, where τ_{nr} is a typical non-radiative decay time for the high-k reservoir excitons, and τ_{rel} a typical relaxation time of the high-k excitons into the light-cone states. Both time constants may be functions of temperature, and vary from sample to sample depending on the residual doping of the layers and device architecture (the latter for example defining the carrier dwell time in the active layer). Furthermore, the X^0 linewidth shows pronounced dependence on T, typically increasing from 10-20 meV at T=10K to over 40 meV at room T. Such homogeneous broadening would effectively relax the energy conservation required for the scattering into the light-cone states and would modify the way the reservoir states (as well as the dark excitons) contribute to PL and EL.

The factors considered above imply a non-trivial dependence of the PL and EL intensity on temperature in WSe$_2$. Indeed the overall increase of PL and EL in the range from 10 to 300 K varied between different devices. Still, the Arrhenius fit (Fig. 6.6F) to the exponential increase of the EL with increasing temperature on some of our devices yields the characteristic energy of ∼40 meV, which is in reasonable agreement with the predicted Δ_{SO} [9]. On the other hand, the MoSe$_2$ films and LEDs, where the dark exciton sub-band is higher in energy than the bright exciton sub-band,

always showed the opposite behaviour with the notable decrease of light emission with increasing T. While it is expected that the emission efficiency would decrease due to the transfer of some exciton population into the dark exciton sub-band and also into the high-k states, such a strong decrease by a factor of 100 and more may only be possible if the non-radiative escape time shortens at elevated temperature.

6.5   Conclusions

High-efficiency LEDs made from van der Waals heterostructures comprising a single atomic layer of WSe$_2$ as active light-emitting material, hBN tunnel barriers, and graphene electrodes for vertical current injection were fabricated. Such WSe$_2$-based LEDs show unexpectedly enhanced performance at room temperature compared with the low-T operation. This enhancement is also in contrast to MoSe$_2$ and MoS$_2$ LEDs studied in this thesis, where both PL and EL decrease by a factor of 10 to 100 when the temperature is varied from 10 to 300 K. With the record external room temperature efficiencies of 10%, such single layer WSe$_2$ LEDs present significant promise for future development of flexible opto-electronic components. The efficiency can be boosted further by creating multiple quantum well devices as described in chapter 5 and by the fine tuning of the h-BN tunnel barrier thickness. One of the remaining challenges is scalable production of these components, only possible with well controlled wafer-scale growth techniques [17, 18].

References

[1] Kin Fai Mak, Changgu Lee, James Hone, Jie Shan, and Tony F Heinz. Atomically thin mos 2: a new direct-gap semiconductor. *Physical Review Letters*, 105(13): 136805, 2010.

[2] Andrea Splendiani, Liang Sun, Yuanbo Zhang, Tianshu Li, Jonghwan Kim, Chi-Yung Chim, Giulia Galli, and Feng Wang. Emerging photoluminescence in monolayer mos2. *Nano letters*, 10(4):1271–1275, 2010.

[3] Xiaodong Xu, Wang Yao, Di Xiao, and Tony F Heinz. Spin and pseudospins in layered transition metal dichalcogenides. *Nature Physics*, 10(5):343–350, 2014.

[4] Ziliang Ye, Ting Cao, Kevin O'Brien, Hanyu Zhu, Xiaobo Yin, Yuan Wang, Steven G Louie, and Xiang Zhang. Probing excitonic dark states in single-layer tungsten disulphide. *Nature*, 513(7517):214–218, 2014.

[5] Keliang He, Nardeep Kumar, Liang Zhao, Zefang Wang, Kin Fai Mak, Hui Zhao, and Jie Shan. Tightly bound excitons in monolayer wse 2. *Physical review letters*, 113(2):026803, 2014.

[6] Alexey Chernikov, Timothy C Berkelbach, Heather M Hill, Albert Rigosi, Yilei Li, Ozgur Burak Aslan, David R Reichman, Mark S Hybertsen, and Tony F Heinz. Exciton binding energy and nonhydrogenic rydberg series in monolayer ws 2. *Physical review letters*, 113(7):076802, 2014.

[7] Qing Hua Wang, Kourosh Kalantar-Zadeh, Andras Kis, Jonathan N Coleman, and Michael S Strano. Electronics and optoelectronics of two-dimensional transition metal dichalcogenides. *Nature nanotechnology*, 7(11):699–712, 2012.

[8] AK Geim and IV Grigorieva. Van der waals heterostructures. *Nature*, 499(7459):419–425, 2013.

[9] Andor Kormányos, Guido Burkard, Martin Gmitra, Jaroslav Fabian, Viktor Zólyomi, Neil D Drummond, and Vladimir Fal'ko. k · p theory for two-dimensional transition metal dichalcogenide semiconductors. *2D Materials*, 2(2):022001, 2015.

References

[10] Hongyi Yu, Gui-Bin Liu, Pu Gong, Xiaodong Xu, and Wang Yao. Dirac cones and dirac saddle points of bright excitons in monolayer transition metal dichalcogenides. *Nature communications*, 5, 2014.

[11] Di Xiao, Gui-Bin Liu, Wanxiang Feng, Xiaodong Xu, and Wang Yao. Coupled spin and valley physics in monolayers of mos 2 and other group-vi dichalcogenides. *Physical Review Letters*, 108(19):196802, 2012.

[12] Hanan Dery and Yang Song. Polarization analysis of excitons in monolayer and bilayer transition-metal dichalcogenides. *arXiv preprint arXiv:1506.06686*, 2015.

[13] L Vina, S Logothetidis, and M Cardona. Temperature dependence of the dielectric function of germanium. *Physical Review B*, 30(4):1979, 1984.

[14] Yumeng You, Xiao-Xiao Zhang, Timothy C Berkelbach, Mark S Hybertsen, David R Reichman, and Tony F Heinz. Observation of biexcitons in monolayer wse2. *Nature Physics*, 2015.

[15] Jinqiao Xie, Xianfeng Ni, Qian Fan, Ryoko Shimada, Ümit Özgür, and Hadis Morkoç. On the efficiency droop in ingan multiple quantum well blue light emitting diodes and its reduction with p-doped quantum well barriers. *Applied Physics Letters*, 93(12):1107, 2008.

[16] Joachim Piprek. Efficiency droop in nitride-based light-emitting diodes. *physica status solidi (a)*, 207(10):2217–2225, 2010.

[17] Kibum Kang, Saien Xie, Lujie Huang, Yimo Han, Pinshane Y Huang, Kin Fai Mak, Cheol-Joo Kim, David Muller, and Jiwoong Park. High-mobility three-atom-thick semiconducting films with wafer-scale homogeneity. *Nature*, 520 (7549):656–660, 2015.

[18] Yu-Chuan Lin, Ram Krishna Ghosh, Rafik Addou, Ning Lu, Sarah M Eichfeld, Hui Zhu, Ming-Yang Li, Xin Peng, Moon J Kim, Lain-Jong Li, et al. Atomically thin resonant tunnel diodes built from synthetic van der waals heterostructures. *Nature communications*, 6(7311), 2015.

Chapter 7

Conclusions

In this thesis optical characterisation of two different groups of two dimensional semi-conductor materials was carried out: III-VI compounds and transition metal dichalco-genides (TMDCs). With the latter, light emitting diodes based on van der Waals heterostructures were realised and characterised using photoluminescence (PL) spec-troscopy. The key results for each topic were the following:

1. In chapter 3, low temperature cw and time resolved PL of two dimensional GaTe and GaSe two dimensional films was presented. It was observed that PL intensity decreases significantly when the film thickness is reduced for both materials and that films thinner than 7 nm show no detectable PL. We claim that the reduction of quantum yield is a consequence of non-radiative processes associated with surface states. A model was proposed to differentiate between the fast non-radiative carrier escape to surface traps in the thin 15–20 nm layers near the film surface, and slower decay in an intermediate region of the film, where the carriers first move to the surface layers and then decay. The model accounts for the change in the character of the PL decay for thin films with thicknesses less than 30–40 nm, where we expect only fast direct relaxation to

surface traps. No other trends with thickness were observed including notable changes in PL lifetime and blue shift which would be expected due to quantum confinement. Further protection of the films such as oxygen-free encapsulation is needed to hinder the fast PL intensity decay. This will allow III-VI materials to be considered as building blocks for van der Waals heterostructures.

2. In chapter 4, the stability of thin films of InSe and GaSe was studied using PL and Raman spectroscopy. We showed that GaSe films are affected by chemical interactions on the surface layers leading to film erosion with an average rate of 0.14 ± 0.05 nm/hour when they are exposed to ambient conditions. This was observed as a significant decrease over time of PL and Raman intensity. In the case of InSe, degradation under the same condition is much weaker. It demonstrates that this III-VI layered material is a good candidate to be used in van der Waals heterostructure. A reduction of the degradation rate by more than two orders of magnitude in GaSe films can be achieved by using encapsulation of the films with dielectrics such as Si_xN_y or SiO_2.

3. In chapter 5, light emitting diodes based on van der Waals heterostructures fabricated by stacking graphene, insulating hexagonal boron nitride and various semiconducting TMDC monolayers were presented. Our devices made with a single quantum well (QW) exhibit an external quantum efficiency (EQE) of $\sim1\%$ under electrical pumping. When increasing the number of quantum wells, the quantum efficiency increases up to $\sim10\%$. The emission can be tuned over a wide range of wavelengths by appropriately choosing and combining 2D semiconductors such as MoS_2, WS_2 and WSe_2.

4. In chapter 6, light emitting diodes based on van der Waals heterostructures made from WSe_2 and $MoSe_2$ were presented. Here we show that the EQE in van der

Waals LEDs comprising monolayers of WSe_2 unexpectedly grows with temperature. Room temperature EQE under electrical injection of 10% was demonstrated in single WSe_2 monolayer QW LEDs exceeding by more than 500 the previous best performance of MoX_2 QWs in ambient conditions. Such temperature activated behaviour is a consequence of the strong spin-orbit interaction and specific ordering of the spin states in tungsten dichalcogenides resulting in the lowest-energy dark exciton sub-band. A comparison with a $MoSe_2$-based LED was carried out to emphasize this behaviour. In $MoSe_2$ LEDs strong decrease of EQE was observed at elevated temperatures.

Appendix A

Model for PL intensity dependence on thickness of GaTe and GaSe thin films

In order to describe the observed trend of photoluminescence (PL) intensity as a function of film thickness h_{film} in GaSe and GaTe thin films we have developed a simplified rate equation model described below. It describes the behavior of photo-excited carriers in terms of populations of e-h pairs, i.e. electrons and holes are not treated separately for simplicity.

A.1   Modeling

As shown in Fig. 3.7(b) we assume that the film is divided into three regions: (1) two regions of thickness h_0 near the film surfaces where fast carrier relaxation to surface traps occurs leading to non-radiative carrier escape; (2) a 'normal' region of thickness $h_{film} - 2h_0$ in the central part of the film where carriers do not decay non-radiatively, but can escape into the regions (1), where they undergo non-radiative decay. Here the

Model for PL intensity dependence on thickness of GaTe and GaSe thin films

h_0 value may be associated with a depletion depth or an average surface trap radius[1]. It is assumed to be independent of the film thickness and may be different for films made of different materials.

In region (1), in first approximation the average time it takes for the carrier/e-h pair to escape non-radiatively is proportional to half the thickness of region (1) (can be understood as the average time for the carrier to reach the surface or as the overlap of the wavefunction of the carrier and the trap). This half-thickness is given by $h_0/2$ for the two regions adjacent to the surface for film thicknesses $h_{film} > 2h_0$, and is $h_{film}/4$ for $h_{film} \leq 2h_0$, when the two surface regions merge. Thus we introduce a non-radiative decay time in the regions of type (1) as $\tau_{nr1} = (h_0/2)/u_1$ for $h_{film} > 2h_0$, and $\tau_{nr1} = (h_{film}/4)/u_1$ for $h_{film} \leq 2h_0$. Here u_1 is a constant with the dimensions of meter per second.

In region (2), the non-radiative escape time reflects the average time it takes for a carrier or an e-h pair to reach any of the regions (1). The underlying mechanism for this process may be depletion and band-bending expected at the film surface leading to charge separation and non-radiative decay [1]. We assume that once the carrier or e-h pair has reached region (1) it escapes non-radiatively. In first approximation, the average time it takes a carrier/e-h pair to reach region (1) is proportional to half the thickness of region (2), $h_{film}/2 - h_0$. Thus we introduce a non-radiative decay time in region (2) as $\tau_{nr2} = (h_{film}/2 - h_0)/u_2$. Here u_2 is a constant with the dimensions of meter per second, effectively corresponding to the average carrier velocity in region (2). Notably, in films with $h_{film} \leq 2h_0$, region (2) does not exist, and the only non-radiative escape that we consider is due to the escape to traps as described above for region (1).

In equations below, we denote e-h pair populations in regions (1) and (2) as N_1 and N_2, respectively, and the population of the 'PL states' as N_{loc}. Appropriately,

$N_2 = 0$ for $h_{film} \leq 2h_0$. In both regions, e-h pairs relax with the time τ_{rel} into the 'PL states' giving rise to radiative recombination. Non-radiative escape from the 'PL states' is neglected. This assumption is based on the fact that in most cases PL is observed from the tightly-bound localized states. N_{loc} states decay radiatively with a characteristic time τ_{PL}, so that the PL intensity $I_{PL} = N_{loc}/\tau_{PL}$. Saturation of 'PL states' is neglected as the data reported in Figs.3.2(b),3.3(b) is measured for the laser powers where saturation effects are unimportant. The light absorption coefficient, α is assumed to be the same in both types of regions (1) and (2). For the small thicknesses of the films that we consider, the e-h pair generation rate is equal to $P\alpha$ multiplied by the thickness of the regions (1) or (2) as given below. Here P is the e-h pair generation rate due to the laser excitation rescaled to account for the PL detection efficiency.

The following rate equations can thus be introduced for the case $h_{film} > 2h_0$:

$$
\begin{aligned}
dN_1/dt &= 2h_0 P\alpha - N_1/t_{rel} - N_1/\tau_{nr1} \\
dN_2/dt &= (h_{film} - 2h_0)P\alpha - N_2/t_{rel} - N_2/\tau_{nr2} \\
dN_{loc}/dt &= N_1/\tau_{rel} + N_2/\tau_{rel} - N_{loc}/\tau_{PL}
\end{aligned}
$$

For the case $h_{film} \leq 2h_0$ we will have:

$$
\begin{aligned}
dN_1/dt &= Ph_{film}\alpha - N_1/t_{rel} - N_1/\tau_{nr1} \\
N_2 &= 0 \\
dN_{loc}/dt &= N_1/\tau_{rel} - N_{loc}/\tau_{PL}
\end{aligned}
$$

In the steady-state case we obtain the following expression for PL intensity for $h_{film} > 2h_0$:

$$
I_{PL} = 2h_0 P\alpha/(1 + \tau_{rel}/\tau_{nr1}) + (h_{film} - 2h_0)P\alpha/(1 + \tau_{rel}/\tau_{nr2}), \quad \text{(A.1)}
$$

147

where $\tau_{nr1} = \tau_1 h_0/2$ and $\tau_{nr2} = \tau_2(h_{film}/2 - h_0)$, and for $h_{film} \leq 2h_0$

$$I_{PL} = h_{film}P\alpha/(1 + \tau_{rel}/\tau_{nr1}), \quad \text{(A.2)}$$

where $\tau_{nr1} = (h_{film}/4)/u_1$.

By substituting these expressions for the non-radiative decay times directly we obtain for PL intensity for $h_{film} > 2h_0$:

$$I_{PL} = 2h_0^2 P\alpha/(h_0 + 2\tau_{rel}u_1) + (h_{film} - 2h_0)^2 P\alpha/(h_{film} - 2h_0 + 2\tau_{rel}u_2). \quad \text{(A.3)}$$

For $h_{film} \leq 2h_0$ we get:

$$I_{PL} = h_{film}^2 P\alpha/(h_{film} + 4\tau_{rel}u_1), \quad \text{(A.4)}$$

A.2   Results of the modeling

A.2.1   Results for GaSe thin films

According to Eqs. A.3, A.4, we have four parameters, with which we describe the observed dependence of I_{PL} on the film thickness: h_0, the products $P\alpha$, $\tau_{rel}u_1$ and $\tau_{rel}u_2$.

Further analysis of Eqs.A.3, A.4 shows that these parameters are not completely independent. This becomes obvious if we note that for small h_{film} where we expect fast non-radiative process (i.e. large $\tau_{rel}u_1$) we get $h_{film} \ll 4\tau_{rel}u_1$, and Eq.A.4 reduces to a simple parabolic dependence: $I_{PL} \approx h_{film}^2 P\alpha/(4\tau_{rel}u_1)$. This function is independent of individual parameters $P\alpha$ and $\tau_{rel}u_1$, and depends on their ratio only.

For large h_{film} where we expect slower non-radiative process we get $(h_{film} - 2h_0)$

of the order of $2\tau_{rel}u_2$, and a simple approximation can be used for Eq.A.3 giving $I_{PL} \approx (h_{film} - 2h_0)P\alpha$. From here we find that $P\alpha$ should be of the order of 10^5 nm^{-1}s^{-1}.

The two functions described by Eqs.A.3, A.4 and especially their asymptotics have significantly different form, effectively with different 'slopes' as seen e.g. in Fig.3.3(b) for the case of GaSe. For GaSe data in Fig.3.3(b), it is relatively easy to define the position of a characteristic kink around h_{film} =30 nm, where the behavior changes. We use this observation to fix the value of h_0 to 15 nm.

In the next step, we have explored a range of fitting functions providing a reasonable agreement with the experiment. We conclude that our model can reliably predict the order of magnitude of the fitting parameters, but not the actual value. So we find that $\tau_{rel}u_1$ is of the order of a 1000 nm and $\tau_{rel}u_2$ is of the order of a 100 nm.

As an illustration for the GaSe data, in Fig.3.3(b) we show a fitting with $P\alpha = 3.5 \times 10^5$nm^{-1}s^{-1}, $\tau_{rel}u_1 = 2900$ nm and $\tau_{rel}u_2 = 150$ nm. The figure also shows the variation of PL intensity as would be expected from the change in absorption only (dashed line). This would correspond to a thickness independent non-radiative processes occurring with the same rate in the whole volume of the film. This curve is described by the expression $I_{PL} = I_{GaSe}[1 - exp(-\alpha_{GaSe}h_{film})]$, where I_{GaSe} is the PL intensity for films with $h_{film} \approx$200 nm and the absorption coefficient α=1000 cm^{-1} [2].

A.2.2 Results for GaTe thin films

We used the same fitting procedure for GaTe with the results shown in Fig.3.2(b). Although the 'kink' in the thickness-dependence of I_{PL} for GaTe is not as pronounced as for GaSe, it is still observable at a slightly higher value of $2h_0$=40 nm. The model describes adequately the data for h_{film} up to around 90 nm, but fails to reproduce

the very steep enhancement of PL for thicker films. This probably occurs due to the contribution of the free excitons to the PL signal. It is probable that there is an additional strong non-radiative escape mechanism for free excitons in thin films, which is overcome in thicker films with the result that the PL intensity for thick films grows faster than the model predicts. Another reason could be deviation from the effectively 'ballistic' transport that we assumed leads to the carrier escape into regions (1), and its replacement for the larger thicknesses with a slower 'diffusion' process.

In a similar way to GaSe, we confine ourselves to determination of the order of magnitude only for the main parameters, which are similar to GaSe: we find that $\tau_{rel}u_1$ is of the order of a 1000 nm and $\tau_{rel}u_2$ is of the order of a 100 nm. As an illustration for the GaTe data, in Fig.3.2(b) we show a fitting with $P\alpha = 5.0 \times 10^6$ nm^{-1}s^{-1}, $\tau_{rel}/\tau_1 = 3800$ nm and $\tau_{rel}/\tau_2 = 200$ nm. The figure also shows the variation of PL intensity as would be expected from the change in absorption only (dashed line). This curve is described by the expression $I_{PL} = I_{GaTe}[1 - exp(-\alpha_{GaTe}h_{film})]$, where I_{GaTe} is the PL intensity for films with $h_{film} \approx 200$ nm. The absorption coefficient $\alpha_{GaTe} = 5000$ cm^{-1} is used according to Ref. [2].

References

[1] Raffaella Calarco, Michel Marso, Thomas Richter, Ali I Aykanat, Ralph Meijers, André vd Hart, Toma Stoica, and Hans Lüth. Size-dependent photoconductivity in mbe-grown gan-nanowires. *Nano letters*, 5(5):981–984, 2005.

[2] J Camassel, P Merle, H Mathieu, and A Gouskov. Near-band-edge optical properties of ga se x te 1- x mixed crystals. *Physical Review B*, 19(2):1060, 1979.

Appendix B

Calculation of collection efficiency

In chapters 5 and 6 the external quantum efficiency was calculated following the description of section 2.2.1. In order to get the most accurate calculation it is necessary to take into account the losses on the system used to measure. This will depend on the device environment inside the sample, optics used to collect and guide the light emitted and the detector. On this appendix a detailed description of the calculation wis presented

In section 2.2.1 the quantum efficiency was defined as the number of photons emitted per number of injected electron-hole pairs. In order to estimate the number of emitted photons we need to estimate our collection efficiency. The total loss is defined as:

$$\eta = \eta_{Lens}\eta_{optic}\eta_{system} \tag{B.1}$$

η_{optic} is the loss of all the optical components in the optical circuit. It was measured directly using a 1.96 eV laser and a power meter to determine the loss at each component. We find $\eta_{optic} = 0.18$.

η_{system} - converts the number of photons arriving at the incoming slit of the detector

into the detector counts. It takes into account the loss of photons which pass through the slit, grating and onto the CCD and has been again measured directly by using the 1.96 eV laser and taking spectra of the laser for different powers in order to get a counts vs incident photons. For our system we get 4203 integrated cts/sec per 1 pW. If the system were 100% efficient we should count $N = P/h\nu = 3177476$ photons, therefore we arrive at an estimate for the system efficiency to be $\eta_{system} = 4203/3177476 = 1.32 \times 10^{-3}$.

η_{Lens} is the efficiency of the lens collection[3]. We use a 50x objective with a numerical aperture, $NA = 0.55$. LEDs are fabricated on either two substrates, firstly Si/SiO_2(290nm) with refractive index of Si (n=3.734) and SiO_2(n=1.645) or distributed Bragg reflectors which consist of 10 alternating quarter wave pairs (187.5 nm) of SiO_2 (n=1.46) and NbO_2 (n=2.122) [1, 2].

Numerical simulations allow us to make an improved estimate of the collected light emitted from a dipole on each substrate type. Our NA=0.55. This gives a collection angle of 33.4°.

So for a WSe_2 flake on SiO2 we find that:

$$\eta_{Lens} = \frac{P_{SiO_2}(33.4)}{P_{SiO_2}(180)} = 2.5\% \tag{B.2}$$

while for WSe_2 flake on a DBR we find that:

$$\eta_{Lens} = \frac{P_{DBR}(33.4)}{P_{DBR}(180)} = 31\% \tag{B.3}$$

This gives us two loss factors depending on the substrate the LED was fabricated onto.

$$\eta_{SiO_2} = 0.18 \times 1.32 \times 10^{-3} \times 0.025 = 5.94 \times 10^{-6} \tag{B.4}$$
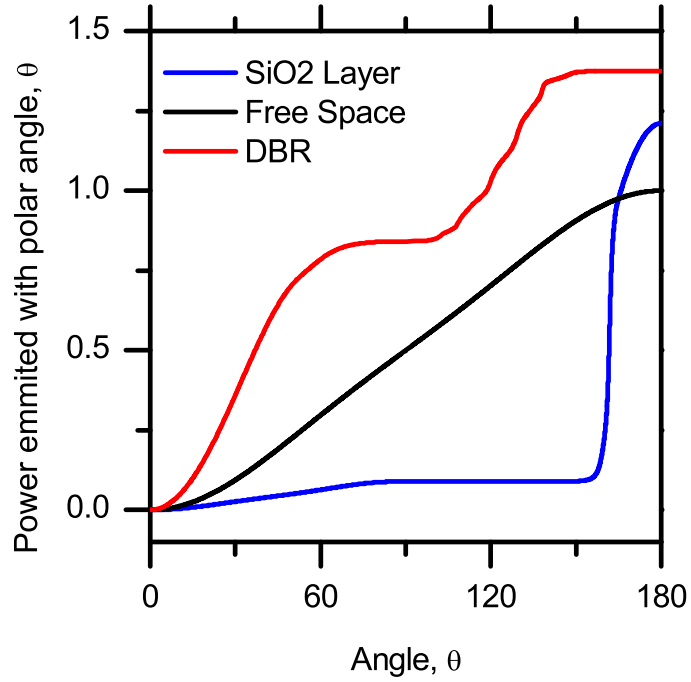
Fig. B.1 Total power emitted within a polar angle for an emitting dipole placed on Si/SiO$_2$ and on a distributed Bragg reflector (DBR) as well as in free space.

$$\eta_{DBR} = 0.18 \times 1.32 \times 10^{-3} \times 0.31 = 7.37 \times 10^{-5} \tag{B.5}$$

References

[1] S Dufferwiel, S Schwarz, F Withers, AAP Trichet, F Li, M Sich, Del Pozo-Zamudio, C Clark, A Nalitov, DD Solnyshkov, et al. Exciton-polaritons in van der waals heterostructures embedded in tunable microcavities. *arXiv preprint arXiv:1505.04438*, 2015.

[2] Stefan Schwarz, Scott Dufferwiel, PM Walker, Freddie Withers, AAP Trichet, Maksym Sich, Feng Li, EA Chekhovich, DN Borisenko, Nikolai N Kolesnikov,

References

et al. Two-dimensional metal–chalcogenide films in tunable optical microcavities. *Nano letters*, 14(12):7003–7008, 2014.